The magmatic architecture of continental flood basalts II : A new conceptual model

Tushar Mittal [1,2] **and Mark A. Richards**[2,3]

[1]Department of Earth, Atmospheric and Planetary Sciences, Massachusetts Institute of Technology, Cambridge, Massachusetts, USA
[2]Department of Earth and Planetary Science, University of California, Berkeley, California, USA
[2]Department of Earth and Space Sciences, University of Washington, Seattle, Washington, USA

Key Points:

- Mechanical magma reservoir model demonstrates that individual CFB eruptive events cannot be fed by a single large crustal magma body.
- CFB eruptions are likely fed from a number of small-medium sized ($\sim 10^2$ - $10^{3.5}$ km^3) interconnected magma reservoirs.
- Our new transcrustal magmatic plumbing model explains the primary geophysical and geochemical characteristics for continental flood basalts.

Corresponding author: Tushar Mittal, tmittal2@berkeley.edu

Abstract

Continental flood basalts intruded and erupted millions of km^3 of magma over $\sim$ 1-5 Ma. Previous work proposed the presence of large ($> 10^5$-10^6 km^3) crustal magma reservoirs to feed these eruptions. However, in Paper I, we illustrated that this model is inconsistent with observations, by combining eruptive rate constraints with geochemical and geophysical observations from the Deccan Traps and other CFBs. Here, we use a new mechanical magma reservoir model to calculate the variation of eruptive fluxes (km^3/year) and volumes for different magmatic architectures. We find that a single magma reservoir cannot explain the eruptive rate and duration constraints for CFBs. Using a 1D thermal model and characteristic timescales for magma reservoirs, we conclude that CFB eruptions were likely fed by a number of interconnected small-medium ($\sim 10^2$ - $10^{3.5}$ km^3) magma reservoirs. It is unlikely that each individual magma reservoir participated in every eruption, thus permitting the occasional formation of large xenocrysts (e.g., megacrystic plagioclase). This magmatic architecture permits (a) large volume eruptive episodes with 10s to 100s of years duration, and (b) relatively short time-periods separating eruptive episodes (1000s of years) since multiple mechanisms can trigger eruptions (via magma recharge or volatile exsolution, as opposed to long term (10^5 - 10^6 year) accumulation of buoyancy overpressure), and (c) lack of large upper-crustal intrusive bodies in various geophysical datasets. Our new proposed magmatic architecture has significant implications for the tempo of CFB volatile release (CO_2 and SO_2), potentially helping explain the pre-K-Pg warming associated with Deccan Traps.

1 Introduction

Continental flood basalt provinces (CFBs) are some of the largest magmatic events in Earth history and their "main eruptive phase" (durations $\sim$ 1 Ma; V. E. Courtillot & Renne, 2003; Bryan et al., 2010; V. Courtillot & Fluteau, 2014; Ernst & Youbi, 2017; Svensen et al., 2018) are associated with eruption of millions of km^3 of dominantly pāhoehoe basaltic lava flows over vast areas (e.g., Self et al., 1998; Mahoney & Coffin, 1997; Bryan & Ferrari, 2013; Ernst, 2014, and references therein). CFBs are critical events in the interaction between the solid Earth and surface environment since the volatile emissions from degassing of erupted lavas (as well as intrusives) can strongly perturb the ecosystem (Clapham & Renne, 2019; Torsvik, 2020). This relationship is illustrated by the frequently temporal correlation of CFBs with significant environmental perturbations on a global scale, including major mass extinctions and rapid climate change (e.g., Wignall, 2001; Jones et al., 2016; Ernst & Youbi, 2017; Clapham & Renne, 2019). Most CFBs are associated with the arrival of a deep mantle plume head and consequent high degree of mantle melting at the base of the lithosphere over a spatially extended region (e.g., M. A. Richards et al., 1989; Campbell & Griffiths, 1990; Farnetani & Richards, 1994; Ernst, 2014; Ernst et al., 2019).

Although the overall time-duration of CFBs can extend to 5-15 Ma (V. E. Courtillot & Renne, 2003; V. Courtillot & Fluteau, 2014; Svensen et al., 2018), typically most of the CFB erupted volume is emplaced in the "main-phase" eruptions. As an example, more than $>$ 60% of the Deccan Traps volume was erupted in $\sim$ 800 kyr around the Cretaceous-Paleogene boundary (M. A. Richards et al., 2015; Schoene et al., 2019; Sprain et al., 2019). This CFB main phase is in turn composed of hundreds of individual eruptive episodes each representing the eruptive products from a single or few dike associated fissures (Self et al., 2014). In the field, each eruptive episode comprises a flow-field built up of one or several lava flows (See Thordarson & Self, 1998; Self et al., 1998; Jay et al., 2009, for more discussion of the terminology). Analysis of typical CFB flow fields, especially in the Columbia River Basalt province, suggest that they were emplaced over at least a decade, and likely over multiple centuries (Vye-Brown, Self, & Barry, 2013; Fendley et al., 2019). Individual flow fields in CFBs

have lava volumes ranging from 10^3- 10^4 km^3 with individual flows 100s of km long (Self et al., 2008; Bryan et al., 2010; Self et al., 2014; Fendley et al., 2020).

This unique magmatic character of CFBs compared to modern basaltic volcanism underscores two fundamental questions: *What are the geophysical conditions, with respect to melt generation and transport, that are required for CFBs ? What is the crustal plumbing system of these CFBs that permits large, repeated individual eruptive events? This magmatic architecture is related to another key question: why do flood basalts erupt persistently in such large eruptive episodes?*. In this series of papers, we explore the hypothesis that the unique character of "flood" basalt eruptions is a consequence of the distinct crustal magmatic architecture. At present, it is unclear how large individual magma bodies are as well as how they organize spatio-temporally to transfer melt from a mantle plume source to the surface (Jerram & Widdowson, 2005; Ernst, 2014; Cruden & Weinberg, 2018; Coetzee & Kisters, 2018; Magee et al., 2018; Magee, Ernst, et al., 2019).

In our first paper (Paper I), we tested the previously proposed large ($> 10^5$-10^6 km^3) magma reservoir model for CFB magmatic architecture (Karlstrom & Richards, 2011; Black & Manga, 2017) using eruptive tempo constraints from the Deccan Traps as well as other CFBs wherever available. In contrast to model predictions, our analysis of geochronological, paleomagnetic, volcanological, and Hg proxy datasets from the Deccan Traps found no evidence for long eruptive hiatuses (¿ 50 kyr) or evidence for very pulsed eruptive history during the Deccan main phase volcanism. In addition, we found that stratigraphic geochemical variations in the Deccan Traps (and other CFBs) are very difficult to explain with the 2-stage (one at Moho depth, another in upper crustal depth) large magma reservoir model. Finally, we found no volcanological (Deccan dike swarm spatial pattern) or geophysical (seismic, magnetotelluric, gravity) evidence for the a large upper magma body in the Deccan. Given the mismatch between the CFB observations and model predictions, we conclude that the large reservoir model does not explain observations from Deccan Trap (and many other CFBs). Instead, we posit that the large, spatially distributed, magma flux from a mantle plume head (and the consequent thermal input) allows multiple magma bodies to remain eruptible. Each of these magma reservoirs undergoes Recharge-Eruption-Assimilation-Fractional Crystallization processes and stochastically interconnect to feed large eruptive episodes. Conceptually, this magmatic architecture is a scaled up version of the magmatic architecture that has been recently proposed for many ocean island basalts and arc volcanoes (e.g., Edmonds et al., 2019, and references therein). We hypothesize that during the course of a CFB event, the spatial distribution and interconnectivity of magma reservoirs evolves due to increasing mantle melt flux and the development of efficient vertical melt pathways in the lithosphere and the lower crust. These transitions are the primary reason for the unique nature of flood basalts, especially the "main-phase" eruptions.

In this study, we test this conceptual model with numerical models to assess whether this model architecture can indeed quantitatively reproduce the CFB eruptive tempo estimates as well as other geochemical and geophysical observations. In Section 2, we describe a sequence of new models for fissure-style eruptions fed from either a single or multiple coupled magma reservoirs, as well as thermal models to assess how the crustal properties will evolve over the lifetime of a CFB event. These models allow us to predict the erupted fluxes, total erupted volumes (or equivalently the duration of eruptions), and frequency of eruptions for different CFB magmatic architectures and reservoir sizes. In Section 3 and 4, we describe the results of these models, emphasizing their consistency with various observational constraints and inferences regarding the required CFB magmatic plumbing system. Finally, in Section 5 and 6, we discuss the implications of our model results in terms of a new model for magmatic architecture

for CFBs, emphasizing the importance of small multiple connected magma reservoirs for feeding the large volume basaltic lava flows.

2 Magmatic system Model

The three primary "quantitative" physical constraints with regards to CFB eruptive episodes are : a) the eruptive volume fluxes (km^3/year, Section 3.4 and 3.5 Paper I), b) the total erupted volumes of each flow unit (or equivalently the typical duration of each eruptive event, Section 3.4 and 3.5 Paper I), and c) the frequency of eruptive intervals (Section 3.2-3.5 Paper I). In order to assess how these parameters vary as a function of reservoir geometry and crustal properties for a single reservoir, as well as a set of connected reservoirs, we use a set of two model frameworks. Firstly, we use a volume-averaged visco-elastic mechanical model for an ellipsoidal magma reservoir coupled to a dike-shaped erodible conduit to calculate eruption rates and duration (Section 2.1). We then use idealized 1D thermal models with time-varying plume associated melt influx. In combination with characteristic timescales for magma reservoir evolution (Degruyter & Huber, 2014; Mittal & Richards, 2019), these model results allow us to assess how evolving crustal visco-elastic properties affect the likelihood of crustal magma accumulation vs. surface eruption.

2.1 Definition of Magma Reservoir

Consistent with our description in Paper I as well as a wide range of magmatic system modeling work (Black & Manga, 2017; Degruyter & Huber, 2014, e.g.,), we use "magma reservoir" to refer to a well-mixed magma body with a volume-averaged temperature, melt and volatile composition. We readily acknowledge that this real magma bodies, especially with mush zones, may not be compositionally well mixed (see Marsh (2013)). Still, this commonly used approximation makes the modelling mathematically much more tractable. With this terminology, we will interpret a single very large magma chamber with spatial variations in thermal, chemical, and rheological properties as being multiple magma reservoirs with a high degree of inter-connectivity.

2.2 Magma Reservoir Model

2.2.1 Model Setup and assumptions

We start with a magma reservoir of a chosen geometry emplaced within a visco-elastic crustal half-space. We assume that the reservoir has reached the critical overpressure ($\Delta P \sim$ 20-40 MPa, Rubin, 1995; Caricchi et al., 2014; Degruyter & Huber, 2014; Mittal & Richards, 2019) for crustal tensile failure and has just been connected to the surface through a dike-shaped conduit (See Fig.7). With this initial condition, we use a mechanical model (described in subsequent sections) to calculate the surface eruption rate and the total erupted volume before the dike closes due to magma solidification. Additionally, we allow for the scenario that the magma reservoir is connected to additional crustal reservoirs through conductive magma pathways (Figure 1). For these calculations, we are agnostic about both how long it took to assemble the magma body and if the ΔP was achieved through recharge, buoyancy overpressure, or volatile over-pressurization (e.g., Degruyter & Huber, 2014). Additionally, we do not use a full thermo-mechanical box model for the magma reservoir evolution (e.g., Degruyter & Huber, 2014; Mittal & Richards, 2019) since the cooling timescale for even a 1 km radius magma reservoir ($L^2/\kappa_{thermal} \sim 30,000$ years, thermal diffusivity $\kappa_{thermal} \sim 10^{-6}$ m^2/s, Karlstrom et al. (2017)) takes much longer than the time duration of individual CFB eruptive episodes (100s to few 1000s of years, Section 3.4, 3.5, Paper I).

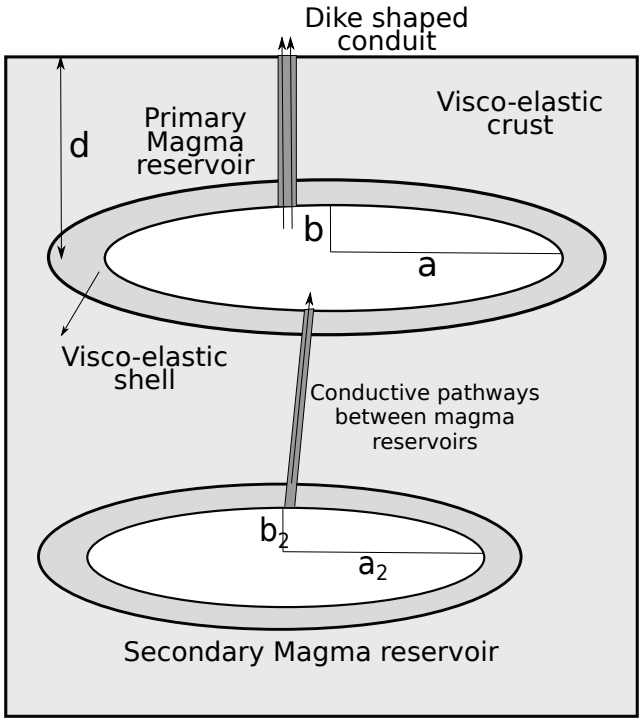

Figure 1: Schematic of the the magma reservoir model (Section 2.1). The primary magma reservoir is connected to the surface through a dike-shaped conduit and it can also be connected to one or multiple secondary reservoirs at depth.

The primary components of our magma reservoir model are a) compressible ellipsoidal magma reservoir with influx from another reservoir, b) visco-elastic crust, and c) erodible dike-shaped conduit feeding surface eruption. Initially, the overpressure and buoyancy of the melt-crystal-magmatic volatile (MVP, CO_2 and H_2O) magma mixture drives surface eruption through the dike. With mass flux out of the reservoir, the overpressure in the magma reservoir progressively decreases, leading to a reduced eruption rate. The rate of overpressure change is modulated by the visco-elastic response of the surrounding crust as well as magma influx from other reservoirs. Eventually, the magma overpressure and buoyancy are insufficient to drive fast enough magma flow rate through the dike to prevent solidification. Throughout the eruptive period, we allow the dike width to increase at a rate proportional to the shear traction on the dike walls to approximate the process of thermal and mechanical erosion and plastic deformation (following Piombo et al., 2016). This additional process approximates the rapid initial increase and subsequent slow decay in discharge rates that has been documented for many basaltic fissure eruptions, such as Stromboli (Italy), Holhuraun (Iceland), Piton de la Fournaise (La Réunion), Kilauea (Hawaii) (e.g., Wadge, 1981; Hon et al., 1994; Pedersen et al., 2017; Harris et al., 2007; Calvari, 2019, and references therein).

For mathematical simplicity, we make several simplifying assumptions in our model. Firstly, we do not have the initial diking phase in our model calculations. Even if a magma reservoir reaches critical overpressure, the consequent dike may not always reach the surface to feed eruptions. Secondly, our dike-shaped conduit model does not include the multi-physics processes in the conduit, especially the rheological changes associated with vapor exsolution, crystallization, and bubble growth in ascending melts (e.g., H. Gonnermann & Manga, 2012; H. M. Gonnermann, 2015; Cassidy et al., 2018;

A. Aravena, Cioni, de' Michieli Vitturi, et al., 2018). Additionally, we do include a very parameterized form of melt transport into the magma reservoir from other reservoirs. Thirdly, we do not model any potential migration of active fissures along a dike during an eruption (See Section 5.1, Paper I for CFB observations). For instance, the ten dike-fed fissures in the Laki 1783 eruption opened in sequence, with each individual dike segment only active for a short time (days - months, Thordarson & Self, 1993). A similar, well-characterized recent analog of this process is the Kilauea 2018 eruption (C. A. Neal et al., 2019) wherein the feeder dike kept propagating during the early phases of the eruption with multiple active vents. Finally, we do not allow changes in crystal, melt, and volatile-gas volume fractions in the magma reservoir due to magma mixing, preferential loss of vapor phase during an eruption, or fractional crystallization. We do allow changes in the MVP volume fraction and magma mixture density in the magma reservoir due to pressure-dependent CO_2- H_2O solubility and vapor phase density.

Although the physical processes mentioned above are important for understanding the full dynamics of CFB eruptions, our interest in this study is to obtain first-order estimates of eruption rates and duration (within a factor of 2 at best). Our constraints for CFB eruption are not sufficiently precise to warrant a more complicated model with additional unconstrained model parameters. Furthermore, the physical mechanisms associated with vent localization as well as fissure transition during a basaltic fissure eruption are not well understood even for modern basaltic eruptions. We anticipate that the unmodeled processes will principally introduce additional short timescale variability to the eruption rate (e.g., Patrick et al., 2019) but will not qualitatively change our conclusions (A. Aravena, Cioni, de' Michieli Vitturi, et al., 2018). We would also note that for magma reservoirs having a volume of at least $\sim$ 10 km^3 (much smaller than what we consider in our calculations), dikes can reach the surface even from $\sim$ 10 km depths (Townsend & Huber, 2020a). Thus, although our model is simplified vis-a-vis a real flood basalt eruption, a more complex model is beyond the scope of this present study. We can also perform a much larger parameter space exploration with our model compared to a full multi-physics conduit model.

In the subsequent sections, we first describe the basic model framework followed by analytical solutions for spherical and ellipsoidal magma reservoirs under simplifications. We then add additional complexity to develop the full numerical ODE model for a single magma reservoir and subsequently multiple coupled magma reservoirs.

2.2.2 Conservation Equations

Since the mass of the magma reservoir $M_{res} = \rho_{res} V$, the chamber averaged mass conversation equation for the magma reservoir is :

$$\frac{dM_{res}}{dt} = V\frac{d\rho_{res}}{dt} + \rho_{res}\frac{dV}{dt} \tag{1}$$

where M_{res}, ρ_{res}, and V are respectively the mass, density, and volume of the magmatic reservoir. P is the over-pressure in the magma reservoir with respect to a lithostatic pressure at the same depth. Using the combined compressibility of the magmatic mixture (crystal + magmatic volatiles + magma) in the reservoir (β_{res}), we can write an equation for the change in density of the magmatic mixture in the reservoir :

$$\frac{d\rho_{res}}{dt} = \rho_{res}\beta_{res}\frac{dP}{dt} \tag{2}$$

Analogously, we can use the following equation for $\frac{dV}{dt}$:

$$\frac{dV}{dt} = V\beta_{cr}\frac{dP}{dt} + V\frac{P}{\eta_{cr}} \tag{3}$$

Here, β_{cr} is the elastic compressibility and η_{cr} is the viscosity of the surrounding crust. We have added an extra term for the change in reservoir volume (VP/η_{cr}) to provide a first order approximation for the crustal response, akin to many other lumped parameter magma chamber models (e.g., Degruyter & Huber, 2014). For a spherical magma chamber, $\beta_{cr} = \frac{3}{4K_{cr}}$ where K_{cr} is the effective elastic modulus of the crust (K. Anderson & Segall, 2011; Degruyter & Huber, 2014; Rivalta & Segall, 2008; Rivalta, 2010).

Using these relationships, we can re-write the mass conservation equation :

$$\implies \frac{dM_{res}}{dt} = \rho_{res} V \beta_{res} \frac{dP}{dt} + \rho_{res}\Big[V\beta_{cr}\frac{dP}{dt} + V\frac{P}{\eta_{cr}}\Big] \tag{4}$$

$$\implies \frac{dM_{res}}{dt} = \rho_{res} V \Big[\beta_{res} + \beta_{cr}\Big]\frac{dP}{dt} + \rho_{res} V \frac{P}{\eta_{cr}} \tag{5}$$

.

We assume an ellipsoidal shape for the magma reservoir with semi-major $a_c = c_c$ and semi-minor axis b_c and hence eccentricity $e = (1/a_c)\sqrt{a_c^2 + b_c^2}$. An ellipsoidal geometry enables us to model large spatially extensive magma chambers wherein the $a_c > b_c$. The volume and surface area of the oblate ellipsoid is Weisstein (2003):

$$V = \frac{4\pi}{3} a_c^2 b_c \tag{6}$$

$$S_{res} = 2\pi a_c^2 + \pi \frac{b_c^2}{e} ln\Big(\frac{1+e}{1-e}\Big) \tag{7}$$

As magma is drained from the reservoir, the volume of the reservoir, and hence its dimensions will evolve with time. For mathematical simplicity, we assume that the aspect ratio of the magma reservoir ($O_{res} = b_c/a_c$) will remain constant. Although in practice, this assumption will likely not exactly hold, we expect that to first order this is reasonable for moderate aspect ratios given the expectation for the end-member case of a sphere wherein the magma reservoir will shrink/expand symmetrically. The consequent time evolution of the reservoir volume is :

$$\frac{dV}{dt} = 4O_{res}\pi a_c^2 \frac{da_c}{dt} \tag{8}$$

$$\text{Substituting the definition of } \frac{\mathrm{dV}}{\mathrm{dt}} \text{ in Eqn 3, we have :} \tag{9}$$

$$4O_{res}\pi a_c^2 \frac{da_c}{dt} = \frac{4O_{res}\pi}{3} a_c^3 \Big[\beta_{cr}\frac{dP}{dt} + \frac{P}{\eta_{cr}}\Big] \tag{10}$$

$$\implies \frac{da_c}{dt} = \frac{a_c}{3}\Big[\beta_{cr}\frac{dP}{dt} + \frac{P}{\eta_{cr}}\Big] \tag{11}$$

Since the mass of the reservoir can only be changed by fluxes into and out of the reservoir, the mass conservation eqn will be :

$$\frac{dM_{res}}{dt} = R_{in} - R_{out} \tag{12}$$

whereR_{in} and R_{out} represent flux into and out of the magma reservoir.

The mass flux into the magma reservoir (R_{in}) is modeled as follows, similar to the analysis in Segall (2016); K. Anderson and Segall (2011) :

$$\frac{dM_{in,res}}{dt} = \Omega(t)(P^{\infty} - P + B_2^1)^n \tag{13}$$

where $\Omega(t)$ is a time dependent conductivity (with units of Kg/Pa s) between the two magma reservoirs 1 & 2 and P^{∞} is the over-pressure in the secondary magma

reservoir w.r.t to its local lithostatic pressure. B_2^1 is the buoyancy overpressure due to the magma buoyancy between the two chambers if they are at different depths. B_2^1 is defined as :

$$B_2^1 = (\rho_{c,2} - \rho_{res,2})gd_{res,2} - (\rho_{c,1} - \rho_{res,1})gd_{res,1} \tag{14}$$

where $d_{res,1}, \rho_{res,1}$ and $d_{res,2}, \rho_{res,2}$ are respectively the depths and mixture densities of reservoirs 1 & 2. This term is added to ensure that when the two magma reservoirs reach a magmastatic pressure condition, there is no mass flux between them. This implies that $P^{\infty}_{mgst} = -(\rho_{c,2} - \rho_{res,2})gd_{res,2}$, $P_{mgst} = -(\rho_{c,1} - \rho_{res,1})gd_{res,1}$, and $P^{\infty}_{mgst} - P_{mgst} + B_2^1 = 0$. If $(P^{\infty} - P + B_2^1) > 0$, there is a magma flux into the primary magma reservoir from the secondary reservoir and vice-versa. We readily acknowledge that this is a significant simplification of the physical processes of diking and other processes through which melt is transferred between different magmatic reservoirs. In addition, the value of n can be greater than unity for non-linear magma rheology as discussed in Segall (2019). However, this introduces additional, fairly unconstrained free parameters into the model. Consequently, we choose to set $n = 1$ with an exploration of non-linear rheological analysis beyond the scope of the present study. We parameterize the time-dependent conductivity as :

$$\Omega(t) = \Omega_0\Big(1 - e^{-t/t_{cond}}\Big) \tag{15}$$

where t_{cond} is the conductivity timescale and Ω_0 is the conductivity amplitude. We readily acknowledge that in reality, the connectivity between individual magma bodies is more complicated and can include anastomosing fault zones, vein networks, dikes, and segmented bridges as illustrated by various field examples (Pollard et al., 1975; Schofield et al., 2012; Magee, Muirhead, et al., 2016; Magee, O'Driscoll, et al., 2016; Schofield et al., 2017; Magee, Muirhead, et al., 2019; Galland et al., 2019, and references therein). However, these physical processes are very challenging to model accurately even in a simple system. Thus, we have chosen a simplified, but commonly used form for melt conductivity between magma reservoirs.

The magma flux out of the magma reservoir is modeled as a dike shaped conduit with semi-major axis a and semi-minor axis b ($b << a$). The volume flux out from the magma reservoir is :

$$Q_{out,res} = \frac{\pi}{4}\Big[\frac{P(t) + (\rho_c - \rho_{res})gd_{res}}{d_{res}}\Big]\frac{1}{\eta_{res}}\frac{a^3b^3}{a^2 + b^2} \tag{16}$$

$$\text{and consequently the mass flux out is } : \frac{dM_{out,res}}{dt} = -\rho_{res}Q_{out,res}(t) \tag{17}$$

where η_{res} is the viscosity of the magma mixture erupting at the surface, g is the acceleration due to gravity, and ρ_c is the crustal density at the depth of the magma reservoir.

Combining Equations 17, 13, and 5, we have the following mass conservation equation with influx and outflux:

$$\rho_{res}V\Big[\beta_{res} + \beta_{cr}\Big]\frac{dP}{dt} + \rho_{res}V\frac{P}{\eta_{cr}} \tag{18}$$
$$= -\rho_{res}\frac{\pi}{4}\Big[\frac{P(t) + (\rho_c - \rho_{res})gd_{res}}{d_{res}}\Big]\frac{1}{\eta_{res}}\frac{a^3b^3}{a^2 + b^2} + \Omega(t)(P^{\infty} - P + B_2^1)$$

$$\text{where } \frac{dP}{dt} = -\frac{P}{\eta_{cr}(\beta_{res} + \beta_{cr})} - \frac{\pi}{4V}\Big[\frac{P(t) + (\rho_c - \rho_{res})gd_{res}}{d_{res}}\Big]\frac{1}{\eta_{res}(\beta_{res} + \beta_{cr})}\frac{a^3b^3}{a^2 + b^2} + \tag{19}$$
$$\Omega(t)(P^{\infty} - P + B_2^1)\frac{1}{\rho_{res}V(\beta_{res} + \beta_{cr})}$$

We define a non-dimensional compressibility $\tilde{\beta}_s = (\beta_{res} + \beta_{cr})/\beta_{sph}$ where the net compressibility is scaled with the value for a spherical crustal reservoir ($\beta_{sph} = \frac{3}{4K_{cr}}$).

Substituting this into the equation set above, we get :

$$\frac{dP}{dt} = -\frac{4K_{cr}P}{3\eta_{cr}\tilde{\beta}_s} - \frac{K_{cr}}{4d_{res}\eta_{res}}\Big[\frac{P(t)+(\rho_c-\rho_{res})gd_{res}}{\tilde{\beta}_s a_c^2 b_c}\Big]\frac{a^3b^3}{a^2+b^2} + \Omega(t)(P^\infty - P + B_2^1)\frac{K_{cr}}{\pi a_c^2 b_c \tilde{\beta}_s \rho_{res}} \tag{20}$$

The typical timescales in this pressure evolution equation are (assuming $a >> b$):

$$t_{Maxwell} = \frac{\eta_{cr}\tilde{\beta}_s}{K_{cr}} \tag{21}$$

$$t_{flux} = \frac{4d_{res}a_c^2 b_c}{ab^3}\frac{\eta_{res}\tilde{\beta}_s}{K_{cr}} \tag{22}$$

$$t_{repres} = \frac{\pi a_c^2 b_c \tilde{\beta}_s \rho_{res}}{\Omega K_{cr}} \tag{23}$$

Here $t_{Maxwell}$ is the viscous stress relaxation timescale, t_{repres} is the timescale to repressurize the magma reservoir by recharge, and t_{flux} is the timescale to relax the magma overpressure by dike-fed eruptions.

Following the model presented in Piombo et al. (2016) to explain the observed transient increase in volume flux in dike fed basaltic eruptions, we allow the dike semi-minor axis to evolve over time due to mechanical erosion (according to Dragoni & Santini, 2007). The erosion rate is assumed to be proportional to the shear traction on the conduit walls :

$$\tau \sim \frac{\eta_{res}Q}{(\pi ab)b} \tag{24}$$

$$\implies \tau \sim \Big[\frac{P(t)+(\rho_c-\rho_{res})gd_{res}}{d_{res}}\Big]b \tag{25}$$

.

The wall of the conduit maintains an elliptical shape despite erosion. We keep the semi-major axis (a) constant with time since $a >> b$ and it is much easier for dikes to accommodate increased flux by elastic deformation of the semi-major axis b (Dragoni & Tallarico, 2018). Hence, we have the following time evolution equation for b :

$$\frac{db}{dt} = \frac{k}{d_{res}}\Big[P(t)+(\rho_c-\rho_{res})gd_{res}\Big]\frac{a^2 b}{a^2+b^2} \tag{26}$$

$$\frac{db}{dt} \approx \frac{k}{d_{res}}\Big[P(t)+(\rho_c-\rho_{res})gd_{res}\Big]b \tag{27}$$

where k is the erosion rate per unit traction (m/Pa-s). A. Aravena, Cioni, de' Michieli Vitturi, et al. (2018) show that to first order, the results of this model are consistent with the more complex conduit model with elastic deformation, depth dependent viscosity, and multi-phase processes. The permanent plastic deformation of the conduit (represented by the erosion term) is much larger than conduit shape variation by elastic deformation except at the very end of the eruption (See Fig. S6 A. Aravena, Cioni, de' Michieli Vitturi, et al., 2018).

2.2.3 Spherical Magma Chamber

First, we consider a visco-elastic mechanical model for a spherical chamber modified from Segall (2016). The primary feature of this model is the inclusion of a visco-elastic shell with an outer radius of R_2 surrounding the magma chamber of radius R_1. Additionally, we include a melt flux into the magma chamber as well a melt flux out

due to a dike fed surface eruption. Since the magma reservoir geometry is spherical, $a_c = b_c = R_1$. The new mass conservation equation is :

$$\frac{dM_{res}}{dt} = V\frac{d\rho_{res}}{dt} + \rho_{res}\frac{dV}{dt} \tag{28}$$

$$\implies \frac{dM_{res}}{dt} = \rho_{res}V\beta_{res}\frac{dP}{dt} + \rho_{res}\Big[4\pi R_1^2\frac{du_r}{dt}(r=R_1) + V\frac{P}{\eta_{cr,fr}}\Big] \tag{29}$$

where $u_r(r = R_1)$ is the radial displacement at the edge of the magma reservoir and $\eta_{cr,fr}$ is the viscosity of the far-field crust. The first term for the volume displacement is due to the deformation of the visco-elastic shell embedded in an elastic medium, whereas the other term represents deformation back to lithostatic pressure from far field longer duration viscous relaxation. Combining with the mass flux terms into and out of the primary chamber, we get :

$$\begin{aligned} -\rho_{res}\frac{\pi}{4}\Big[\frac{P(t)+(\rho_c-\rho_{res})gd_{res}}{d_{res}}\Big]\frac{1}{\eta_{res}}\frac{a^3b^3}{a^2+b^2} + \Omega(t)(P^\infty - P + B_2^1) \\ = \rho_{res}V\beta_{res}\frac{dP}{dt} + \rho_{res}\Big[4\pi R_1^2\frac{du_r}{dt}(r=R_1) + V\frac{P}{\eta_{cr,fr}}\Big] \end{aligned} \tag{30}$$

For notational convenience, we define a few additional variables as follows :

$$B^1 = (\rho_c - \rho_{res})gd_{res} \tag{31}$$

$$Q^1 = \rho_{res}\frac{\pi}{4d_{res}}\frac{1}{\eta_{res}}\frac{a^3b^3}{a^2+b^2} \tag{32}$$

$$Q^{rl} = \frac{V}{\eta_{cr,fr}} \tag{33}$$

Consequently, we can re-write the mass conservation equation as :

$$-\frac{Q^1}{\rho_{res}}(P+B^1) + \frac{\Omega}{\rho_{res}}(P^\infty - P + B_2^1) - Q^{rl}P = V\beta_{res}\frac{dP}{dt} + 4\pi R_1^2\frac{du_r}{dt}(r=R_1) \tag{34}$$

We can analytically solve this equation set assuming that the terms such as b, ρ_{res}, Ω, and $P^\infty$are not functions of time. Consequently, we can use the Laplace transform to solve the linear equation set. We refer to the reader to the Appendix in Segall (2016) for the full description of the mathematical details and only describe the solution steps here that differ from their analysis. Firstly, the Laplace transformed mass conservation equation is (with the Laplace transform form of P(t) being $\hat{P}$(s)):

$$-Q^1(\hat{P} + \frac{B^1}{s}) + \Omega(\frac{P^\infty}{s} - \hat{P} + \frac{B_2^1}{s}) - Q^{rl}\rho_{res}\hat{P} \tag{35}$$

$$= \rho_{res}V\beta_{res}(s\hat{P} - P_0^+) + \rho_{res}V\beta_{cr}\Big[s\hat{P}\Big(\frac{s+(\alpha+1)t_R^{-1}}{s+t_R^{-1}}\Big) - P_0^+\Big]$$

$$\text{with : } \alpha = \frac{3(1-\nu)}{(1+\nu)}\Big[\Big(\frac{R_2}{R_1}\Big)^3 - 1\Big] \tag{36}$$

$$t_R = \Big[\frac{3\eta_{cr,1}(1-\nu)}{K_{cr}(1+\nu)}\Big]\Big(\frac{R_2}{R_1}\Big)^3 \tag{37}$$

where we have used the solution from Dragoni and Magnanensi (1989) for a spherical magma chamber surrounded by a Maxwell viscoelastic shell in a full space (See Appendix of Segall (2016) for details). Here $\eta_{cr,1}$ is the viscosity in the visco-elastic shell between radius R_1 and R_2 and ν is the Poisson's ratio. Due to the presence of a finite thickness visco-elastic shell, one of the viscous relaxation timescales in this model setup is t_R (Dragoni & Magnanensi, 1989). P_0^+ is the initial value of overpressure at t=0. Substituting the expression for t_{repres} with $a_c = b_c = R_1$, and defining the timescale $\tau_{rl} = t_{repres}(a_c = b_c = R_1)$, we get :

$$-\hat{P}L_1 + \frac{1}{s}L_2 = \tau_{rl}\Big(s\hat{P} - P_0^+ + \beta s\hat{P}\frac{\alpha t_R^{-1}}{s+t_R^{-1}}\Big) \tag{38}$$

$$\text{with}: \ \beta = \frac{\beta_{cr}}{\beta_{cr} + \beta_{res}} \tag{39}$$

$$L_1 = \frac{Q^1 + \Omega + Q^{rl}\rho_{res}}{\Omega} \tag{40}$$

$$L_2 = \frac{-Q^1 B^1 + \Omega(P^{\infty} + B_2^1))}{\Omega} \tag{41}$$

$$\tau_{rl} = \Big[\frac{\pi R_1^3 \tilde{\beta}_s \rho_{res}}{\Omega K_{cr}}\Big] \tag{42}$$

We can re-arrange the equation to get :

$$\hat{P} = \frac{(L_2 + s\tau_{rl}P_0^+)(s + t_R^{-1})}{s[\beta s\tau_{rl}\alpha t_R^{-1} + (s + t_R^{-1})(s\tau_{rl} + L_1)]} \tag{43}$$

The time domain solution of the over-pressure evolution P(t) is :

$$P(t) = \frac{L_2 t_R^{-1}}{\tau_{rl}s_1 s_2} + \frac{(L_2 + s_1\tau_{rl}P_0^+)(s_1 + t_R^{-1})}{s_1\tau_{rl}(s_1 - s_2)}e^{s_1 t} + \frac{(L_2 + s_2\tau_{rl}P_0^+)(s_2 + t_R^{-1})}{s_2\tau_{rl}(s_2 - s_1)}e^{s_2 t} \tag{44}$$

$$\text{where}: \ s_1 = \frac{-1}{2}\Big(t_R^{-1}(1 + \beta\alpha) + \frac{L_1}{\tau_{rl}}\Big) + \frac{1}{2}\sqrt{[t_R^{-1}(1 + \beta\alpha) + \frac{L_1}{\tau_{rl}}]^2 - 4\frac{L_1 t_R^{-1}}{\tau_{rl}}} \tag{45}$$

$$s_2 = \frac{-1}{2}\Big(t_R^{-1}(1 + \beta\alpha) + \frac{L_1}{\tau_{rl}}\Big) - \frac{1}{2}\sqrt{[t_R^{-1}(1 + \beta\alpha) + \frac{L_1}{\tau_{rl}}]^2 - 4\frac{L_1 t_R^{-1}}{\tau_{rl}}} \tag{46}$$

In the limit of no recharge (i.e $\tau_{rl} -> \infty$) and no flux out of the magma chamber ($Q^1 = 0$), we get :

$$P(t) = \frac{P_0^+}{1 + \beta\alpha}(1 + \beta\alpha \exp[-t_R^{-1}(1 + \beta\alpha)t] \tag{47}$$

$$\tag{48}$$

with a characteristic timescale of $t_{R,relax\,compress} = t_R/(1 + \beta\alpha)$ with eventually $P(t)_{lim\ t->\infty} = P_0^+/(1 + \beta\alpha)$.

Using the analytical solution, we can also calculate the crustal stress field surrounding the magma chamber. The hoop stress term is defined as follows for regions 1 (visco-elastic shell) and region 2 (elastic region) :

$$\sigma_{\theta\theta}^{(1)}(r,t) = -\frac{L_2 t_R^{-1}}{\tau_{rl}s_1 s_2} + \frac{(L_2 + s_1\tau_{rl}P_0^+)}{s_1\tau_{rl}(s_1 - s_2)}\Big(\frac{s_1 R_1^3}{2r^3} - t_R^{-1}\Big)e^{s_1 t} + \frac{(L_2 + s_2\tau_{rl}P_0^+)}{s_2\tau_{rl}(s_2 - s_1)}\Big(\frac{s_2 R_1^3}{2r^3} - t_R^{-1}\Big)e^{s_2 t} \tag{49}$$

$$\sigma_{\theta\theta}^{(2)}(r,t) = \frac{L_2 t_R^{-1}}{\tau_{rl}s_1 s_2}\Big(\frac{R_2}{2r}\Big)^3 + \Big(\frac{R_1^3}{2r^3}\Big)\Big[\frac{(L_2 + s_1\tau_{rl}P_0^+)}{s_1\tau_{rl}(s_1 - s_2)}\Big(s_1 + t_R^{-1}\Big(\frac{R_2}{R_1}\Big)^3\Big)e^{s_1 t} + \frac{(L_2 + s_2\tau_{rl}P_0^+)}{s_2\tau_{rl}(s_2 - s_1)}\Big(s_2 + t_R^{-1}\Big(\frac{R_2}{R_1}\Big)^3\Big)e^{s_2 t}\Big] \tag{50}$$

Here, positive values represent tension while negative values imply compression.

2.2.4 Ellipsoidal Magma Chamber

Although the spherical magma chamber model provides a nice theoretical framework to analyze the coupled interaction of magma recharge, dike-fed eruption, and crustal visco-elastic deformation, there are some significant limitations of the model making it difficult to quantitatively use for flood basalt eruptions. In particular, the choice of spherical geometry is a very strong limitation with the maximum volume of magma chambers of order 550 km^3 (for a 5 km Radius chamber) which is significantly

smaller than typical flood basalt eruptive volumes of 2000 - 10,000 km^3. In addition, the conductivity between the magma reservoirs 1 & 2, semi-major and semi-minor axis (a_c and b_c), and dike semi-minor axis (b) are fixed in order to use the Laplace transform method for the analytical solution. The latter is especially critical since an evolution of b is one potential mechanism to explain the observed time-evolution of volume fluxes from basaltic eruptions (Piombo et al., 2016; Calvari, 2019).

We hence modify and extend the eruption model presented in (Piombo et al., 2016). The conservation equations are :

$$\frac{dP}{dt} = -\frac{4K_{cr}P}{3\eta_{cr}\tilde{\beta}_s} - \frac{K_{cr}}{4d_{res}\eta_{res}}\Big[\frac{P(t)+(\rho_c-\rho_{res})gd_{res}}{\tilde{\beta}_s a_c^2 b_c}\Big]\frac{a^3b^3}{a^2+b^2} + \Omega(t)(P^\infty - P + B_2^1)\frac{K_{cr}}{\pi a_c^2 b_c \tilde{\beta}_s \rho_{res}} \tag{51}$$

$$\frac{db}{dt} \approx \frac{k}{d_{res}}\Big[P(t)+(\rho_c-\rho_{res})gd_{res}\Big]b \tag{52}$$

$$\frac{da_c}{dt} = \frac{a_c}{3}\Big[\beta_{cr}\frac{dP}{dt} + \frac{P}{\eta_{cr}}\Big] \tag{53}$$

$$\frac{d\rho_{res}}{dt} = \rho_{res}\beta_{res}\frac{dP}{dt} \tag{54}$$

We first consider an elastic end-member model wherein we set influx equal to zero and ignore crustal viscous stress relaxation as well as changes in a_c and ρ_{res}. We hence have a coupled non-linear ODE system :

$$\frac{dP}{dt} = -\frac{K_{cr}}{4d_{res}\eta_{res}}\Big[\frac{P(t)+(\rho_c-\rho_{res})gd_{res}}{\tilde{\beta}_s a_c^2 b_c}\Big](ab^3) \tag{55}$$

$$\frac{db}{dt} \approx \frac{k}{d_{res}}\Big[P(t)+(\rho_c-\rho_{res})gd_{res}\Big]b \tag{56}$$

The solution of this coupled ODE equation set is :

$$P(t) = C_1 - W_3[B^1 + C_1]e^{W_1}\frac{1}{W_3e^{W_1}+1} \tag{57}$$

$$b^3(t) = \frac{3W_2e^{W_1}}{W_3e^{W_1}+1}(B^1+C_1) \tag{58}$$

$$\text{with : } W_1 = 3W_2(B^1+C_1)(t-3C_2) \tag{59}$$

$$W_2 = \frac{k}{d_{res}} \tag{60}$$

$$W_3 = \frac{1}{t_{flux}b_0^3} \tag{61}$$

Here C_1 and C_2 are the integration constants. Using the initial conditions for P and b at t = 0 :

$$P(t=0) = P_0^+ \tag{62}$$

$$b(t=0) = b_0 \tag{63}$$

we get the following solution :

$$b(t) = \Big[e^{(\alpha_{el}+1)t/t_{flux}}\frac{\alpha_{el}+1}{e^{(\alpha_{el}+1)t/t_{flux}}+\alpha_{el}}\Big]^{1/3}b_0 \tag{64}$$

$$P(t) = \frac{(\alpha_{el}+1)(P_0^+ + B^1)}{e^{(\alpha_{el}+1)t/t_{flux}}+\alpha_{el}} \tag{65}$$

$$\alpha_{el} = 12(P_0^+ + B^1)\frac{\eta_{res}k}{K_{cr}ab_0^3}\hat{\beta}_s a_c^2 b_c \tag{66}$$

$$t_{flux} = \frac{4d_{res}a_c^2b_c}{ab_0^3}\frac{\eta_{res}\tilde{\beta}_s}{K_{cr}} \tag{67}$$

Additionally, the volume flow rate is given by :

$$Q(t) = Q_0(1+\alpha_{el})^2 \frac{e^{(\alpha_{el}+1)t/t_{flux}}}{\left[e^{(\alpha_{el}+1)t/t_{flux}} + \alpha_{el}\right]^2} \tag{68}$$

$$\text{with} \ : Q_0 = ab_0^3 \frac{\pi}{4\eta_{res} d_{res}} (P_0^+ + B^1) \tag{69}$$

and peak flux (Q_{max}) and peak flux time (t_{max}) being :

$$Q_{max} = \frac{Q_0}{4} \frac{(1+\alpha_{el})^2}{\alpha_{el}} \tag{70}$$

$$t_{max} = \frac{t_{flux}}{1+\alpha_{el}} log(\alpha_{el}) \tag{71}$$

For large magma chambers ($a_c, b_c > 1$km), the value of α_{el} is much larger than 1. Hence, we can simplify the Q_{max} relationship as follows :

$$Q_{max} \approx \frac{Q_0}{4} \alpha_{el} \tag{72}$$

$$\implies Q_{max} \approx 3\pi (P_0^+ + B^1)^2 \frac{k\hat{\beta}_s}{K_{cr} d_{res}} a_c^2 b_c \tag{73}$$

$$\tag{74}$$

Interestingly, this relationship is independent of the initial shape of the dike as well as magma mixture viscosity. Using typical values for $K_{cr} \sim 10^{10}$ Pa, $\beta_s \sim 5$, k$\sim 10^{-10}$ m/Pa-s, $P_0^+ \sim 20$MPa, $\Delta\rho \sim 300$km/m^3, and a depth of 5 km (See discussion of parameter values in Section 2.3), the constraint on the magma reservoir geometry can be expressed as :

$$a_c^2 b_c \approx 27.5 (\frac{Q_{max}}{100 km^3/yr}) km^3 \tag{75}$$

Thus, a typical magma reservoir semi-major axis for an individual flood basalt eruption required to match the observed eruptive volume fluxes is ~ 5km for an aspect ratio $b_c/a_c \sim 0.2$.

We next include a time-dependent flux from a secondary reservoir as well as viscous relaxation by numerically solving the coupled ODE system for the two (or more) reservoirs. In order to include the effect of a low-viscosity ($\eta_{cr,shell}$) visco-elastic shell in our analysis, we have included an additional faster viscous relaxation term from a visco-elastic shell surrounding the magma reservoirs analogous to the far field pressure relaxation term. The effective viscosities of the shell for magma reservoirs 1 & 2 are $\tilde{\eta}_{cr,shell,1}$ and $\tilde{\eta}_{cr,shell,2}$ respectively. These viscosities have been defined in order to provide an analog of the characteristic timescale for stress relaxation in the no recharge limit $t_{R,relax\ compress}$- $t_R/(1+\beta\alpha)$ (Segall, 2016, See results in previous section). The final set of equations are as follows :

$$\frac{dP}{dt} = -\frac{4K_{cr}P}{3\eta_{cr,1}\tilde{\beta}_{s,1}} - \frac{K_{cr}}{4d_{res,1}\eta_{res,1}} \Big[\frac{P(t) + (\rho_c - \rho_{res,1}) g d_{res,1}}{\tilde{\beta}_{s,1} a_{c,1}^2 b_{c,1}}\Big] \frac{a^3 b^3}{a^2+b^2} + \Omega(t)(P^\infty - P + B_2^1) \frac{K_{cr}}{\pi a_{c,1}^2 b_{c,1} \tilde{\beta}_{s,1} \rho_{res,1}} - \frac{4K_{cr}P}{3\tilde{\eta}_{cr,shell,1}\tilde{\beta}_{s,1}} \tag{76}$$

$$\frac{dP^\infty}{dt} = -\frac{4K_{cr}P^\infty}{3\eta_{cr,2}\tilde{\beta}_{s,2}} - \Omega(t)(P^\infty - P + B_2^1) \frac{K_{cr}}{\pi a_{c,2}^2 b_{c,2} \tilde{\beta}_{s,2} \rho_{res,2}} - \frac{4K_{cr}P^\infty}{3\tilde{\eta}_{cr,shell,2}\tilde{\beta}_{s,2}} \tag{77}$$

$$\frac{db}{dt} \approx \frac{k}{d_{res,1}} \Big[P(t) + (\rho_c - \rho_{res,1}) g d_{res,1}\Big] b \tag{78}$$

$$\frac{da_{c,1}}{dt} = \frac{a_{c,1}}{3} \Big[\beta_{cr,1} \frac{dP}{dt} + \frac{P}{\eta_{cr,1}} + \frac{P}{\tilde{\eta}_{cr,shell,1}}\Big] \tag{79}$$

$$\frac{da_{c,2}}{dt} = \frac{a_{c,2}}{3}\Big[\beta_{cr,2}\frac{dP^{\infty}}{dt} + \frac{P^{\infty}}{\eta_{cr,2}} + \frac{P^{\infty}}{\tilde{\eta}_{cr,shell,2}}\Big] \tag{80}$$

$$\frac{d\rho_{res,1}}{dt} = \rho_{res,1}\beta_{res,1}\frac{dP}{dt} \tag{81}$$

$$\frac{d\rho_{res,2}}{dt} = \rho_{res,2}\beta_{res,2}\frac{dP^{\infty}}{dt} \tag{82}$$

$$\tilde{\eta}_{cr,shell,1} = \eta_{cr,shell,1}\Big[\frac{3(1-\nu)}{(1+\nu)}\Big]\frac{1}{1+\beta_1\alpha_1}\Big(\frac{a_{c,out,1}}{a_{c,1}}\Big)^3 \tag{83}$$

$$\tilde{\eta}_{cr,shell,2} = \eta_{cr,shell,2}\Big[\frac{3(1-\nu)}{(1+\nu)}\Big]\frac{1}{1+\beta_2\alpha_2}\Big(\frac{a_{c,out,2}}{a_{c,2}}\Big)^3 \tag{84}$$

$$\alpha_1 = \frac{3(1-\nu)}{(1+\nu)}\Big[\Big(\frac{a_{c,out,1}}{a_{c,1}}\Big)^3 - 1\Big] \tag{85}$$

$$\alpha_2 = \frac{3(1-\nu)}{(1+\nu)}\Big[\Big(\frac{a_{c,out,2}}{a_{c,2}}\Big)^3 - 1\Big] \tag{86}$$

$$\beta_1 = \frac{\beta_{cr,1}}{\beta_{cr,1} + \beta_{res,1}} \tag{87}$$

$$\beta_2 = \frac{\beta_{cr,2}}{\beta_{cr,2} + \beta_{res,2}} \tag{88}$$

Here, $a_{c,out,1}$ and $a_{c,out,2}$ are the semi-major axis of the crustal viscous shell. We readily acknowledge that this additional term only qualitatively captures the behavior of the system in an ellipsoidal geometry, the spatial pattern of stress relaxation and timescale will not be exactly the same, especially near the free surface (Karlstrom & Richards, 2011). Additionally, as illustrated in the no-recharge limit for the visco-elastic shell model, the maximum relaxation of the over-pressure from the viscous relaxation is $P(t)_{lim\ t->\infty} = P_0^+/(1+\beta\alpha)$ as opposed to the formalism here. Nevertheless, the addition of this term allows us to first order capture a short term response of the system. An eruption will stop when the advective heat flux through the dike is insufficient to keep it open. Thus, we terminate the calculation when the Peclet number (the ratio of timescales for diffusive to advective heat transport) reduces to less than unity. Mathematically, this implies that $\mathrm{Pe} = (b^2/\kappa)/(d_{res}/v_{dike}) < 1$ where κ is the thermal diffusivity and v_{dike} is the magma flow rate in the dike. Finally, analogous to the REAFC model above, the rate of change of the elemental mass m_{ch} of a magma reservoir is :

$$dm_{ch} = dM_e C_{ch} + dM_{re} C_{re} \tag{89}$$

Here, C_{ch} is the element's concentration in the magma reservoir and C_{re} is the element's concentration in the magma recharge. dM_e (negative) and dM_{re} (positive) are the mass changes due to eruption and recharge from other magma reservoirs, respectively.

2.3 1D thermal model

2.3.1 Model setup and assumptions

We use a 1-D thermal diffusion model to calculate the time-evolving background crustal temperature structure due to the emplacement of vertical dike-shaped crustal magma bodies following Karlstrom et al. (2017) (note that given the 1D model horizontal sills will be just a single point). The melt is emplaced over a stochastic range of depths with the total heat input dependent on the specified melt flux rate at the base of the crust. Over time, the increasing crustal temperature leads to a reduction in crustal viscosity and permeability as well as slower cooling of magma bodies. Using the framework of a thermo-chemical magma reservoir box model and associated timescales (Degruyter & Huber, 2014; Mittal & Richards, 2019), we assess how these changes impact the likelihood of different size magma bodies to accumulate melt or erupt to the surface. In addition, the timescales help illustrate the dominant mecha-

nism for the build-up of the critical overpressure for the reservoirs that may erupt. We also systematically assess how this likelihood changes as a function of crustal depth.

Given our 1D model, we cannot directly include a number of important physical processes such as 3D viscous deformation around magma bodies, emplacement, and growth of laterally extensive magma bodies, and the role of pre-existing crustal structure and heterogeneity (Karakas & Dufek, 2015; Karakas et al., 2017; Colón et al., 2019). Following Karlstrom et al. (2017), our 1D thermal model does not include an explicit melt component in the crust with individual dikes instantaneously transfering their heat content into the crust upon emplacement. Finally, we do not explicitly model the thermo-chemical evolution of the magma reservoir and the corresponding changes in the melt, crystal, and volatile content, as well as crustal assimilation and the associated release of volatiles (e.g., Black & Manga, 2017; Beinlich et al., 2020). Although the inclusion of these processes is essential for a full magmatic system model (e.g., Black & Manga, 2017), it would introduce additional, not well constrained, model parameters, choices about magmatic architecture, as well as significant numerical complexity. Since our primary focus in this analysis is calculating how the crustal thermal structure evolves over time, we contend that our 1D model framework provides a reasonable first-order estimate. Furthermore, our model framework permits a broad parameter space exploration. Thus, despite simplifications, the 1D thermal model coupled with magmatic timescale (Degruyter & Huber, 2014; Mittal & Richards, 2019) helps constrain the conditions required for frequent magma eruptions and the crustal location of the corresponding magma bodies.

2.3.2 Magmatic timescales

We calculate crustal thermal evolution using a 1D finite difference method (Langtangen & Linge, 2017) allowing a depth dependent thermal conductivity profile with continuous dike intrusions in a specified depth range (L^{rng}_{dike}). The crustal thermal profile evolves from a steady state geotherm to an elevated temperature due to the additional heat input from dikes. We follow Karlstrom et al. (2017) for the model setup and parameters and refer the reader to their paper for details and model justifications. Following Roland et al. (2010); Cao et al. (2019), we implement the effect of hydrothermal cooling in the upper crust (top 8 km) by modifying the thermal conductivity based on a Nusselt number (See the respective papers for details). Given the significant thermal input associated with a CFB, we choose Nu = 8 for all our calculations. The primary variables for the 1D model are the input melt volume flux and the time-period (T_{period}) of the sinusoidal variation in the volume flux, with the volume flux defined as $Q_{melt}(t) = Q_0\pi \sin(2\pi\ t/T_{period})$. We can define two characteristic non-dimensional numbers for this system

$$\mathrm{De}_{Maxwell} = t^c_{Maxwell}/t^c_{fill} \tag{90}$$

$$\mathrm{Tr}^{cr} = T_{period}/t^c_{diff,intr} = T_{period}/[(L^{rng}_{dike})^2/\kappa_{cr}] \tag{91}$$

$$\tag{92}$$

Here Tr^{cr} quantifies the variability in melt supply to the crust by scaling it with a thermal diffusion time for the vertical length-scale L^{rng}_{dike} over which volume flux Q_0 is uniformly distributed (Karlstrom et al., 2017). On a crustal scale if $\mathrm{De}_{Maxwell} > 1$, the magma reservoir can erupt before the stresses viscously relax, whereas $\mathrm{De}_{Maxwell} < 1$ implies a regime where magma accumulation is favored (Karlstrom et al., 2017). If Tr^{cr} is much greater than one, i.e., the magma supply varies significantly with time, the thermal cooling between successive dike intrusions is appreciable and as a result, the crustal heating by intrusions is reduced.

The eruptive dynamics of a magma reservoir can be defined, to first-order, by a set of characteristic timescales (Degruyter & Huber, 2014; Mittal & Richards, 2019; Townsend et al., 2019) : a timescale for viscous relaxation ($t^c_{viscous}$), timescale for

pressurization by melt recharge t^c_{fill}, timescale for cooling and crystallization t^c_{cool} to a typical crystal fraction (ϵ_0) based on an energy balance (Karlstrom & Richards, 2011) and a pore pressure diffusion timescale $t^c_{press\,diff}$ (Mittal & Richards, 2019). These timescales characterize the likelihood of magma eruptibility as well as the physical mechanism leading to magma overpressure (See discussion in Mittal & Richards, 2019). The timescales are defined as :

$$t^c_{viscous} = \eta_{crust}/(\Delta P) \tag{93}$$

$$t^c_{fill} = V/Q_0 \tag{94}$$

$$t^c_{cool} = \epsilon_0 V \Big(\frac{\oint_{res} q(\Delta T) dA}{\rho_{res} L_f} - \frac{Q_0 c_p \Delta T}{L_f} \Big)^{-1} \tag{95}$$

$$t^c_{press\,diff} = \frac{b_c^2}{4\kappa_{pd}} \tag{96}$$

where η_{crust} is temperature dependent viscosity defined as follows $\eta_{crust}(T) = A\exp(G/RT)$ with A = 4.25 x 10^7, R = 8.31 (gas constant), G = 141 x 10^3 (activation energy), and T the temperature in Kelvin (Karlstrom et al., 2017). Q_0 is the melt flux into the magma reservoir which is calculated by integrating the linear melt flux at the base of the mantle over an area equal to the square of the crustal thickness (Karlstrom et al., 2017). In the cooling timescale, ΔT is the magma temperature decrease below the liquidus , $q(\Delta T)$ is the heat flux from the magma reservoir into the surrounding crust, $\oint_{res} q(\Delta T) dA$ is the heat flux integrated over the area of the magma reservoir, c_p is the specific heat capacity, and L_f is the latent heat of fusion. For the pressure diffusion timescale, we choose the typical lengthscale for diffusion to be $b_c/2$ as the shell outside the reservoir and κ_{pd} is the pore-pressure diffusivity. As described in Mittal and Richards (2019), the pressure diffusivity is defined as $\kappa_{pd} = k^m M_B/\eta_{fluid}$ where k^m is the crustal permeability, η_{fluid} is the fluid viscosity ($\sim 10^{-4}$ Pa s), and M_B is the crustal Biot modulus (= 5.59 x 10^{10} Pa for Westerley granite). Since crustal permeability is expected to be smaller at depth due to higher temperatures and increasing lithostatic pressure (Ingebritsen & Gleeson, 2017) as well as be decreased with higher temperatures due to ductile flow, we approximate the time-varying permeability around a magma reservoir using the following functional form with exponential temperature and depth dependence (e-folding distance of 5 km, Ingebritsen & Manning, 2010):

$$k^m(T, d_{res}) = k_0^m [1 - \exp(-20/T)] \exp(-d_{res}/5000) \tag{97}$$

with k_0^m = 1 x10^{-18} m^2 and temperature T in ^{o}C. Although the permeability around a magma reservoir can have significant transient variations associated with loss of exsolved magma fluids, eruptions and dike formation as well as tectonic and far field stress perturbations, the processes involved are complex and require a full multi-physics analysis (See Mittal & Richards, 2019, and references therein). Consequently, we have chosen the above form as a first order approximation to illustrate the importance of passive volatile loss on magma eruptibility. In addition, we use the solubility calculations to ensure that the there are sufficient exsolved volatiles (volatile volume fraction $\epsilon_g > 0.0075$) in the magma system for this mechanism to be applicable. Otherwise, the permeability value is set to zero. We emphasize that our parameter choice is fairly conservative, both with regards to temperature and depth scaling, given available permeability measurements for geothermal-metamorphic regions (Ingebritsen & Manning, 2010; Stober & Bucher, 2015).

The heat flux around an ellipsoidal magma chamber can be estimated using spatial gradients for a steady state temperature profile (Moons & Spencer, 1988; Karlstrom & Richards, 2011) :

$$q(\xi, \phi) = \frac{k\Delta T}{cot^{-1}(\xi_0)(1+\xi^2)} \sqrt{\frac{1+\xi^2}{(a_c^2 - b_c^2)(\xi^2 + \phi^2)}} \tag{98}$$

Here ϕ is the scaled polar co-ordinate ($= \sin\chi$) and ξ ($= \sinh\mu$) is a scaled distance from the reservoir wall with μ and χ ($\in [\pi/2, \pi/2]$) being the radial and polar coordinate the oblate spheroidal coordinate system. The surface of the oblate ellipsoid is defined by $\mu = \mu_0$ with $\tanh(\mu_0) = b_c/a_c$ For our calculations, we integrate the heat flux over the ellipsoid surface at the reservoir-crust interface ($\xi = \xi_0$). Consequently, the integral flux term $\oint_{res} q(\Delta T) dA$ is :

$$\oint_{res} q(\Delta T) dA = 2\pi a_c \int_{-c}^{c} q(\Delta T, \xi_0, z/b_c) \sqrt{1 + \frac{(a_c - b_c)(a_c + b_c) z^2}{b_c^4}} dz \tag{99}$$

$$= \frac{2\pi a_c k \Delta T}{cot^{-1}(\xi_0)(1+\xi_0^2)} \sqrt{\frac{1+\xi_0^2}{(a_c^2 - b_c^2)}} \int_{-c}^{c} \sqrt{1 + \frac{(a_c - b_c)(a_c + b_c) z^2}{b_c^4}} \frac{1}{\sqrt{\xi_0^2 + (z/b_c)^2}} dz \tag{100}$$

where we have used the surface integral equation for an oblate spheroid and the relationship between ϕ and the Cartesian co-ordinate z ($\phi = z/b_c$). We numerically calculate this integral to calculate the total heat flux from the surface of the magma reservoir.

2.4 Model Parameters

2.4.1 Elastic Compressiblity

We calculate the elastic compressibility for ellipsoidal magma reservoirs using the results of the numerical finite element calculations from K. Anderson and Segall (2011) in an elastic half space as a function of aspect ratio b_c/a_c. We use the numerical results for the medium-deep regime when the depth of the magma reservoir is larger than the semi-major axis a_c and shallow results otherwise. We also extrapolate to lower aspect ratios (< 0.5) outside the numerical calculations using the analytical expressions from Amoruso and Crescentini (2009) for full elastic space - $\beta_{cr} = 3/(4K_{cr})[(a_c/b_c)(2/\pi) - 4/5]$. Although the free surface effects are likely important for spatially extensive magma reservoirs, the lack of simple analytical expressions makes it difficult to accurately model within our framework and using the analytical solution in the regions outside the numerical region enable us to capture the first order behavior.

2.4.2 Magmatic volatile solubility

Since the magmatic volatiles have a strong impact on the magma compressibility (e.g., Rivalta & Segall, 2008), it is important to include the presence of magmatic volatiles (CO_2 and H_2O) in the magma mixture. We calculate the joint solubility of the magmatic volatiles (CO_2 and H_2O) in the melt using the equations described in Iacono-Marziano et al. (2012). If the volume fraction of the magmatic volatiles in the magmatic mixture is very high, the volatiles will likely be passively lost from the reservoir even without any eruption due to their high buoyancy w.r.t the surrounding crust (See discussion in Mittal & Richards, 2019). Hence, we cap the maximum volume fraction of volatiles in the magmatic reservoir to 20 % as an upper limit (Aarnes et al., 2012). In order to calculate the exsolved magmatic volatiles at a given magma reservoir depth, we either assume a closed system degassing path wherein exsolved volatiles remain in the system (upto a maximum of 20% volume fraction) or a partial open system degassing where some fraction of the exsolved volatiles at each depth are lost from the system and passively degassed. These different exsolution paths affect both the depth when water starts exsolving from the melt as well as the bulk density and compressibility of the magma reservoir.

We calculate the initial concentrations of water and CO_2 in the melt by starting with a chosen mantle source composition and using partition coefficients to calculate

the volatile content (X_{melt}) in the melt given a degree of partial melting (F):

$$X_{melt} = \frac{X_{mantle}}{D + F(1 - D)} \tag{101}$$

Following (Black & Manga, 2017), we set the bulk partition coefficient D to be 0.01 for water (Katz et al., 2003) and 10^{-4} for CO_2 (Hauri et al., 2006) assuming oxidizing redox conditions (Rohrbach & Schmidt, 2011; Stagno et al., 2013). Although there is considerable uncertainty regarding the initial mantle volatile (CO_2, H_2O) composition (e.g., Self et al., 2014) and references therein), there is increasing evidence that the mantle source of Phanerozoic LIPs is volatile enriched compared to the background mantle (Gu et al., 2019; Capriolo et al., 2020). The typical range of water content ranges from 0.1 to 0.6 wt % (X.-C. Wang et al., 2016; Liu et al., 2017; Ivanov et al., 2018; Gu et al., 2019) with the real values closer to the upper end since measurements are biased by pre-eruptive degassing. With regards to mantle CO_2 contents, K. R. Anderson and Poland (2017) estimated that the Hawaiian mantle plume has a CO_2 content of 964 ppm (with a 68 % range from 740 to 1230 ppm) while Matthews et al. (2020) infered that the Iceland plume has a CO_2 concentration of $\sim$ 2.2 wt% ($\pm$1.5 wt %). These results are broadly consistent with estimates from Lange (2002) arguing for more than 4 wt % concentration of CO_2 and H_2O in the CRB melt (for a typical melt fraction of 5-15%) in order to ensure their buoyancy. The frequent presence of mantle composition sulphides, as well as carbonatitic and hydrous assemblages in the SIP ultramafic intrusions also support the presence of a significant volatile flux into the system throughout the CFB event (Larsen et al., 2018). Additionally, the metasomatized mantle lithosphere may also contribute significant C to the parental melt reaching the crustal system (e.g., Black & Gibson, 2019; Gibson et al., 2020). Based on these results, we assume a higher mantle volatile composition than Black and Manga (2017) with a conservative value of 750 ppm CO_2, and 0.23 wt % H_2O. This parameter set ensures that the partial melt water content for 10 % degree partial melting is $\sim$ 2 wt %, consistent with some melt inclusions results from the Deccan Trap Wai sub-group (Choudhary et al., 2019) and some estimates from the Réunion lava flows (Boudoire et al., 2018). Also, the melt CO_2 is typically order 0.5-1 %, which is consistent with petrologic and melt inclusion estimates from Deccan, Columbia River Basalts, and Central Atlantic Magmatic Province (Self et al., 2006; Capriolo et al., 2020).

As discussed in Section 3 (Paper I), there is a general consensus that the primary plume derived melt was picritic (K. G. Cox, 1980; Sen & Chandrasekharam, 2011; Chatterjee & Sheth, 2015; K. V. Kumar et al., 2018; Dongre et al., 2018). Consequently, we use the estimate of the primary melt composition modeled from the most primitive picrite from Deccan Traps (Pavagadh Picrite) as well a Deccan lava flow average for our solubility calculations (Sen & Chandrasekharam, 2011; K. V. Kumar et al., 2018). We acknowledge that actual magma compositions will evolve through REAFC processes in the magmatic system. However, a comprehensive analysis of different magma compositions is beyond the scope of this study and does not influence our primary results. Additionally, the dominance of a tholeiitic composition in Deccan Traps suggest that although fractional crystallization was extensive, only small volumes of intermediate and high silicic rocks (e.g., rhyolites) were produced. In Fig.8, we show the solubility curves (for different choices of open system degassing fraction, See (Mittal & Richards, 2019) for a discussion of passive degassing observations and mechanisms) for two different melt compositions (Deccan average vs Pavagadh Picrite) and two different mantle volatile contents (F = 10% M. Richards et al., 2013). The main feature of note with these calculations is that CO_2 can exsolve from the melt at fairly deep depths (order 20-30 km) whereas H_2O can remain soluble up until shallow depths (order 3-6 km). Thus, any buoyancy driven over-pressurization due to H_2O volatiles will be a significant process only in the upper crust whereas the CO_2 associated buoyancy dominates for the deeper crustal reservoirs. The upper limit on the

amount of magmatic volatiles in these calculations is set by the requirement that the volatile volume fraction is always less than 20%. With decreasing lithostatic pressure, the decrease in density of the volatile phase leads to a strong reduction in the total CO_2 and H_2O. Additionally, we show the results for a range of degassing efficiency from 0 (closed system) to 80 % in Figure 2 for each scenario. The results illustrate that the choice of open system degassing fraction can have a substantial impact on the melt solubility through differences in the amount of the exsolved volatile phase which is in equilibrium with the melt. For the rest of our analysis, we use the Deccan primitive composition (Pavagadh Picrite) and a mantle volatile composition of 750 ppm CO_2 and 0.23 wt % H_2O with a relatively closed system configuration (degassing efficiency of less about 5 %) unless otherwise noted.

2.4.3 Other parameters

To calculate the melt-crystal-exsolved fluid mixture density and compressiblity, we use the modified Redlich-Kwong equation of state for magmatic fluids from Halbach and Chatterjee (1982) (See Degruyter and Huber (2014) for details). The density of the melt and the crytals depend on the melt compostion as well as depth, and volatile content, all of which will be evolving during the magmatic system evolution. However, to first order, we can use a simplified, conservative constant melt density linearly increasing from 2500 kg/m^3 from shallow depths (5 km depth, constant for depths less than 5 km) to 2700 kg/m^3 for deeper depths (30 km) based on the pMELTS calculations from Karlstrom and Richards (2011) for approximately 30 % crystal fraction (as well as typical parameters from Piombo et al., 2016; A. Aravena, Cioni, de' Michieli Vitturi, et al., 2018) while we conservatively set crystal density to be 3000 kg/m^3 to represent ultramafic crystalized cumulate. Similarly, for simplicity, we set the compressibility of melt and crystals to 2 x 10^{-10} Pa^{-1} and 2 x 10^{-11} Pa^{-1} respectively (K. Anderson & Segall, 2011). We emphasize that these simplifications significantly reduce the model complexity and allow a more clear physical analysis of the model, thus allowing us to capture the first order behavior. A fully coupled petrological analysis, though important, is beyond the scope of this study and does not affect the primary conclusions of our analysis. We set the crustal effective elastic modulus to 10 GPa and Poisson's ratio to 0.25 (Karlstrom et al., 2017).

For the crustal density and conductivity structure, we use a simplified piecewise linear relationship using the results from Jennings et al. (2019) and DeBari and Greene (2011) for a typical continental crustal section. We set the viscosity of the basaltic magma at $\sim$ 1000 Pa-s based on field based measurements for Hawaiian lava flows which are reasonable analogs for flood basalt lava flows both in terms of composition and eruptive style (Chevrel et al., 2019).

For all our calculations, we set the dike semi-major axis (a)to 500 m and the initial dike semi-minor axis (b) to be equivalent to that required for an initial Peclet number of 2. For a typical magma reservoir depth of 5 km (and other parameters described above), the initial dike width is 0.25-1 m. These values are very consistent with the lower range of DT dike thickness (Section 5, Paper I) representing the single injection dikes. With regards to dike length, our chosen value of a 1 km long active segment is broadly consistent with modern CFB analogs such as the Laki 1783 eruption (Thordarson & Self, 1993) when accounting for flow localization within the dikes and the region of active magma flow within a dike segment (Bruce & Huppert, 1990; Fialko & Rubin, 1999; Wylie et al., 1999; Brown et al., 2007; Taisne & Tait, 2011; Parcheta et al., 2015). We find that changing the dike shape within reasonable ranges does not significantly change our results, especially given other parameter uncertainties. A more comprehensive analysis of the whole parameter space is beyond the scope of this study.

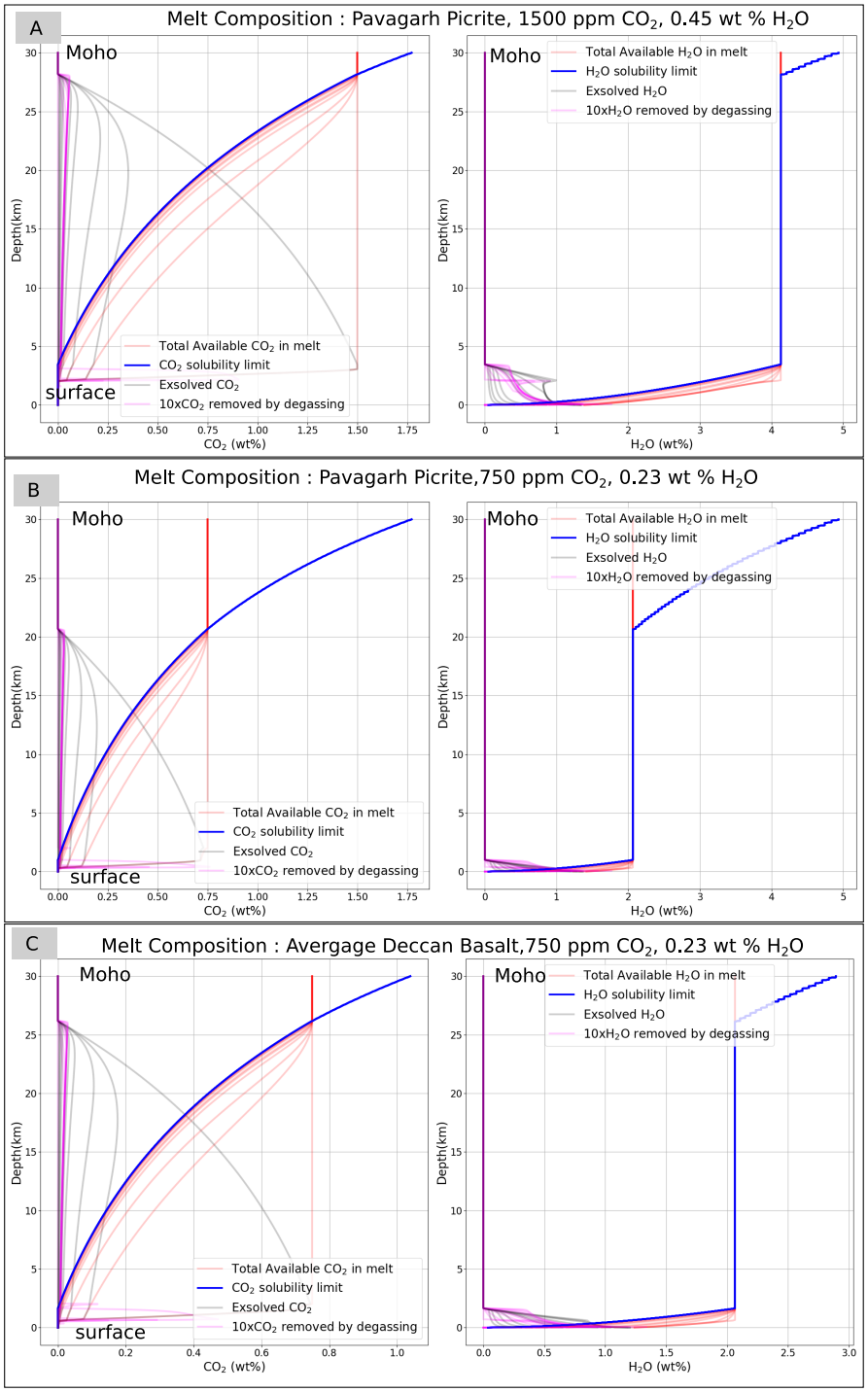
A
Melt Composition : Pavagarh Picrite, 1500 ppm CO_2, 0.45 wt % H_2O
Moho
surface
Depth(km)
CO_2 (wt%)
H_2O (wt%)
Total Available CO_2 in melt
CO_2 solubility limit
Exsolved CO_2
10xCO_2 removed by degassing
Total Available H_2O in melt
H_2O solubility limit
Exsolved H_2O
10xH_2O removed by degassing
B
Melt Composition : Pavagarh Picrite,750 ppm CO_2, 0.23 wt % H_2O
C
Melt Composition : Avergage Deccan Basalt,750 ppm CO_2, 0.23 wt % H_2O

Figure 2

Figure 2 *(previous page)*: Joint solubility of the magmatic volatiles (CO_2 - Left panels, and H_2O- Right panels) in the melt for 2 different primitive melt composition estimates (Panel B and C) as well as two different initial mantle volatile compositions (Panel A and B). The initial concentrations of water and CO_2 in the melt are calculated for 10% degree of partial melting. In the plots, the degree of magmatic volatiles lost at each depth increases from 0% to 80 % (different gray lines) illustrating how the magmatic volatile content changes as the system moves from a closed system to an unbuffered open-system behavior. The exsolution of CO_2 occurs fairly deep in the crustal column whereas H_2O comes out from the melt at shallow depths for all compositions.

3 Model results - Magma Reservoir Model

We use our new visco-elastic mechanical model for an ellipsoidal magma reservoir described in Section 2.1 to calculate how eruptive volume fluxes (km^3/year) and the total erupted volumes of each flow unit (or equivalently the typical duration of each eruptive event) depend on reservoir geometry, and the crustal properties. We are particularly interested in finding what magmatic architecture is required to match the CFB observations constraints (Section 3.3 - 3.5, Paper I). The typical ranges of eruptive fluxes and volumes of individual CFB eruptive episodes are 30-300 (km^3/year) and 1,000 - 10,000 km^3, respectively. The absence of significant a'a flows in most CFB provinces suggest that the eruption rates did not exceed more than a few thousand km^3/year at best (Section 3.5, Paper I). In the following, we first discuss results for a spherical magma reservoir followed by the ellipsoidal reservoir.

3.1 Spherical Reservoir Model

Typical magma reservoirs associated with CFBs are expected to have a high aspect ratio, especially for the hypothesized large (> 100 km long) magma reservoirs (e.g., Section 2, 4 & 5, Paper I). Thus, the choice of a spherical geometry seems an unreasonable choice. Nevertheless, starting with a spherical reservoir model enables us to directly compare and contrast our results with those from previous studies (Huppert & Woods, 2002; Woods & Huppert, 2003; Piombo et al., 2016; Townsend et al., 2019; Townsend & Huber, 2020b).

In Figures 9 and 10, we show model calculations for a range of magma reservoir radius. The depth of all the reservoirs is 5 km, representative of an upper crustal magma body. We note that for most of the reservoir sizes, a 5 km depth is not physical since the top of the magma body will exceed the free surface. However, changing the magma reservoir depth for each reservoir size would make it more complicated to compare the results since the volatile exsolution, magma mixture buoyancy, and crustal properties are all depth-dependent. Thus, for these calculations, we keep the nominal reservoir depth the same. We consider more physical magma reservoirs in the subsequent section. In order to match the observational constraint for eruptive volume flux (Figure 3A, top panel), we set the dike width to be 1 m. The far-field crustal viscosity and the visco-elastic shell radius is fixed at 10^{21} Pa-s and $R_2 = 1.5R_1$ (Segall, 2016) for all results shown here.

First, we consider the case of no magma recharge from the underlying reservoir (conductivity = 10^{-6} Kg/Pa-s) and a relatively cold visco-elastic shell ($\eta_{cr,1} = 10^{20}$ Pa-s). The total duration of the eruption is set by t_{flux} (Eqn. 26, Table 1), which is proportional to the magma reservoir volume. For our chosen parameters, the eruption duration is less than a year, much shorter than CFB observations. Additionally, the

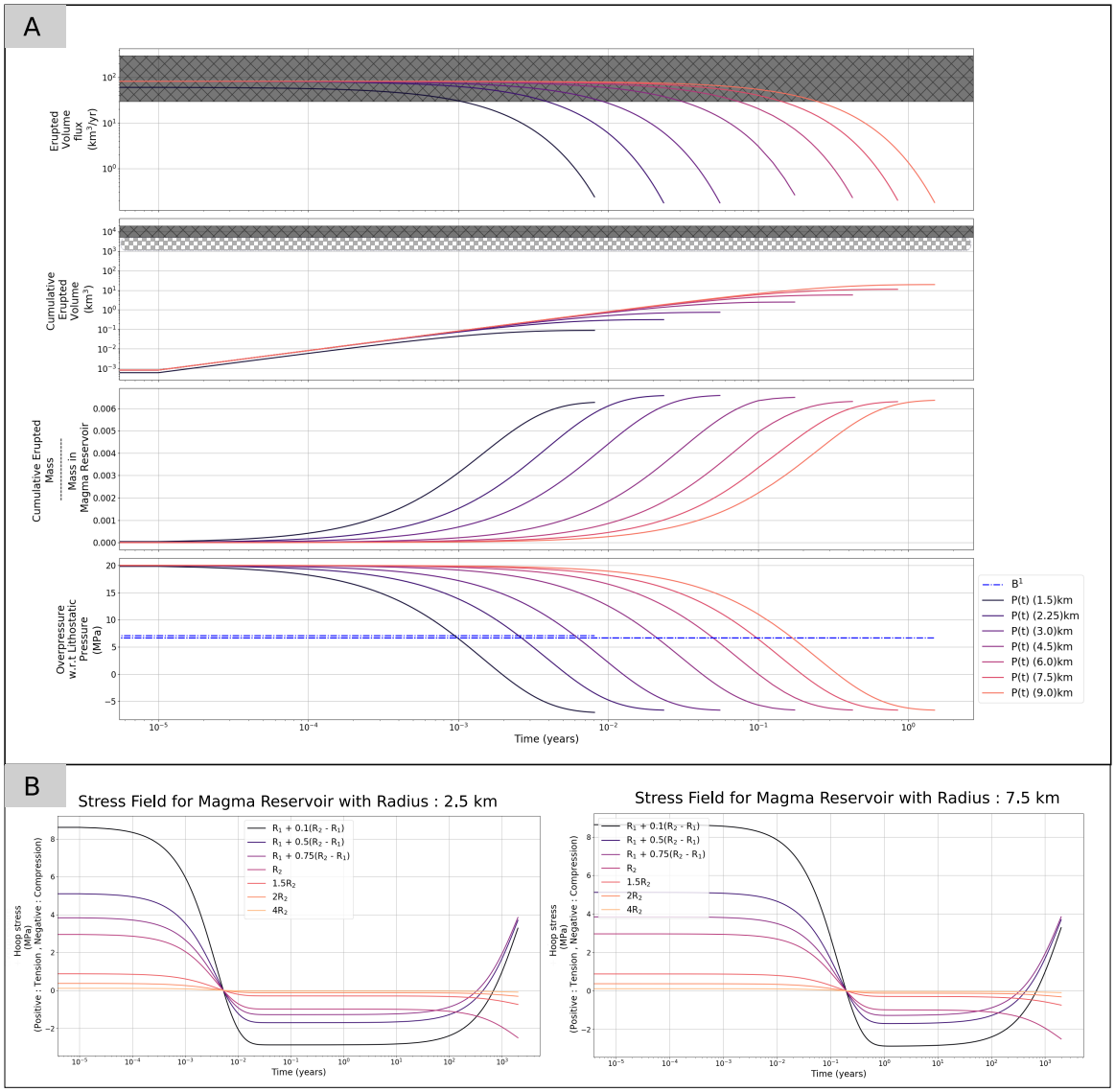

Figure 3: Model Results for Spherical Reservoir Model : Erupted volume flux (km^3/yr), total erupted volume (km^3), fraction of magma chamber mass erupted, and magma reservoir overpressure (Pa), for different reservoir radius (Panel A, see legend in the figure) at a typical upper crustal depth of 5 km. The viscosity of the surrounding crust is set to 10^{20} Pa-s and the conductivity is set to 10^{-6} Kg/Pa-s. A range of eruptive volume fluxes (30-300 km^3/year) and total erupted volumes (1,000 - 5,000 km^3 : hashed region & 5,000 - 10,000 km^3 : shaded hashed region) for flood basalts based on observational constraints is shown on the figure. The Panel B show the time-evolving total pressure for 2 different radius magma reservoirs at different distances outward from the reservoir wall in the visco-elastic shell. The B^1 curve shows the magma buoyancy overpressure in the conduit. At the termination of the eruption, the total overpressure is zero : $P(t) + B^1 \sim 0$.

erupted volume is too low for model parameters chosen to obtain reasonable eruption rates. This result is a direct consequence of the low eruption efficiency of a spherical magma reservoir (Figure 3A, cumulative erupted mass/mass in magma reservoir curves). Huppert and Woods (2002) showed that the typical erupted volume from an over-pressurized magma reservoir is $\sim V_{res}\beta_{res}\Delta P$ (Also see Townsend & Huber, 2020b). For a typical compressibility of 1-3 x 10^{-10} Pa for a magma mixture with some exsolved volatiles (Rivalta, 2010; Degruyter & Huber, 2014) and $\Delta P \sim 20MPa$ (Rubin, 1995), the erupted volume $\sim 0.002 - 0.006V_{res}$. Even if this value is increased by a factor of 10 with progressive crystallization, higher initial melt volatile content or shallower magma body (Edmonds & Wallace, 2017, also See Figure 8), only a few percent of reservoir volume can erupt. Consequently, an eruption of $\sim$ 5000 km^3 magma volume requires a magma reservoir size of 100,000 - 10^6 km^3 (30-60 km radius) inconsistent with various observational constraints (see section 3, Paper I). We note that the efficiency of eruption can potentially be significantly enhanced when accounting for pressurization by caldera and graben subsidence during the eruption (Gudmundsson, 2016). We also note that in most CFBs, there is no evidence any caldera collapse type features on the surface (See Section 5 and 6, Paper I).

A corollary of the typical low eruption efficiency is that it makes explaining CFB volcanism by the large magma reservoir model (with failure by buoyancy overpressure) even more challenging. Black and Manga (2017) assumed that all the whole fraction of the magma body that is both molten and buoyant erupt once the critical buoyancy, overpressure is reached. However, if only a few percent of the mass erupts, many more reservoir failure events would be required to explain the total CFB volumes. However, each eruption would still be associated with a crustal permeability increase due to fracturing (Ingebritsen & Manning, 2010) and consequent volatile loss. Thus, there should not be a significant reduction in the timescale between individual eruptions if the failure is due to buoyancy overpressure.

An interesting conclusion from our model calculations is that the eruptions do not stop when the magma overpressure reduces back to lithostatic conditions, as is generally assumed in box models (K. Anderson & Segall, 2011; Degruyter & Huber, 2014; Mittal & Richards, 2019; Townsend et al., 2019). Instead, we find that eruptions end with the magma reservoir under-pressurized w.r.t lithostatic conditions (akin to results in Karlstrom et al., 2012). This result is a consequence of the buoyancy of the magma. A magma reservoir erupts mass to the surface until it reaches the magmastatic condition rather than the lithostatic condition. Consequently, in Figure 3A, the sum of magma overpressure and buoyancy term (B^1) is close to zero when eruptions terminate due to insufficient melt flux through the dike. This under-pressure can help increase the magma reservoir eruption efficiency by volatile exsolution driven magmatic siphoning (Karlstrom & Manga, 2009). For some parameter choices, the continued exsolution (and consequent magma buoyancy) can sustain eruptions for a long period. In our model calculations, we include this effect by calculating CO_2 - H_2O solubility and magma density during an eruption. The difference in the magma pressure evolution (i.e. magma under-pressurization rather than zero overpressure) also has a strong influence on the stress pattern in the visco-elastic shell surrounding the reservoir (Figure 3B, top panel).

Initially, the hoop stress ($\sigma^{(1)}_{\theta\theta}$) is positive (tension) due to the initial ΔP. With continuing surface eruptions, the magma overpressure decreases to a negative value, which in turn leads to compressional hoop stresses. With no further melt influx, the eruption eventually stops, but the shear stresses within the shell continue relaxing. This stress relaxation eventually leads to a change in sign of the hoop stress in order to match the radial stress (which is tensional due to magma under-pressure) (timescale of $t_{R,relax\,compress}$; See Segall (2016) for a more detailed discussion). Eventually, on a much longer timescale ($t_{R,Maxwell}$) related to the far-field crustal viscosity (not

shown in the figure), all the stresses in the reservoir will relax. Since the viscous shell is coupled to a surrounding viscoelastic medium (with much higher viscosity), any tensional hoop stress in the shell leads to a corresponding compressional stress in the surrounding crust (curves with $r > R_2$, Figure 3B).

The hoop stresses in the viscous shell are particularly interesting with regards to how the connectivity between magma reservoirs is established. For a dike to propagate into the magma reservoir, the dike's magma pressure within the dike must exceed the least compressive stress tangential to the chamber wall. Thus, with respect to an initial lithostatic stress condition, the excess pressure defined as $\sigma_{\theta\theta} + P_{dike}(t)$ measures the difference between the circumferential compressive stress and magma over-pressure. The condition of tensile failure at a given radial distance from the magma reservoir is when either $\sigma^{(1)}_{\theta\theta}(r,t) + P_{dike}(t) = \Delta P$ (for r $< R_2$) or $\sigma^{(2)}_{\theta\theta}(r = R_2, t) + P_{dike}(t) = \Delta P$ (for r $\geq R_2$). Our results suggest that initially, the rapid under-pressurization will lead to a stress pattern that inhibits fracture propagation both out of and into the magma reservoir. Over time, the hoop stresses become tensional, thus making dike propagation more favorable. In the visco-elastic crust coupled to the shell, there is a similar, but opposite effect. We posit that these stress variations may lead to natural timescales for enhanced connectivity between different magma bodies.

Next, we show some model results where we allow faster stress relaxation in the visco-elastic shell ($\eta_{cr,1} = 10^{18}$ Pa-s; Figure 4A, Left Panel). With lower shell viscosity, stress relaxation in the viscous shell leads to pressurization if the magma mixture is not infinitely compressible (Segall, 2016). This pressurization, in turn, enables continued melt flux into the dike and longer, larger eruptions. We find this process is responsible for the much longer eruption duration, total erupted volume, as well as a higher eruption efficiency of large magma reservoirs (Figure 4A). In contrast, the eruptions from a smaller magma reservoir cease before this mechanism can act (timescale of $t_{R,relax\ compress}$). However, the eruption rate is still too small compared to observational constraints.

Finally, we increase the melt influx into the magma reservoir from a deeper magma body (conductivity $\Omega = 10^{-1}$ Kg/Pa-s, $\eta_{cr,1} = 10^{18}$ Pa-s; Figure 4B, Left Panel). The lower magma reservoir is assumed to be quasi-infinite with a constant lithostatic magma pressure and a depth equal to 5 km plus twice the semi-major axis of the primary reservoir. This depth choice approximates the growing region of influence of a larger magma reservoir (e.g., Karlstrom et al., 2009, 2015). With this model configuration, we do find that many magma reservoirs can satisfy both the eruptive flux and the erupted volume constraints. Physically, melt influx helps maintain magma pressurization (with an associated timescale of t_{repres}, Eqn. 27) akin to the visco-elastic shell. Since the magma-overpressure never decreases below zero for the largest magma reservoir, the hoop stresses remain compressional in contrast to the results for smaller magma bodies (Figure 4B top and bottom panels).

Considering different magma reservoir depths, initial volatile content, and depth of the secondary reservoir, we find a qualitatively similar model behavior as described above. A continuous melt influx from an additional magma reservoir is necessary for feeding an individual eruptive episode from the smaller magma reservoir. There are, however, some critical physical processes that are missing in the spherical reservoir model, e.g., changing dike widths, appropriate reservoir geometry, and a quasi-infinite lower reservoir. Since we do not model pressure evolution in the secondary reservoir, magma transport from the reservoir does not lead to an under-pressurization. Consequently, an extensive secondary reservoir with high conductivity and buoyancy acts as an infinite magma source for the primary reservoir feeding surface eruptions. We relax all of these model assumptions with the results from the Ellipsoidal reservoir model described in the next section.

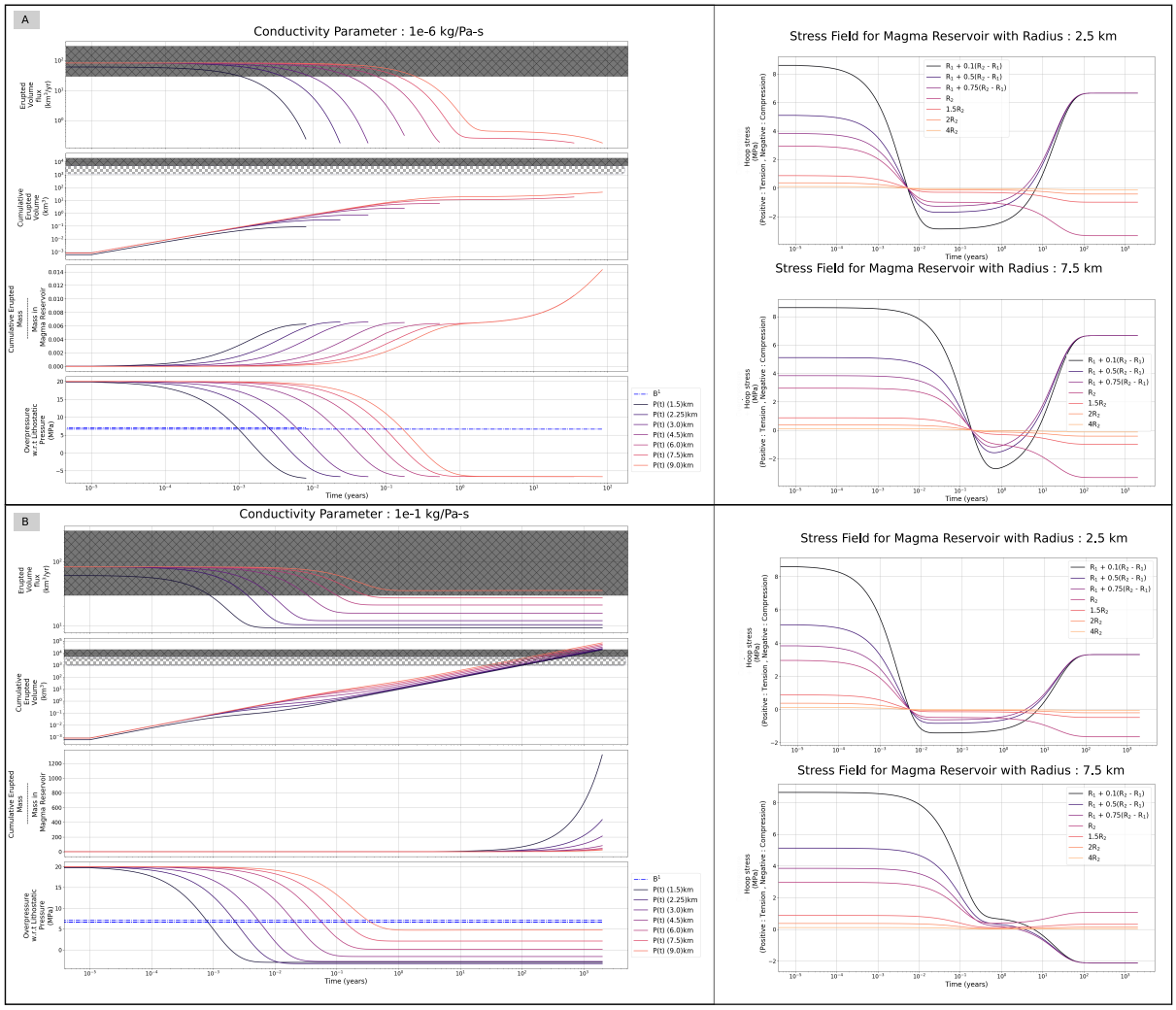

Figure 4: Model Results for Spherical Reservoir Model : Erupted volume flux (km^3/yr), total erupted volume (km^3), fraction of magma chamber mass erupted, and magma reservoir overpressure (Pa), for different reservoir radius (See legend in the figure) at a depth of 5 km. The viscosity of the surrounding crust is set to $\mathbf{10^{18}}$ **Pa-s** and the conductivity is set to 10^{-6} Kg/Pa-s (Part A) and 10^{-1} Kg/Pa-s(Part B). A range of eruptive volume fluxes (30-300 km^3/year) and total erupted volumes (1,000 - 5,000 km^3 : hashed region & 5,000 - 10,000 km^3 : shaded hashed region) for flood basalts based on observational constraints is shown on the figure. The Right Panels for each Part show the time-evolving total pressure for two different radius magma reservoirs at different distances outward from the reservoir wall in the visco-elastic shell. The B^1 curve shows the magma buoyancy overpressure in the conduit. At the termination of the eruption, the total overpressure is zero : $P(t) + B^1 \sim 0$.

3.2 Ellipsoidal Reservoir Model

In the following, we describe our results for the Ellipsoidal reservoir model. We start with the simplest case - an elastic reservoir. We then sequentially add a crustal visco-elastic response, melt influx from a single secondary reservoir, and finally melt influx from four additional reservoirs. The semi-minor axis and depth of the primary reservoir are set to 3 km and 5 km, respectively, for all results unless otherwise noted. We show the model results for a maximum of 10,000 years or when the eruption stops, whichever is faster. The maximum eruption duration should be smaller than 10,000 years given the observational constraints on the duration of individual eruptive episodes (Section 3.3-3.5, Paper I)

3.2.1 Elastic end-member

We first consider an elastic Ellipsoidal magma reservoir in an elastic half-space connected to the surface with an erodible dike-shaped conduit. Using the analytical solutions described in Section 2.1.4, we show the model results for a wide range of reservoir sizes ranging from 2.5 to 75 km (semi-major axis a_c) in Figure 5. These results do not include any crustal stress relaxation or melt influx from other magma reservoirs. In contrast to the spherical reservoir model, the eruption flux initially increases, followed by a subsequent decline and shutdown of eruptions. This difference is a direct consequence of evolving dike widths, which changes both the eruption rate as well as the timescale to relax overpressure by mass loss (t_{flux}; Eqn. 26, Table 1). For instance, the dike width increases from 0.25 m to 20 m by the end of the eruption for the 150 km long magma reservoir (Figure 5, orange curve). The elastic compressibility of a low aspect ratio magma reservoir is much larger than for an equivalent spherical magma body. Thus, the total erupted mass fraction for the largest magma reservoir is about 15 % as opposed to less than a percent in Figure 3.

Still, despite the different model geometry, we find that it is not possible to satisfy the observational constraints on eruptive rate and total volume with a given model geometry. In Figure 6, the results of a wide parameter space exploration show that we need a magma reservoir with semi-major axis $\sim$ 5-10 km to match the eruptive flux estimates of 30-300 km^3/year. But, magma reservoirs that can erupt volumes equivalent to individual CFB eruptive episodes have sizes $a_c \sim 60-100$ km (for a total erupted volume of 5,000-20,000 km^3). The required reservoir size typically increases with decreasing aspect ratios since for the same semi-major axis, smaller aspect ratio implies a smaller total magma reservoir volume. The inversion of this trend at small aspect ratios is due to the rapid increase in elastic compressibility, which in turn increases the eruption efficiency and total erupted volume despite smaller reservoir size.

3.2.2 Visco-elastic crust and melt influx

Next, we enable far-field crustal stress relaxation with the crustal viscosity set to either 10^{19} Pa-s (Figure 7A) or 10^{21} Pa-s (Figure 7B). We find that a lower crustal viscosity allows more rapid relaxation of the magma over/under-pressure akin to the Spherical Reservoir Model results (See Figure 4). This process, in turn, enables longer, larger eruptions with a prolonged low eruption phase. Although this additional eruptive phase decreases the required reservoir size to 30-70 km (for a total erupted volume of 5000-20,000 km^3), this still does not overlap with eruptive rate estimates (Figure 8, crustal viscosity = 10^{19} Pa-s). Additionally, the total duration of an eruptive episode is too long to be consistent with observations. We find a qualitatively similar model behavior when we use lower viscous shell viscosity instead of a lower far-field crustal viscosity.

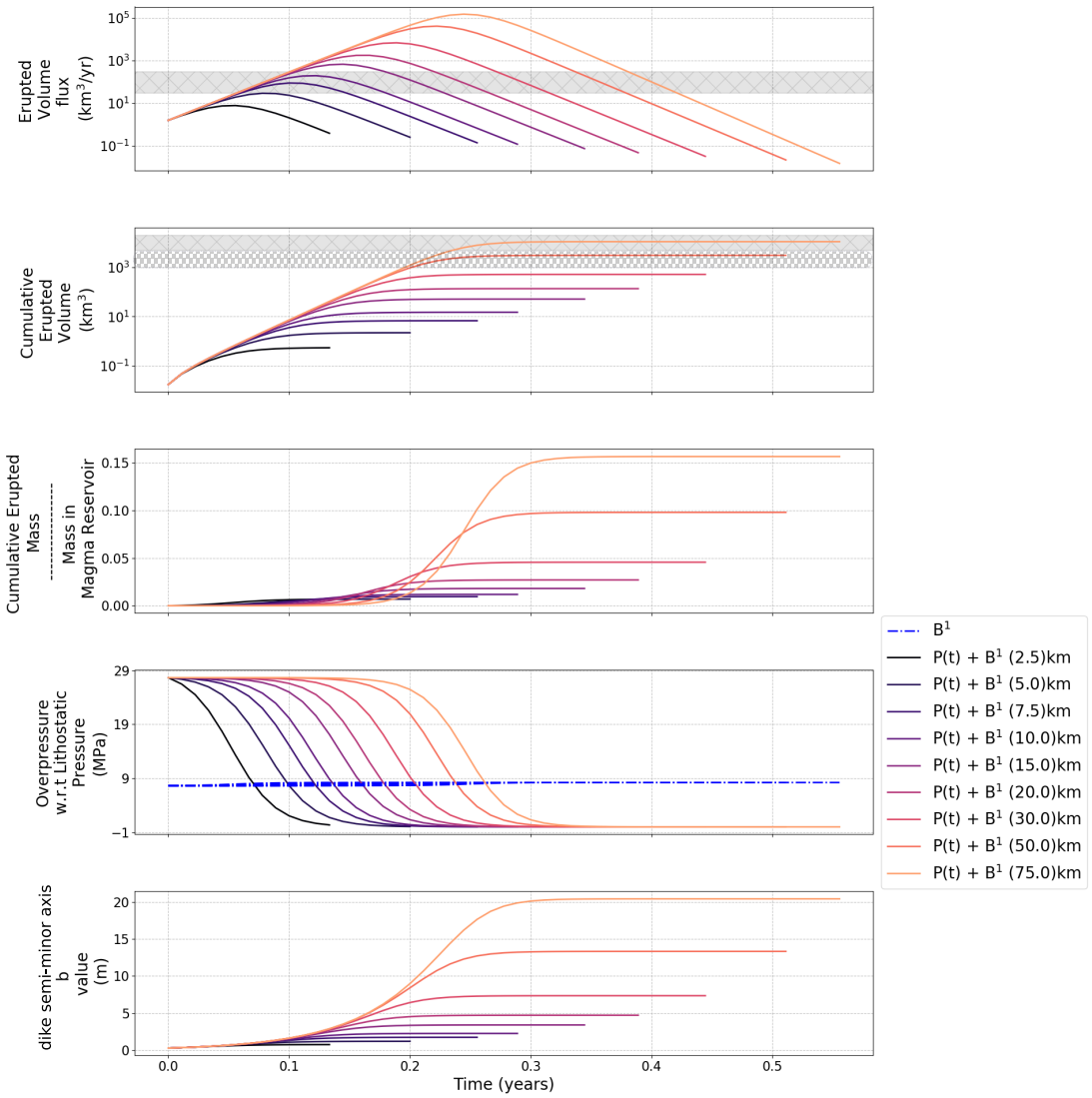

Figure 5: Model Results for Elastic Ellipsoidal Reservoir Model : Erupted volume flux (km^3/yr), total erupted volume (km^3), fraction of magma chamber mass erupted, and magma reservoir overpressure (Pa), and dike width (b). The results are shown for different reservoir semi-major axis sizes (See legend in the figure) with a constant semi-minor axis ($b^c = 3$ km). In this calculation, the crustal stress relaxation and melt influx from additional magma reservoirs is not included. The depth of all the reservoirs is set to 5 km. A range of eruptive volume fluxes (30-300 km^3/year) and total erupted volumes (1,000 - 5,000 km^3 : hashed region & 5,000 - 10,000 km^3 : shaded hashed region) for flood basalts based on observational constraints is shown on the figure.The B^1 curve shows the magma buoyancy overpressure in the conduit. At the termination of the eruption, the total overpressure is zero : $P(t) + B^1 \sim 0$.

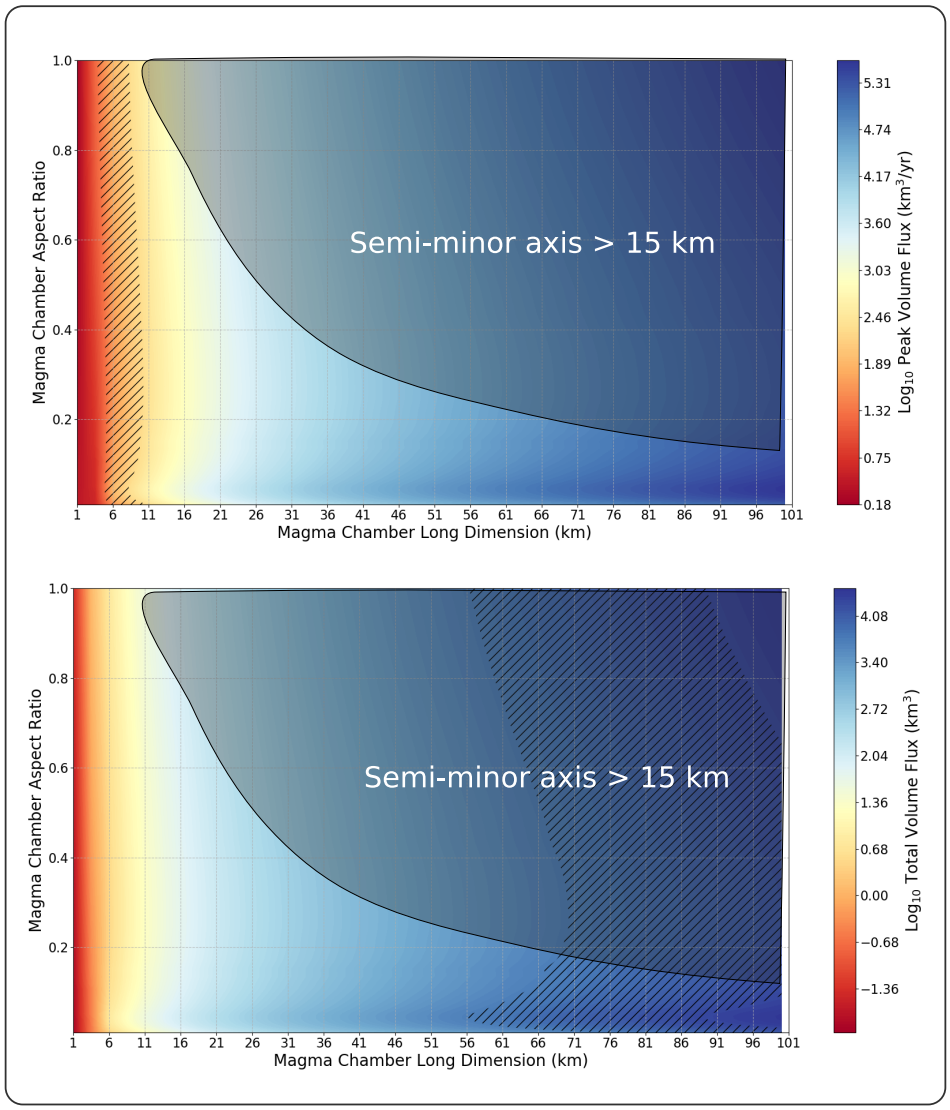

Figure 6: Parameter Space plot for Elastic Ellipsoidal Reservoir Model. A range of eruptive volume fluxes (30-300 km^3/year, Top Panel) and total erupted volumes (5,000 - 10,000 km^3, Bottom Panel) for flood basalts is shaded on the plots. These results clearly illustrate that there is no magma reservoir geometry that can simultaneously satisfy both the constraints.

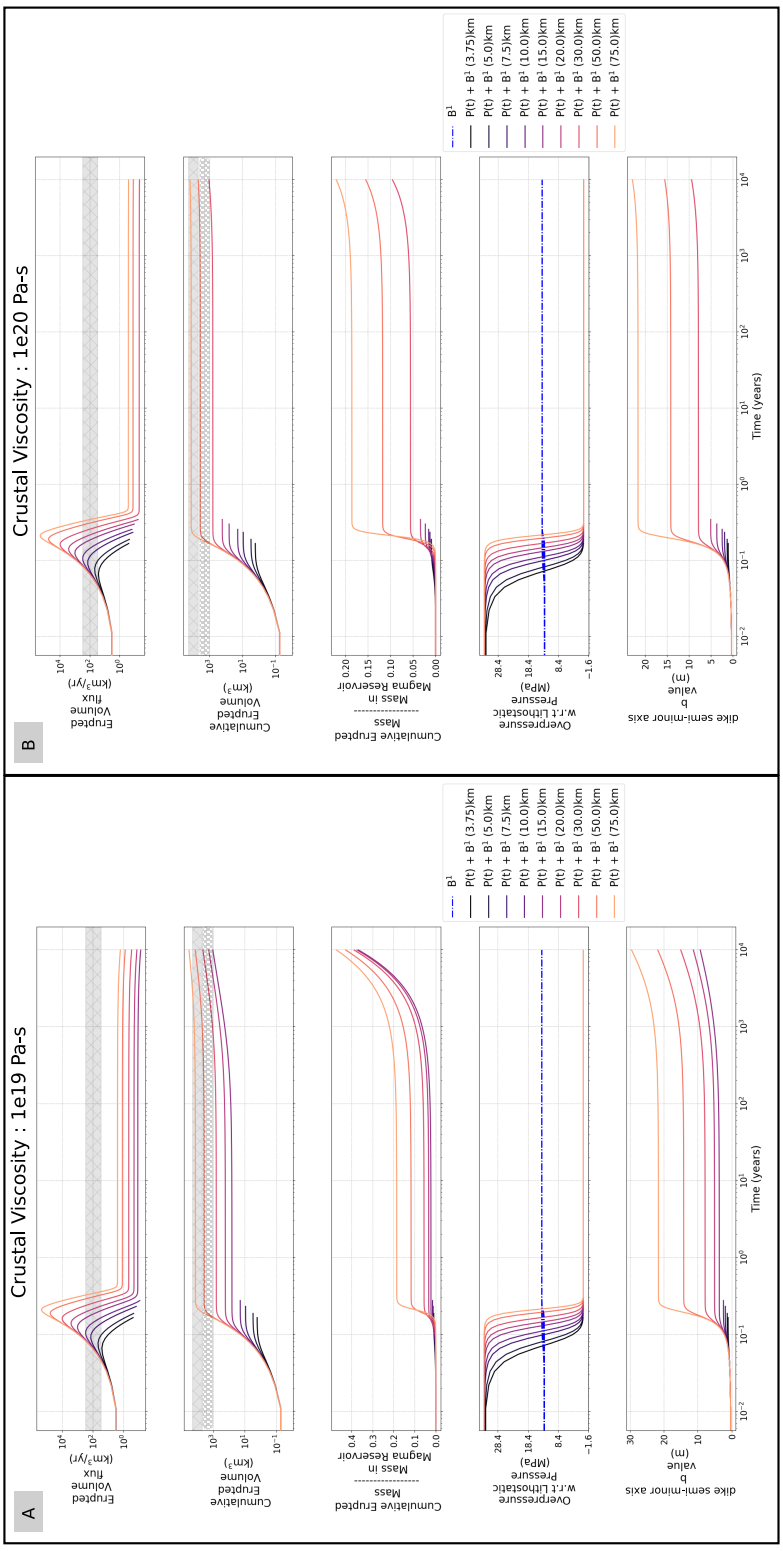
A
Crustal Viscosity : 1e19 Pa-s
B
Crustal Viscosity : 1e20 Pa-s
Erupted Volume flux (km³/yr)
Cumulative Erupted Volume (km³)
Cumulative Erupted Mass
Mass in Magma Reservoir
Overpressure w.r.t. Lithostatic Pressure (MPa)
dike semi-minor axis b value (m)
Time (years)
B¹
P(t) + B¹ (3.75)km
P(t) + B¹ (5.0)km
P(t) + B¹ (7.5)km
P(t) + B¹ (10.0)km
P(t) + B¹ (15.0)km
P(t) + B¹ (20.0)km
P(t) + B¹ (30.0)km
P(t) + B¹ (50.0)km
P(t) + B¹ (75.0)km

Figure 7

Figure 7 *(previous page)*: Model Results for Ellipsoidal Reservoir Model : Erupted volume flux (km^3/yr), total erupted volume (km^3), fraction of magma chamber mass erupted, and magma reservoir overpressure (Pa), and dike width (b). The results are shown for different reservoir semi-major axis sizes (See legend in the figure) and semi-minor axis set to 3 km. In this calculation, we include far-field crustal stress relaxation with the viscosity set to either 10^{19} Pa-s (Panel A) or 10^{20} Pa-s (Panel B) and with no viscous shell relaxation. The depth of all the reservoirs is set to 5 km. A range of eruptive volume fluxes (30-300 km^3/year) and total erupted volumes (1,000 - 5,000 km^3 : hashed region & 5,000 - 10,000 km^3 : shaded hashed region) for flood basalts based on observational constraints is shown on the figure. The B^1 curve shows the magma buoyancy overpressure in the conduit. At the termination of the eruption, the total overpressure is zero : $P(t) + B^1 \sim 0$.

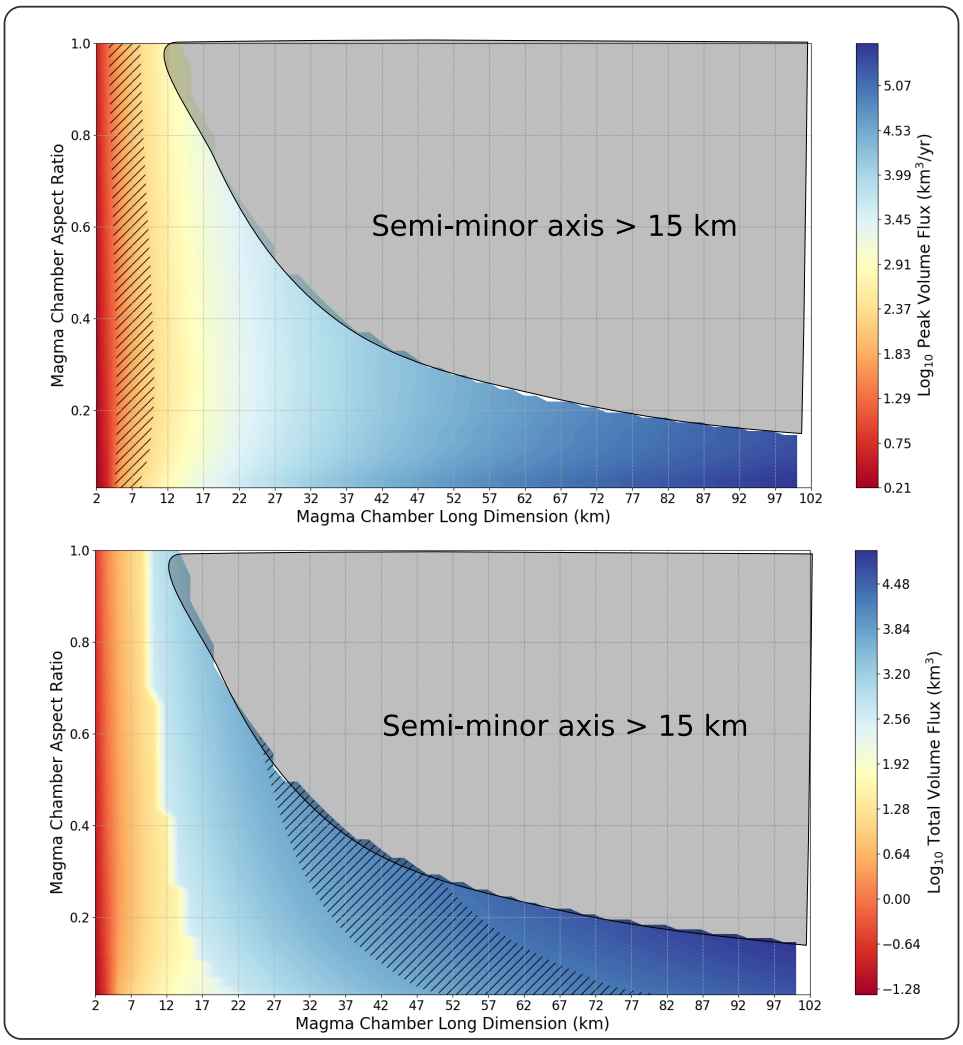

Figure 8: Parameter Space plot for Ellipsoidal Reservoir Model with crustal viscous relaxation (viscosity set to $\mathbf{10^{19}}$ **Pa-s**). A range of eruptive volume fluxes (30-300 km^3/year, Top Panel) and total erupted volumes (5,000 - 10,000 km^3, Bottom Panel) for flood basalts is shaded on the plots. These results clearly illustrate that there is no magma reservoir geometry that can simultaneously satisfy both the constraints.

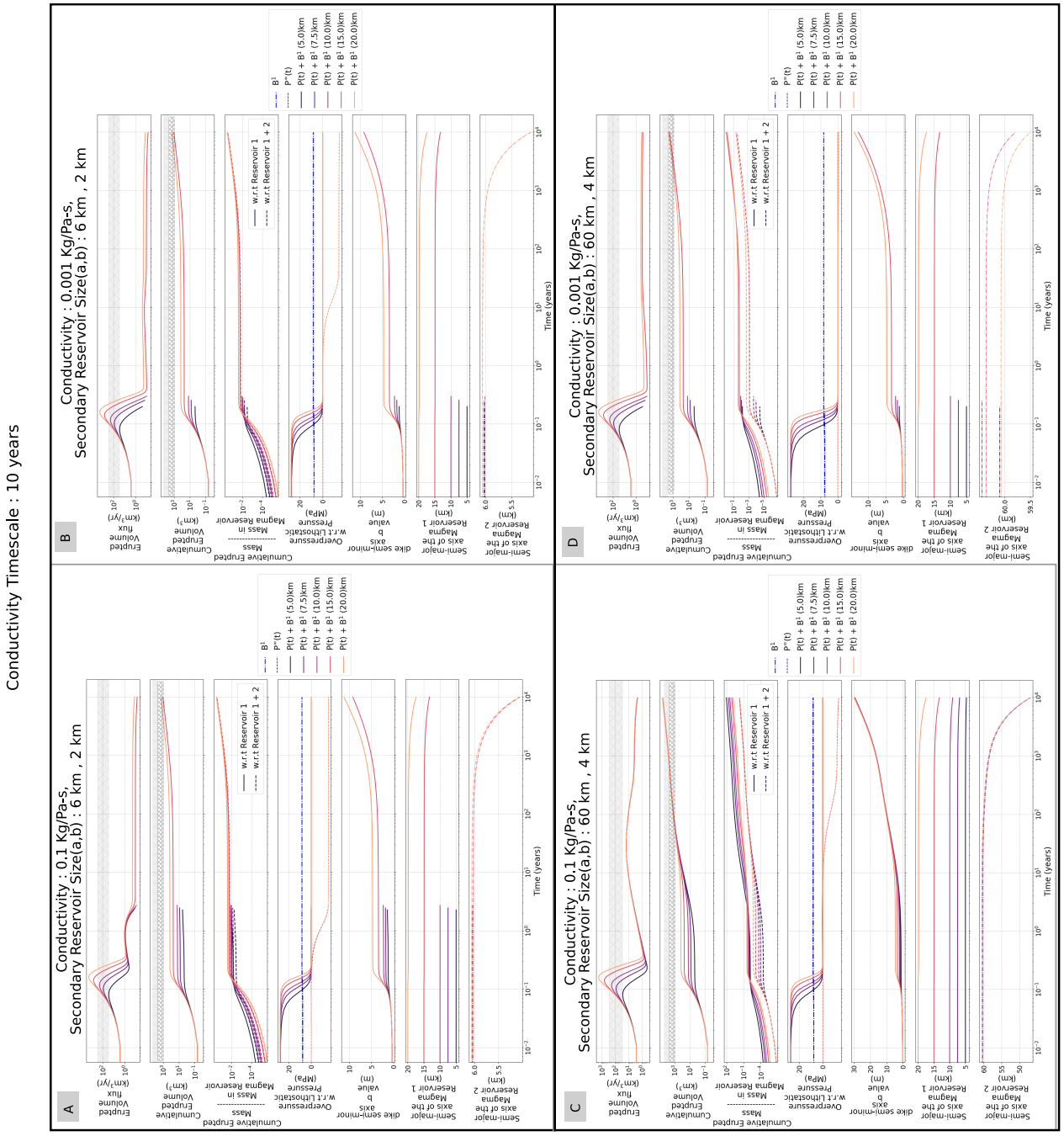
Conductivity Timescale : 10 years
A
Conductivity : 0,1 Kg/Pa-s,
Secondary Reservoir Size(a,b) : 6 km , 2 km
B
Conductivity : 0,001 Kg/Pa-s,
Secondary Reservoir Size(a,b) : 6 km , 2 km
C
Conductivity : 0,1 Kg/Pa-s,
Secondary Reservoir Size(a,b) : 60 km , 4 km
D
Conductivity : 0,001 Kg/Pa-s,
Secondary Reservoir Size(a,b) : 60 km , 4 km
Erupted Volume flux (km³/yr)
Cumulative Erupted Volume (km³)
Cumulative Erupted Mass
Mass in Magma Reservoir
w.r.t Reservoir 1
w.r.t Reservoir 1 + 2
Overpressure w.r.t Lithostatic Pressure (MPa)
dike semi-minor axis b value (m)
Semi-major axis of the Magma Reservoir 1 (km)
Semi-major axis of the Magma Reservoir 2 (km)
Time (years)
B¹
P*(t)
P(t) + B¹ (5.0)km
P(t) + B¹ (7.5)km
P(t) + B¹ (10.0)km
P(t) + B¹ (15.0)km
P(t) + B¹ (20.0)km

Figure 9

Figure 9 *(previous page)*: Model Results for the two Ellipsoidal Reservoir Model with different primary reservoir semi-major axis sizes (See legend in the figure) and semi-minor axis set to 3 km. In this calculation, we include far-field crustal stress relaxation with the viscosity set to 10^{21} Pa-s for the primary magma reservoir and 10^{20} Pa-s for the secondary (deeper) magma reservoir. The viscosity of the viscous shell surrounding both the magma reservoir is set to 5 x 10^{18} Pa-s. The depth of primary reservoirs is set to 5 km while the secondary reservoir is at 11 km depth. The conductivity value and secondary reservoir sizes are fixed to 0.1 kg/Pa-s and 60 km, 4 km respectively. The conductivity time-scale for the calculations varies from 0.5 years (Panel A), 10 years (Panel B), and 100 years (Panel C). A range of eruptive volume fluxes and total erupted volumes for flood basalts based on observational constraints is shaded on the plots.

In order to further increase the erupted mass and decrease the eruption duration, we enable melt influx into the primary magma reservoir from an additional large reservoir ($a_{c,2}, b_{c,2}$: 60 km, 4 km) located at 11 km (3 km plus 2 x semi-major axis of the primary reservoir). In Figure 9, we show the results of models calculations for a range of primary reservoir sizes (a_c between 5 - 20 km) and conductivity timescales ranging from 0.5 to 100 years (t_{cond}, 15). For all the model results, the amplitude of the conductivity (Ω_0), once it is active, is 0.1 kg/Pa-s. In these calculations, we include far-field crustal stress relaxation in a cold crust with the viscosity set to 10^{21} Pa-s for the primary magma reservoir and 10^{20} Pa-s for the secondary (deeper) magma reservoir. The viscosity of the viscous shell surrounding both the magma reservoirs is set to 5 x 10^{18} Pa-s (Degruyter & Huber, 2014).

Analogous to the results from the Spherical Reservoir Model (Figure 4B), we find that a variety of magma reservoir sizes can match both the erupted volume flux and total erupted volume constraints with small t_{cond} (Figure 9A) even though the far-field crust is relatively high viscosity. However, in contrast to results in Figure 4B, the secondary reservoir magma pressure decreases due to mass outflux, and the secondary reservoir becomes under-pressurized over time. This, in turn, reduces the rate in mass flux into the primary reservoir and, consequently, the rate of surface eruptions. In these scenarios, most of the erupted mass is sourced from the deeper magma reservoir directly as illustrated by a 10 km decrease in the semi-major axis of the secondary reservoir. The combination of a large initial reservoir size, as well as lower crustal viscosity, naturally leads to a long-lived eruption. The shape of the primary reservoir geometry only determines the initial eruption rates and the subsequent system behavior is entirely determined by the secondary reservoir dynamics (e.g., Figure 9A, same eruption rates and dike widths at > 10 years) as long as the conductivity timescale is short ($t_{cond} \sim 0.5 - 10$ years). The only exception to this is if t_{cond} is large (e.g., 100 years). In this case, the eruptions from the small reservoir stop before the mass influx can begin (Figure 9C). In reality, this influx may re-pressurize the primary reservoir sufficiently to lead to tensile failure for the small reservoirs.

Although, these results illustrate one potential magma architecture that can produce appropriate eruptive parameters, the choice of an extensive deep magma reservoir is potentially problematic. In particular, it is unclear if the deep magma system is directly activated in each flood basalt eruption given the geochemical evidence for significant shallow fractionation, especially for the Wai subgroup flow (e.g., plagioclase as the dominant phenocryst, See Section 3.1 Paper I). A large upper crustal magma reservoir is ruled out by geophysical observations (Section 6, Paper I). Additionally, if every eruptive episode involves the same large secondary reservoir, it is challenging to explain the geochemical and isotopic changes between successive eruptive events

(Section 3.6). Finally, the challenges with building enough overpressure within large magma reservoirs (Section 2.2.3, Paper I) make it difficult to argue for the rapid establishment of a high conductivity between the primary and a large secondary reservoir for each eruptive episode. In addition, we find in our model, eruptions from a large secondary reservoir continue for 10,000 years (and potentially even longer). Given the estimates of the typical time between individual eruptive episodes (Section 3.3, 3.4, 3.5 Paper I), this duration is too long.

Thus, we explore a large parameter space with different conductivity amplitudes (Ω_0) and secondary reservoir sizes. We show the results for a few representative calculations in Figure 10 with a smaller reservoir size ($a_{c,2}, b_{c,2}$: 6 km, 2 km) and lower conductivity ($\Omega_0 = 0.001$ Kg/Pa-s). Except for the parameters from Figure 9B, none of the other parameter choices can match the eruption rate and erupted volume constraints. For a small reservoir with high conductivity, the faster under-pressurization of the secondary magma reservoir reduces the total erupted volume (Figure 10A vs. Figure 10C). Similarly, a lower conductivity for the large secondary reservoir leads to a much slower eruption rate (Figure 10C vs. Figure 10D, Figure 10A vs. Figure 10B). We find the same qualitative conclusions irrespective of the reservoir depth and volatile content. The higher buoyancy of a more volatile-rich magma mixture leads to slightly higher ($10 - 15\%$) erupted volumes due to higher compressibility as well as the higher underpressure of the primary magma reservoir due to buoyancy. Nevertheless, these processes do not increase the erupted volume for the small secondary reservoir enough to reproduce the observed CFB values. We note that decreasing the far field crustal viscosity does not qualitatively change the results since the viscous stress relaxation is primarily controlled by the low-viscosity visco-elastic shell surrounding the magma reservoir.

It is also noteworthy that even with a small magma reservoir, the eruptive duration in our model is too long to match observations. This is a direct consequence of two physical processes in our model. Firstly, the increase in dike width reduces the magma flux required to reach a unit Peclet number. Thus, even eruptions rates lower than a km^3/year do not terminate the eruption (Figure 10A). Secondly, the viscous stress relaxation in the visco-elastic shell and associated magma re-pressurization provides the small pressure gradient to keep low volume eruptions ongoing, potentially until the magma reservoir is almost fully erupted. This behavior is analogous to the volatile driven siphoning proposed for flood basalt eruptions (Karlstrom & Manga, 2009).

We posit that part of this model behavior may not be physical due to missing physics in our model. Following Piombo et al. (2016), the dike width in our model only evolves due to mechanical erosion or plastic deformation. We have not included any elastic response of the dike-shaped conduit or large scale conduit failure, both of which are potentially key processes for restricting eruption duration. Specifically, the low overpressure within the hydrofracture during the later stages of the eruption may elastically reduce the conduit aperture and shut-off the eruption by faster solidification (Pollard & Segall, 1987; Gudmundsson, 2002). A. Aravena, Cioni, de' Michieli Vitturi, et al. (2018) included an elastic deformation component in their model following Costa et al. (2007) and found that its net impact on the conduit width is small for typical values of erosion rate (A. Aravena, Cioni, de' Michieli Vitturi, et al., 2018, , See Figure S6). However, the efficiency of this process can be enhanced by reducing the host rock rigidity during an eruption as the country rock heats up and plastically deforms. Since the magma overpressure is negative towards the end of the later stages of eruption, the conduit walls may collapse/elastically close and consequently increase the melt flux required for the critical Peclet number = 2. In the following, we include a first order representation of this behavior by including an addition term to the dike semi-minor axis (b) evolution equation (see Eqns. 27). Following Costa et al. (2007); A. Aravena, Cioni, de' Michieli Vitturi, et al. (2018), we calculate the influence of

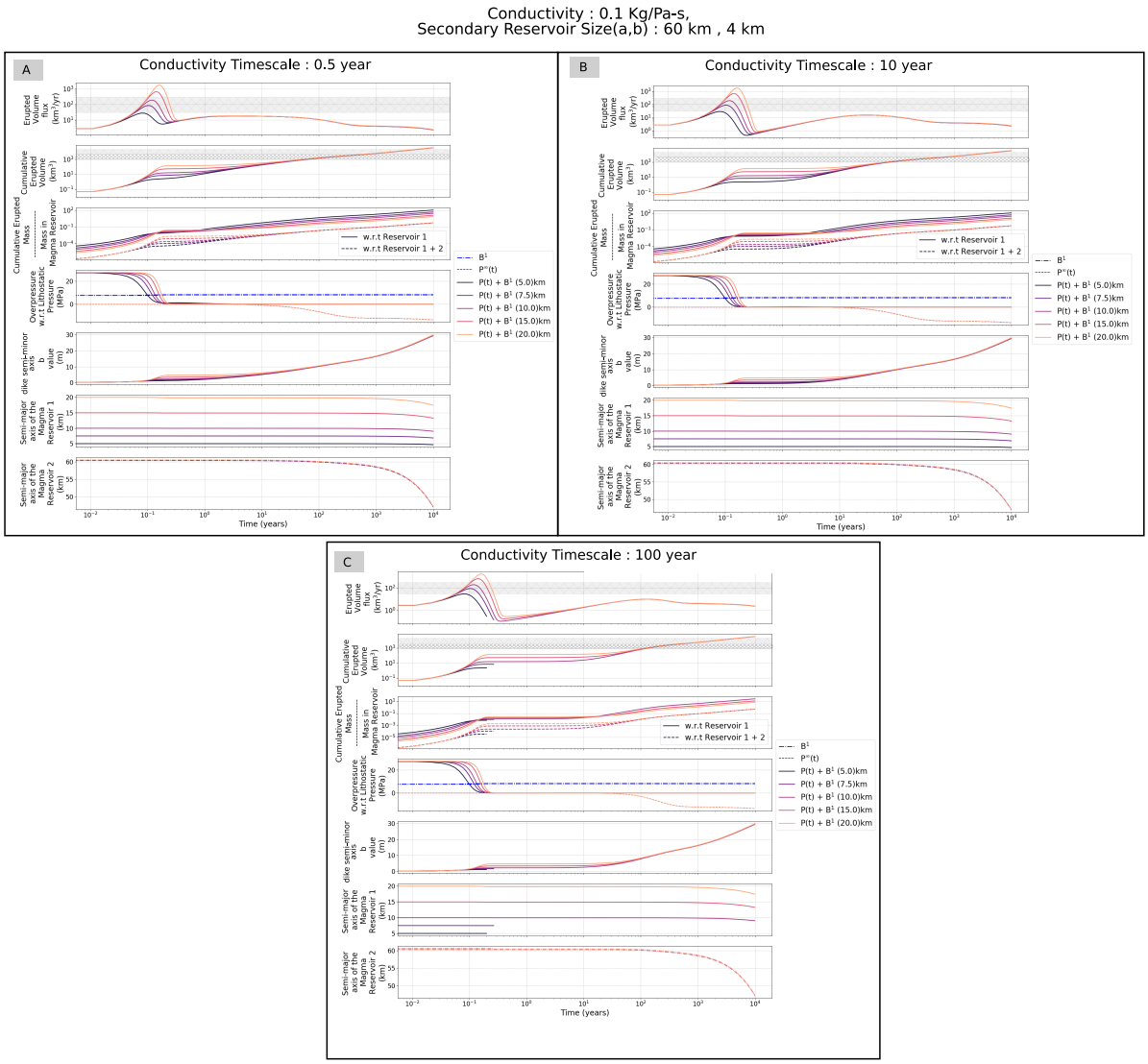

Figure 10: Model Results for two Ellipsoidal Reservoir Model for different primary reservoir semi-major axis sizes (See legend in the figure) and semi-minor axis set to 3 km. In this calculation, we include far-field crustal stress relaxation with the viscosity set to 10^{21} Pa-s for the primary magma reservoir and 10^{20} Pa-s for the secondary (deeper) magma reservoir. The viscosity of the viscous shell surrounding both the magma reservoirs is set to 5 x 10^{18} Pa-s. The depth of primary reservoirs is set to 5 km while the secondary reservoir is at 11 km depth.. The conductivity time-scale for all the calculations is fixed to 10 years with two different conductivity values (Panels A & B; Panels C & D), and two different secondary reservoir sizes (Panels A & C; Panels B & D). A range of eruptive volume fluxes and total erupted volumes for flood basalts based on observational constraints is shaded on the plots.

elastic deformation on b as :

$$b_{steady}(t) = b(t) + P(t)(f_2(t)a + f_1(t)b) \tag{102}$$
$$f_1(t) = (2 * \nu_r - 1)/(2\mu_r(t)) \tag{103}$$
$$f_2(t) = (1 - \nu_r)/(\mu_r(t)) \tag{104}$$
$$\mu_r(t) = [10exp^{-t/t_{cool,b}} + 0.5\,]\text{GPa} \tag{105}$$

Here ν_r (= 0.3) and $\mu_r(t)$ (in GPa) are the Poisson ratio and the rigidity of the host rock respectively. We allow evolution of μ_r over a cooling timescale $\sim 5(b^2/\kappa_{thermal})$ to model the thermal weakening of the conduit with continued magma flux. Thus, the ability of a conduit to remain stable during under-pressurization will progressively decrease (see more discussion in Á. Aravena et al., 2018, and references therein). Using the difference between the present conduit shape (b) and the steady state elastic shape b_{steady}, we write a relaxation term $b_{elast,relx}$:

$$b_{elast,relx} = (b_{new} - b)/t_{relax,elast} \tag{106}$$

We set $t_{relax,elast} \sim 10$ years (decreasing to 1 year if $b_{elast,relx}$ is negative). We acknowledge that this parameter is extremely uncertain and can potentially be much smaller than a year (e.g., kilauea eruption C. A. Neal et al., 2019) or very long considering the crustal Maxwell time-scale. Here, we chose an intermediate value assuming a low crustal rigidity and low crustal viscosity near the conduit.

In our model, the net evolution of the dike semi-minor axis (b) is :

$$\frac{db}{dt} = \frac{k}{d_{res}}\Big[P(t) + (\rho_c - \rho_{res})gd_{res}\Big]b + b_{elast,relx} \tag{107}$$

We acknowledge that our model is highly idealized and introduces additional not well constrained model parameters. In the following, we have typically chosen model parameters that prevent continued eruptions with eruption rates less than ~ 0.5 km^3/year in order to be consistent with the lower end of estimates from Section 3.5 (Paper I) (also see A. Aravena, Cioni, de' Michieli Vitturi, et al., 2018). To first order, the additional dike semi-major axis evolution model helps terminate eruptions much earlier for the small magma reservoirs.

3.2.3 Multiple Secondary Reservoirs

Given the challenges with a single reservoir model, we next consider a model scenario where the primary reservoir is connected to multiple secondary reservoirs. This model setup approximates the idea of a magmatic architecture composed of a set of magma reservoirs interconnected through multiple magma transport pathways analogous to what has been proposed for modern-day arc and hotspot volcanism (e.g., Marsh, 2013; Cashman et al., 2017; Aki & Ferrazzini, 2001, see Figure 22B for a cartoon illustration). A particularly relevant example is the Icelandic Eyjafjallajokull 2010 eruption where there is seismic and petrological evidence of stress interaction between sill-shaped magma lenses over weeks and consequent failure to feed the eruptive conduit (Tarasewicz et al., 2012; White et al., 2019).

To illustrate the model behavior with this configuration, we show a set of representative calculations in Figure 11. For these calculations, the primary reservoir (a_c, b_c: 7.5km, 2 km; 5 km depth) is connected to five additional secondary reservoirs with semi-major axes between 15-25 km and a 3 km semi-minor axis (depth of 11 km). The crustal viscosity is 10^{21} Pa-s for the primary reservoir and 10^{20} Pa-s for the secondary reservoirs. We initialize the system with an overpressure of 20 MPa in the primary reservoir and between 5-20 MPa for the secondary reservoirs (to represent various stages of magmatic evolution). The viscosity of the viscous shell surrounding

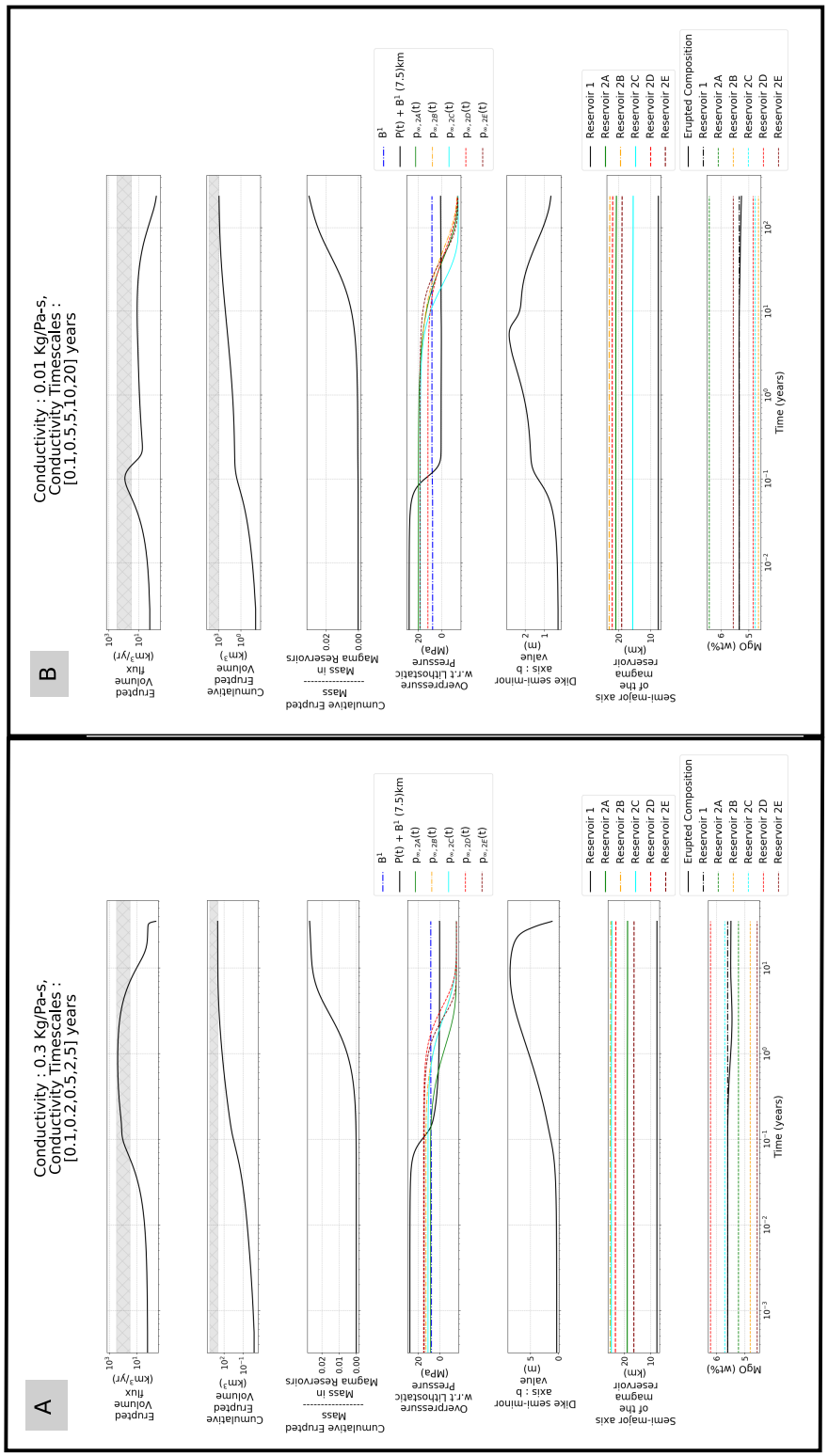
A
Conductivity : 0.3 Kg/Pa-s,
Conductivity Timescales :
[0.1,0.2,0.5,2.5] years
Erupted Volume flux (km³/yr)
Cumulative Erupted Volume (km³)
Cumulative Erupted Mass

Mass in Magma Reservoirs
Overpressure w.r.t Lithostatic Pressure (MPa)
Dike semi-minor axis : b value (m)
Semi-major axis of the magma reservoir (km)
MgO (wt%)
Time (years)
B
Conductivity : 0.01 Kg/Pa-s,
Conductivity Timescales :
[0.1,0.5,5,10,20] years
Erupted Volume flux (km³/yr)
Cumulative Erupted Volume (km³)
Cumulative Erupted Mass

Mass in Magma Reservoirs
Overpressure w.r.t Lithostatic Pressure (MPa)
Dike semi-minor axis : b value (m)
Semi-major axis of the magma reservoir (km)
MgO (wt%)
Time (years)
B¹
P(t) + B¹ (7.5)km
Reservoir 1
Reservoir 2A
Reservoir 2B
Reservoir 2C
Reservoir 2D
Reservoir 2E
Erupted Composition

Figure 11

Figure 11 *(previous page)*: Model Results for multiple Ellipsoidal Reservoir Model : Erupted volume flux (km^3/yr), total erupted volume (km^3), fraction of magma chamber mass erupted, and magma reservoir overpressure (Pa), and dike width (b), and MgO wt %. The primary reservoir has a semi-major axis 7.5 km, semi-minor axis 2 km at 5 km depth connected to 5 secondary reservoirs with different conductivity values and conductivity timescales (See in Figure title). The initial size of each of the secondary reservoir is 15-25 km (semi-major axis), 3 km (semi-minor axis), 11 km depth with the crustal viscosity of 10^{21} Pa-s for the primary reservoir and 10^{20} Pa-s for the secondary reservoirs. The viscosity of the viscous shell surrounding both the magma reservoirs is set to 1 x 10^{19} Pa-s (Panel A), and 2 x 10^{19} Pa-s (Panel B). A range of eruptive volume fluxes and total erupted volumes for flood basalts based on observational constraints is shaded on the plots. Panel A represents the higher inter-reservoir conductivity scenario while the Panel B shows the impact of longer conductive times and lower conductive amplitude.

each of the magma reservoirs is set to 1 x 10^{19} Pa-s (Figure 11A) or 2 x 10^{19} Pa-s (Figure 11B). We also calculate the erupted magma composition based on a simple mixing model for the primary magma reservoir (Eqn. 91). The initial compositions of all the reservoirs are chosen at random between 4 to 6 wt % MgO (a range typical of Wai subgroup flows, Beane et al., 1986).

In Figure 11, we show the results for two representative calculations with different conductivity timescales (t_{cond}) and amplitude (Ω_0). In Figure 11A, we use a high $\Omega_0 = 0.3$ Kg/Pa-s and a range of conductivity timescales ($t_{cond} = 0.1$, 0.2, 0.5, 2, and 5 years). This model case represents a more mature magmatic system with high interconnectivity. For Figure 11B, we choose a lower conductivity ($\Omega_0 = 0.01$ Kg/Pa-s) as well as longer conductivity timescales ($t_{cond} = 0.1$, 0.5, 5, 10, and 20 years). Not surprisingly, we can better match the eruptive flux and volume constraints, especially for the parameters in Figure 11A. With a less mature magmatic system (e.g., Figure 11B), the time-averaged eruptive flux is lower and a longer eruption duration is required to reach the appropriate erupted volumes. Also, the range of conductivity timescales naturally introduces variable surface eruption rates, which have been hypothesized to be a requirement for the formation of inflated sheet lobes (e.g., Rader et al., 2017). The bottom panels of Figure 11A and 11B show the erupted composition will have some intra-flow variation due to the different compositions of secondary reservoirs and varying levels of mixing. Finally, a final dike width of $\sim$ 10 m is very consistent with the range of feeder dike widths in Deccan Traps, especially the active portions of a multiple dike (Section 5, Paper I).

We want to emphasize that our parameter choices are not unique and it is possible to obtain the same time-averaged eruptive flux and total volume with different parameters. Additionally, it is not difficult to sustain higher eruptive fluxes and/or longer eruptions by changing the conductivity timescales, conductivity amplitude, as well as the number of secondary reservoirs. At present, it is difficult to infer how the eruptive style and rates evolved during a CFB eruptive episode based on the lava flow morphology or geochemical variations due to lack of systematic observations (See Section 3.5 and 3.6). Thus, we are not trying to match a specific eruptive history with these calculations. Instead, these results show that the properties of a CFB eruptive episode can be explained by a multiply connected magmatic system.

Conceptually, the multiply-connected magma chambers are a necessary component of CFB magma architectures because this is the only way to have long (tens-hundreds of year) and large (many thousands of km^3) eruptive episodes. If there is

only a single magma reservoir feeding an eruption, the magma overpressure remains large due to reservoir compressibility until a few percent of magma reservoir volume is erupted. Consequently, the overall eruptions rate are too large and the total eruption durations too small compared to observations (Paper I). This physical constraint is circumvented by having multiply-connected small magma reservoirs as shown in the 11. The primary reseroir feeding the surface eruption undergo the same physical process, initially high eruption rate followed by a gradual decline, quicker than a large reserovoir. But, with secondary reservoirs getting connected to the primary reservoir, the eruption can be sustained at required eruption rates since the primary reservoir maintains an overpressure due to melt influx. This physical mechanism is the underlying reason for our conclusions.

3.3 Timescale analysis

We can summarize the key features of the Magma Reservoir Models using a few key characteristic timescales for the primary magma reservoir : timescale for repressurization by recharge ($t_{repress}$), crustal and visco-elastic shell relaxation (t_{relax}), establishment of significant conductivity between reservoirs (t_{cond}), and the timescale for overpressure relaxation by eruptions (t_{flux}, Eqns. 19, 25-27, Table 1). We define t_{relax} as the minimum of $t_{Maxwell}$ and $t_{R,relax\,compress}$ since both of them represent viscous stress relaxation in the surrounding crust. Using t_{flux} to non-dimensionalize the timescales, we get :

$$\Theta_1 = t_{flux}(t=0)/t_{relax} \tag{108}$$

$$\Theta_2 = t_{flux}(t=0)/t_{cond} \tag{109}$$

$$\Theta_3 = t_{repress}/t_{flux}(t=0) \tag{110}$$

We show a regime diagram with these non-dimensional numbers in Figure 12. With two or more magma reservoirs, the full system behavior is controlled by an analogous set of non-dimensional numbers for the secondary reservoir. These additional numbers are necessary to fully describe the model results, especially the absolute values of the erupted volume and eruption rates. Additionally, the conduit width can significantly change (by a factor of 100 in some of the calculations) leading to a significant time-evolution of the t_{flux}. A full analysis of this system is beyond the scope of this study. We do, however, find that Θ_1, Θ_2, and Θ_3 provide a "qualitative" description of the model behavior.

We first consider the case of high reservoir conductivity such that $t_{repress}$ and t_{flux} are comparable or t_{flux} is smaller (i.e. $\Theta_3 < 10$, Figure 12A). If both the timescales for magma recharge and crustal viscous stress relaxation are significantly longer than the t_{flux} ($\Theta_1 << 1$, $\Theta_2 << 1$), then the erupted mass is sourced only from the primary magma reservoir with a high initial eruption rate and short eruptions (elastic limit, Figure 5). As the viscosity of the visco-elastic shell decreases, the rapid relaxation of magma underpressure allows a continuous eruption at a low eruption rate (Figure 7). Consequently, the time-averaged eruption rate (over the eruption duration) for the system decreases. Since the magma eruption is long-lived, the recharge can contribute to the erupted mass even for $\Theta_2 < 1$ (e.g., Figure 9C). This further increases the total erupted volume.

At the other end-member, if the crust is elastic ($\Theta_1 << 1$) but the timescale for recharge is large, i.e., $\Theta_2 > 1$, the recharge from the secondary reservoir will ensure a high continuous eruption rate. Since the crustal response (for both magma reservoirs) is primarily elastic, the eruptions will stop when both the magma reservoirs are underpressurized. If instead, the crust has a lower viscosity (larger Θ_1), eruptions will be long-lived but with lower eruption rates. Thus maximum erupted mass in the system is in the top right parameter space ($\Theta_2 > 1$, $\Theta_2 > 1$). The maximum time-

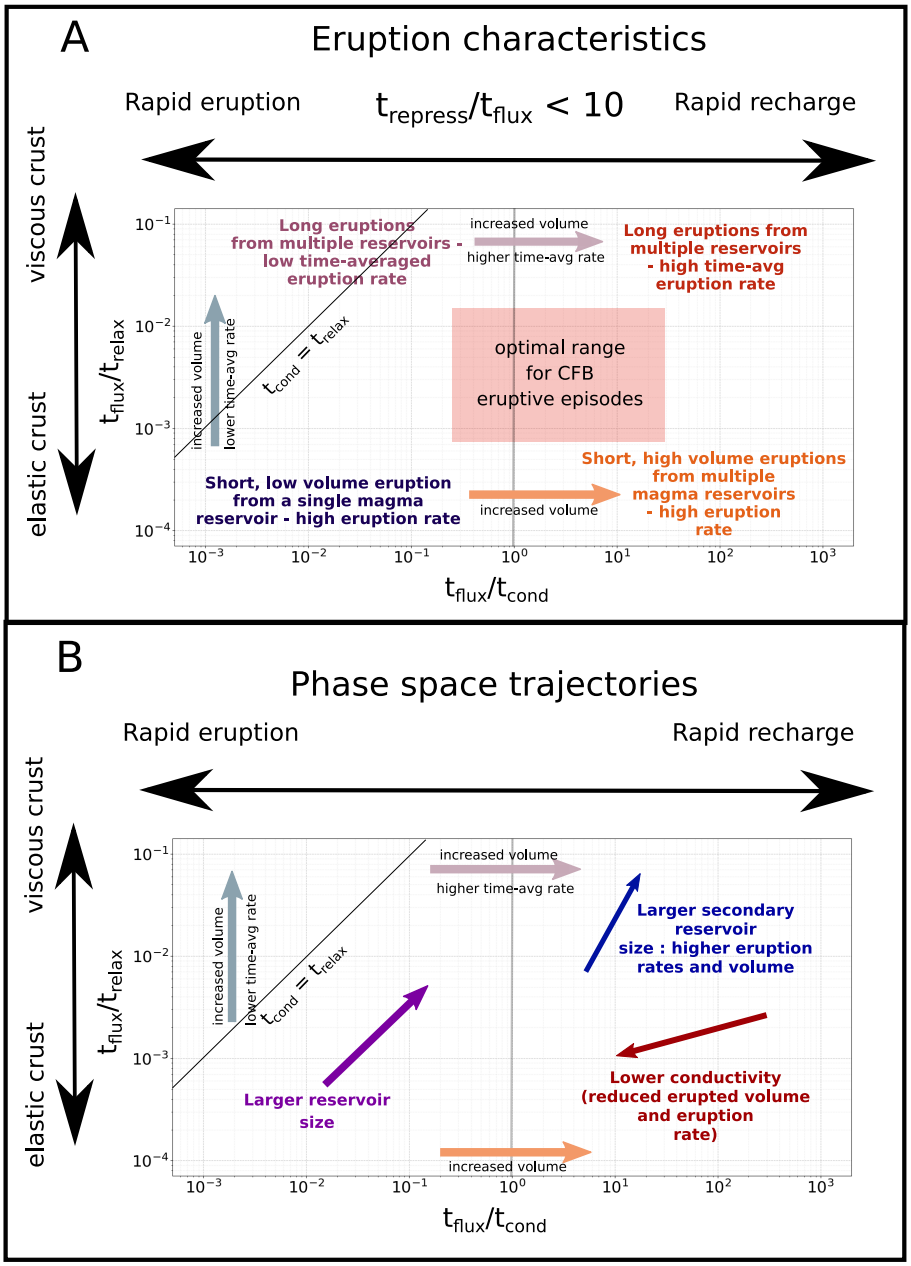

Figure 12: Regime diagram for the two Ellipsoidal Reservoir Model. Using results from Section 3.2, the changes in eruption fluxes and duration are illustrated on the regime diagram (Panel A). In Panel B, we show how changes in physical properties of the reservoirs as well as other characteristic timescale translate to movement in this regime space. We also highlight a potential region for optimal continental flood basalt eruptions in Panel A.

averaged eruption rates are for the lower right part of parameter space ($\Theta_2 > 1$, $\Theta_2 < 1$). A larger primary magma reservoir will increase the t_{flux} for the same dike width, thus moving us towards the top right of the parameter space. Given the model results and the observational constraints, we anticipate that the optimal parameter space for CFB eruptions is in the center-right part of the parameter space (Figure 12A). However, the specific region of parameter space would depend on the parameters of the secondary reservoirs.

If the size of the secondary magma reservoir is increased, the maximum eruption rate, as well as the erupted volume, will increase along with potentially a small increased time-averaged eruption rate (e.g., Figure 10A, 16C). We illustrate this in Figure 12B with the blue arrow direction chosen to represent these characteristics. On the other hand, if the reservoir conductivity decreases, both $t_{repress}$ and Θ_3 will increase. As illustrated by Figure 10C & 16D, this would typically lead to reduced erupted volume as well as eruption rates (red arrow in Figure 12B).

3.3.1 Implications for CFB architecture

In conclusion, our model results clearly illustrate that eruptions from a single large magma reservoir do not match the observational constraints on DT eruption rates and eruption durations. Instead, magma recharge during the eruption from secondary magma reservoirs is a key requirement. We posit that based on a variety of observations, this secondary magma reservoir cannot just be a large lower crustal magma body (See Section 5.2). Instead, our preferred model architecture for CFBs is the presence of several small ($\sim 10^2$ - $10^{3.5}$ km^3) interconnected magma reservoirs present throughout the crust. As illustrated in Figure 11 (with potentially even more coupled reservoirs), such a magmatic architecture can help explain both the properties of individual eruptive episodes as well as the intra-flow geochemical variability (Section 3.7).

4 Model results - Thermal Model

We next assess how crustal thermal evolution affects the ability of different magma bodies to erupt vs. accumulate and grow. We first briefly describe the phase space, how it relates to eruption frequency, and how changing reservoir and crustal properties translate to the phase space. We then present model results for first a constant time-averaged melt flux, followed by a melt flux representative of melt from a mantle plume head.

4.1 Magmatic Timescales

We can define a magma reservoir's eruptive dynamics using a set of four characteristic timescales : $t^c_{viscous}$, t^c_{cool}, t^c_{fill}, and $t^c_{press\,diff}$ (Eqns 92-95, Degruyter & Huber, 2014; Mittal & Richards, 2019). In order to compare these timescales, we define the following non-dimensional Deborah timescales (ratios of two different characteristic times) :

$$De_{visc} = t^c_{viscous}/t^c_{fill} \tag{111}$$
$$De_{cool} = t^c_{cool}/t^c_{fill} \tag{112}$$
$$De_{pd} = t^c_{press\,diff}/t^c_{fill} \tag{113}$$
$$\tag{114}$$

In Figure 13A, we show the 2D regime diagram (assuming $De_{pd} >> 1$). When $De_{viscous} < 1$, the viscous relaxation will prevent a magma reservoir for reaching sufficient overpressure to initiate diking to the surface (Degruyter & Huber, 2014). If

$\tau_{press\ diff}/\tau_{in} >> 1$

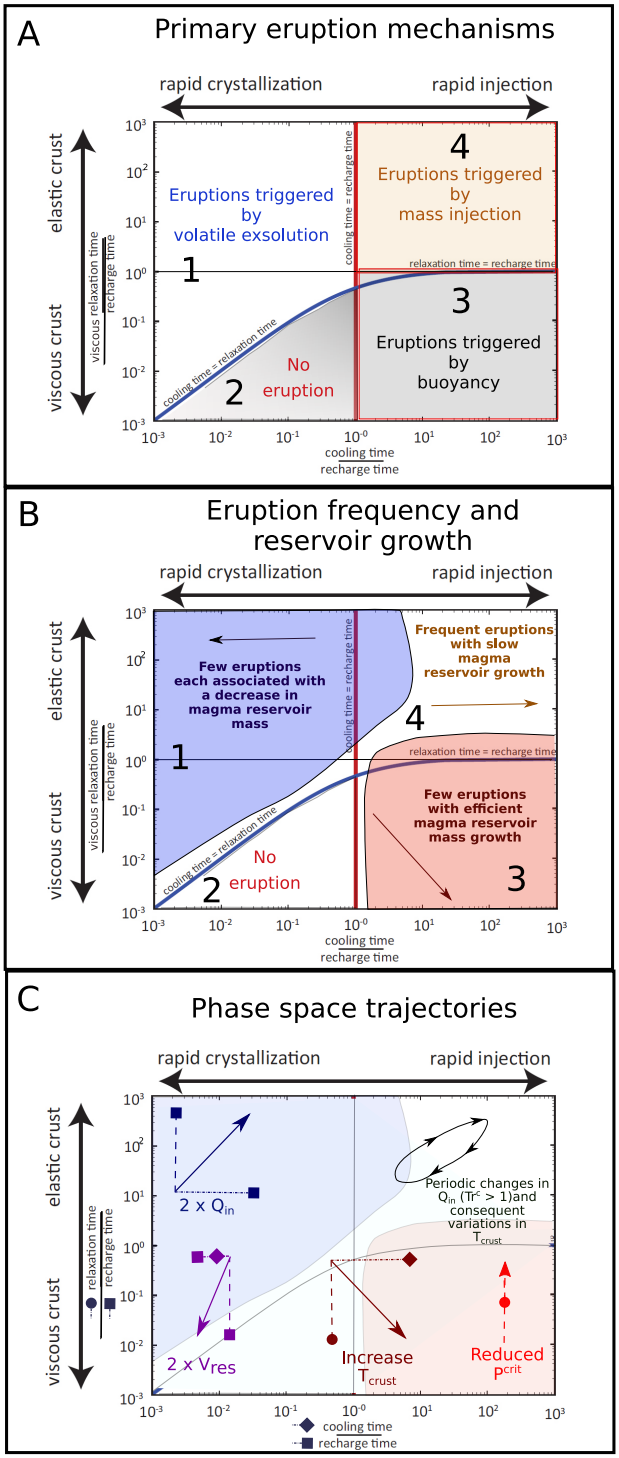

Figure 13

Figure 13 *(previous page)*: Regime diagram for the non-dimensional magmatic timescales (Degruyter & Huber, 2014; Mittal & Richards, 2019) when pressure diffusion is not important. In Panel A, we show how the eruptibility changes as a function of non-dimensional parameters as well as which eruption mechanism dominates. In Panel B, we used results from Townsend et al. (2019) and Black and Manga (2017) to illustrate regions of reservoir growth vs shrinkage and how the eruption frequency changes across the phase space. In Panel C, we illustrate the direction of translation in the phase space based on potential changes in crustal and reservoir properties (Arrow line). The dashed and dotted lines illustrate how different components - filling timescale (square), cooling time (diamond), and viscous timescales (circle) contribute to the net motion in the phase space.

$De_{cool} < 1$ but $De_{visc} > De_{cool}$, eruptions can still occur due to pressurization by secondary volatile exsolution during cooling (Region 1) whereas in the converse, no eruptions occur and the magma will accumulate as intrusions (Region 2). On the other hand, $De_{cool} > 1$ and $De_{viscous} > 1$ allows buildup of magma overpressure by recharge (Region 4). Finally, if $De_{cool} > 1$ and $De_{viscous} < 1$, the magma reservoir will not cool rapidly enough to crystallize but any elastic stress accumulation is relaxed too rapidly (Region 3). Thus, the only viable mechanism to initiate tensile failure is buoyancy overpressure (See Section 2.2, Paper I) or external triggers (de Silva & Gregg, 2014; Gudmundsson, 2016). When $De_{pd} < 1$ (not shown here, see Mittal & Richards, 2019), pressure diffusion of volatiles will reduce the ability of a magma reservoir to pressurize and erupt. We show a couple of other orthogonal projections of the phase space in Figure 14 (bottom right panel). In the limit of $De_{viscous} >> 1$, the phase space behavior is similar with De_{pd} being the stress relaxation mechanism instead of $De_{viscous}$. Finally, when $De_{viscous} > De_{pd}$, pore pressure diffusion is the relevant relaxation mechanism while viscous stress relaxation dominates in the opposite case.

Within this 3D phase space, the eruption frequency and the reservoir growth rate also vary. Based on the results from Townsend et al. (2019) and Black and Manga (2017), we show the various regimes in Figure 13B for a 2-D slice of the full phase space assuming De_{pd} much larger than 1. In Region 1 (along with a small fraction of Region 2), individual eruptions are associated with a net mass loss since volatile exsolution increases the magma compressibility and hence the efficiency of the eruption. Additionally, a single magma reservoir does not erupt very frequently or many times before solidification (Degruyter & Huber, 2014). This result is a direct consequence of the fact that volatile exsolution would generally require a significant amount of cooling per cycle, and this is not very efficient to sustain frequently erupting long-lived magma bodies.

In Region 3, on the other hand, the cooling timescale is much longer than the recharge timescale leading to reservoir growth. Since buoyancy overpressure is the primary mechanism for eruption, individual eruptions, if they occur, are large but very infrequent (Black & Manga, 2017). Finally, in Region 4, recharge is an efficient mechanism for eruptions. Consequently, the magma reservoir can erupt frequently but does not accumulate much mass over multiple eruption cycles. We note these results have been calculated using a much more simplified eruption model than presented in the previous section. Specifically, an eruption in this model stops when the magma pressure reaches lithostatic rather than the magmastatic condition (See discussion in Section 3.1 Degruyter & Huber, 2014; Mittal & Richards, 2019). Additionally, the magma reservoir geometry can also influence the eruption frequency. Nevertheless, we still expect that the overall pattern of eruption frequency and reservoir growth vs.

shrinkage is a robust conclusion given the underlying physical mechanisms described above.

The primary focus of our subsequent analysis is to assess how changes in magma reservoir size, as well as crustal temperature, affect the likelihood of eruptibility. In Figure 13C, we illustrate how these changes translate to the phase space (2D slice with $De_{pd} >> 1$). Firstly, an increase in magma reservoir size leads to a decrease in De_{cool} since $t^c_{cool} \propto R^2$ (diamond in Figure 13C) while $t^c_{fill} \propto R^3$ (square in Figure 13C). Similarly, De_{visc} as well as De_{pd} decrease as well. Thus, in conclusion, an increase in reservoir size is a net left-downward direction (Purple color). Since the buoyancy overpressure is proportional to the reservoir's height, an increase in the size of the magma body would also increase the likelihood of buoyancy-driven eruption.

An increase in crustal temperature decreases the crustal viscosity (and hence t^c_{visc} - circle symbol in Figure 13C) and crustal permeability (De_{pd} increase) while increasing the cooling timescale t^c_{cool}. In aggregate, the hotter crust is characterized by a right-downward arrow in the 2D phase space (Brown color). A reduction in critical overpressure ΔP increases the t^c_{visc} without affecting any of the other timescales. Hence, it is represented by an upward arrow (Red color). Finally, an increase in the recharge rate decreases the t^c_{fill} and is thus represented by the right-upward arrow (Blue color).

Besides the Deborah numbers described above, there is one additional characteristic timescale in our 1D thermal model. Following Karlstrom et al. (2017), we allow variability in the input melt flux with a time period T_{period} (Section 2.2.2). Non-dimensionalizing this with the reservoir recharge timescale, we get another non-dimension number :

$$\mathrm{Tr}^c = T_{period}/t^c_{fill} \tag{115}$$

Here Tr^c is the crustal transport number, which quantifies whether variability in melt supply is significant compared to the mean recharge rate for a given magma reservoir. Typically, an increase in parental melt flux would be associated with crustal temperature increase (since not all the melt may be directly emplaced in the magma body) and vice-versa. Thus, in the phase space (Figure 13C), periodic variations in melt flux can trace a loop oriented along the right-upward arrow direction (Black color, Figure 13C). The larger the Tr^c value, the larger the amplitude of the corresponding loop.

4.2 Constant Melt flux

We first consider a constant time-averaged melt flux of 10^{-6} $(\mathrm{km}^3/\mathrm{year})/\mathrm{km}^2$ at the base of the 30 km crustal section with a dike injection lengthscale (L^{rng}_{dike}) of 15 km (See Section 2.2 and 2.3 for other parameter choices) and $\mathrm{Tr}^{cr} \sim 0.05$ (Figure 14, top panel). Integrated over the mantle plume head with a radius of $\sim$ 500 km (e.g., Farnetani et al., 2018) also approximately equivalent to the circular area of DT), our chosen flux represents a total melt flux of 0.75 km^3/year. Since we do not model explicitly regions of melt accumulation in our model, all input crustal melt is emplaced stochastically as dikes. Consequently, our chosen parameter value is, to first order, reasonable since a substantial fraction of the plume melt will accumulate in magma bodies and feed surface eruptions. The total duration of all our model calculations is 2 Ma.

We show the results for this parameter set in Figure 14. In the top panel, we plot the input melt flux at the base of the crust. The bottom left panel of Figure 14 shows the results of the thermal calculation over time along with the corresponding values of various De numbers for a small magma body (a_c, b_c: 2 km, 600 m) as well as the Buoyancy overpressure w.r.t local lithostatic pressure. We find that with continued melt emplacement into the crust, the lower crustal temperature increases rapidly

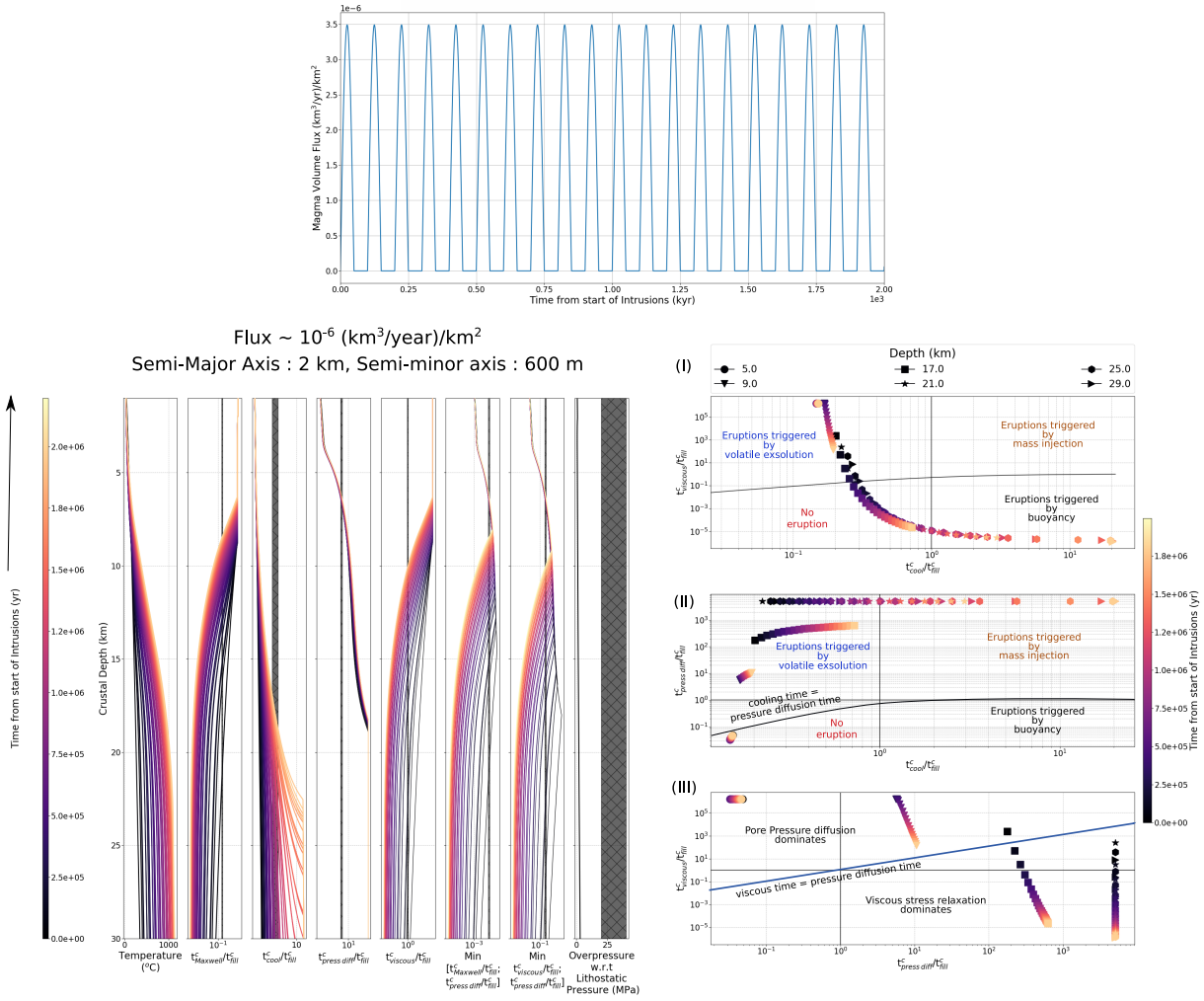

Figure 14: 1D thermal evolution model with constant melt input with a dike length-scale of 15 km (w.r.t the base of the crust). The Figure panel on the top shows the time-history of melt flux into the crustal column, the middle figure shows the thermal evolution of the crustal column as well as various non-dimensional timescales (Degruyter & Huber, 2014; Mittal & Richards, 2019) while the third figure shows the magmatic regime diagram for ascertaining the eruptibility of magma for reservoirs at different depths. The initial concentrations of water and CO_2 in the melt is calculated for 10% degree of partial melting with a mantle source composition of 750 ppm CO_2 and 0.23 wt % H_2O.

while the upper crust remains cold due to hydrothermal circulation and L_{dike}^{rng} of 15 km. Because of the increase in temperature and a corresponding decrease in crustal viscosity, both the Maxwell and the viscous relaxation times decrease. There is also a corresponding increase in the cooling timescale due to higher background temperature. Finally, the crustal permeability at great depths is too low to significantly affect pore pressure diffusion. Coupled with the low volume fraction of magmatic volatile phase at depth, De_{pd} is very large in the lower crust but is much less than 1 in the top $\sim$ 5 km of the crust. Since the magma reservoir is only 600 m depth, the buoyancy overpressure is negligible for all depths.

The bottom right panel of Figure 14 shows three projections of the De number phase space (described in the previous section). In this phase space, we show the temporal De number trajectories for magma bodies emplaced at a few different depths. The De_{pd} vs. De_{visc} phase space (Panel III) shows that the dominant stress relaxation process at shallow depths (5 km and 9 km depths) is pore pressure diffusion. In contrast, viscous stress relaxation is more important for deeper magma bodies. Thus, the appropriate 2D phase space for the shallow bodies is De_{pd} vs. De_{cool} (Panel II) while De_{visc} vs. De_{cool} (Panel I) is the relevant phase for the deeper magma reservoirs.

Due to the high crustal permeability, the 5 km depth magma body is likely to never erupt. In contrast, the same sized magma body at the 9 km depth can erupt due to volatile exsolution throughout the 2 Ma time interval (if the melt has sufficient volatiles). We find that although even deeper magma bodies can initially erupt via volatile exsolution, the temperature increase eventually shuts off eruptions with buoyancy overpressure being the only viable eruption mechanism. In Figures 15, 16, 17, we show the results for the same thermal model for three different magma reservoir sizes (a^c, b^c): 2km, 600m; 5 km, 1.5 km; and 20 km, 5 km. The pattern for all three magma bodies in their respective panel I are essentially the same except that the trajectories are translated to the left for larger magma bodies. This result is consistent with the conclusions from the previous section (and illustrated by the purple arrow in Figure 13C). It is interesting to note that the larger magma bodies are typically in the no-eruption phase space as opposed to the smaller bodies which transit that phase space quickly with changing temperatures (See Figure 15 vs. Figure 17).

Next, we show the results with a more volatile-rich mantle composition: 1500 ppm CO_2 and 0.46 wt % H_2O (See discussion in Section 2.3.2) in Figure 18B. The main consequence of this change vis-a-vis the standard case (Figure 15) is the deeper volatile exsolution of CO_2 and smaller pressure diffusion timescale. As a result, the primary stress relaxation mechanism for some of the mid-crustal magma bodies (17, 21 km depths) is initially not viscous relaxation. Thus, with higher initial volatile content, the relevance of pore pressure diffusion increases to greater crustal depths.

Finally, in Figure 18A, we show the model results for a 10x higher input melt flux: 10^{-5} $(\mathrm{km}^3/\mathrm{year})/\mathrm{km}^2$. Unsurprisingly, the crustal temperature increases much more rapidly with the larger melt flux. The larger melt flux (and the consequent decrease in recharge timescale) translates the trajectories towards the upper right part of the phase space in Figure 18A, Panel I (also see blue arrow in Figure 13C). Consequently, some of the upper to mid-crustal magma bodies can initially erupt due to recharge associated over-pressurization and have frequent eruptions. Eventually, the increasing crustal temperature translates most magma bodies to the buoyancy overpressure part of the phase space.

In conclusion, we find that smaller magma bodies typically are easier to erupt than larger magma bodies. We find that pore pressure diffusion is an important process for the upper crustal magma bodies, and this can significantly inhibit eruption likelihood. A magma body may eventually lose enough volatiles to the crust and/or trap low volume fraction magmatic volatiles by capillary trapping (e.g., Parmigiani et

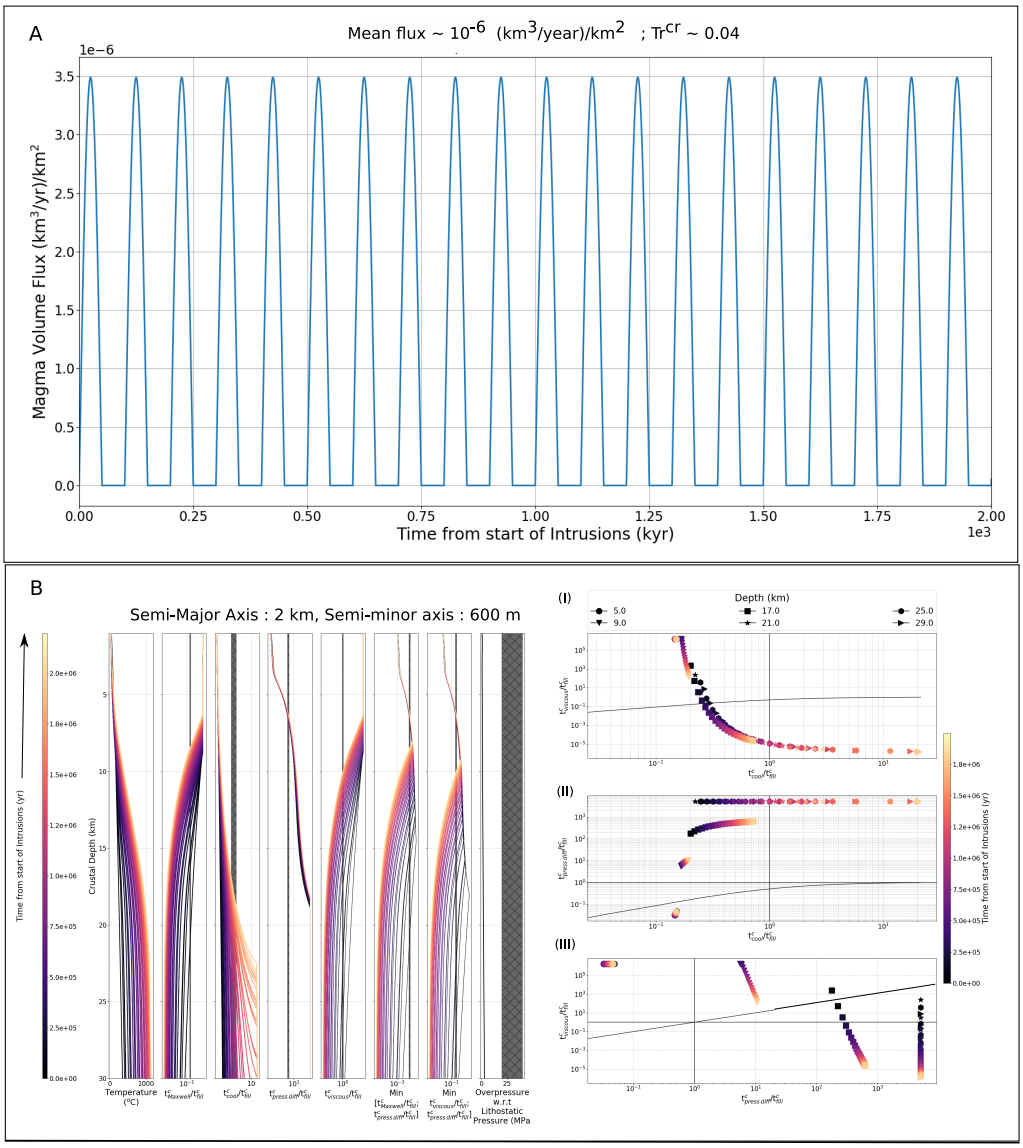

Figure 15: 1D thermal evolution model with constant melt input with a dike length-scale of 15 km (w.r.t the base of the crust) for a small magma reservoir. The Figure panel on the top (Panel A) shows the time-history of melt flux into the crustal column. For each panel, the middle figure shows the thermal evolution of the crustal column as well as various non-dimensional timescales (Degruyter & Huber, 2014; Mittal & Richards, 2019) while the third figure shows the magmatic regime diagram for ascertaining the eruptibility of magma for reservoirs at different depths. The initial concentrations of water and CO_2 in the melt is calculated for 10% degree of partial melting with a mantle source composition of 750 ppm CO_2 and 0.23 wt % H_2O.

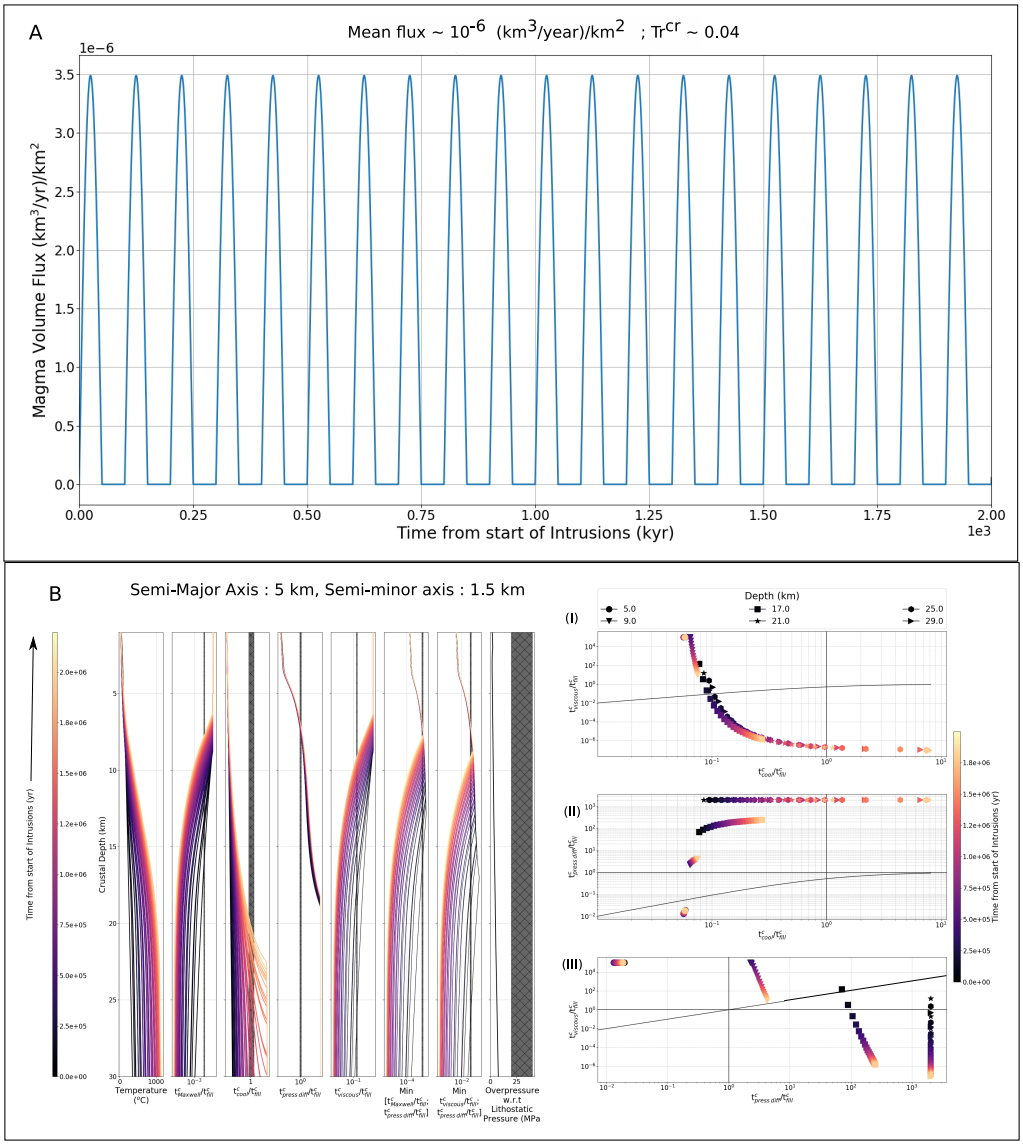

Figure 16: 1D thermal evolution model with constant melt input with a dike length-scale of 15 km (w.r.t the base of the crust) for a medium magma reservoir. The Figure panel on the top (Panel A) shows the time-history of melt flux into the crustal column. For each panel, the middle figure shows the thermal evolution of the crustal column as well as various non-dimensional timescales (Degruyter & Huber, 2014; Mittal & Richards, 2019) while the third figure shows the magmatic regime diagram for ascertaining the eruptibility of magma for reservoirs at different depths. The initial concentrations of water and CO_2 in the melt is calculated for 10% degree of partial melting with a mantle source composition of 750 ppm CO_2 and 0.23 wt % H_2O.

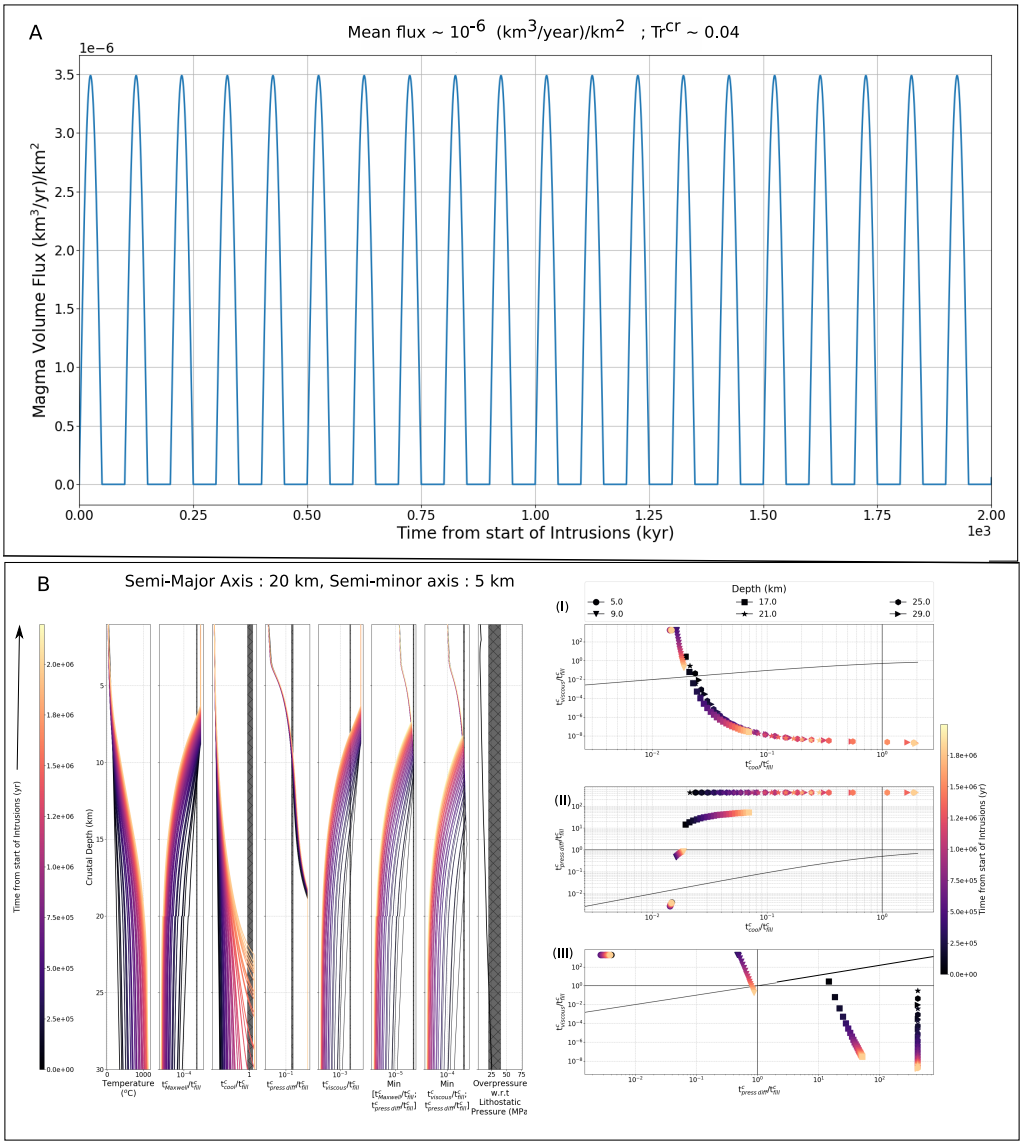

Figure 17: 1D thermal evolution model with constant melt input with a dike length-scale of 15 km (w.r.t the base of the crust) for a large magma reservoir. The Figure panel on the top (Panel A) shows the time-history of melt flux into the crustal column. For each panel, the middle figure shows the thermal evolution of the crustal column as well as various non-dimensional timescales (Degruyter & Huber, 2014; Mittal & Richards, 2019) while the third figure shows the magmatic regime diagram for ascertaining the eruptibility of magma for reservoirs at different depths. The initial concentrations of water and CO_2 in the melt is calculated for 10% degree of partial melting with a mantle source composition of 750 ppm CO_2 and 0.23 wt % H_2O.

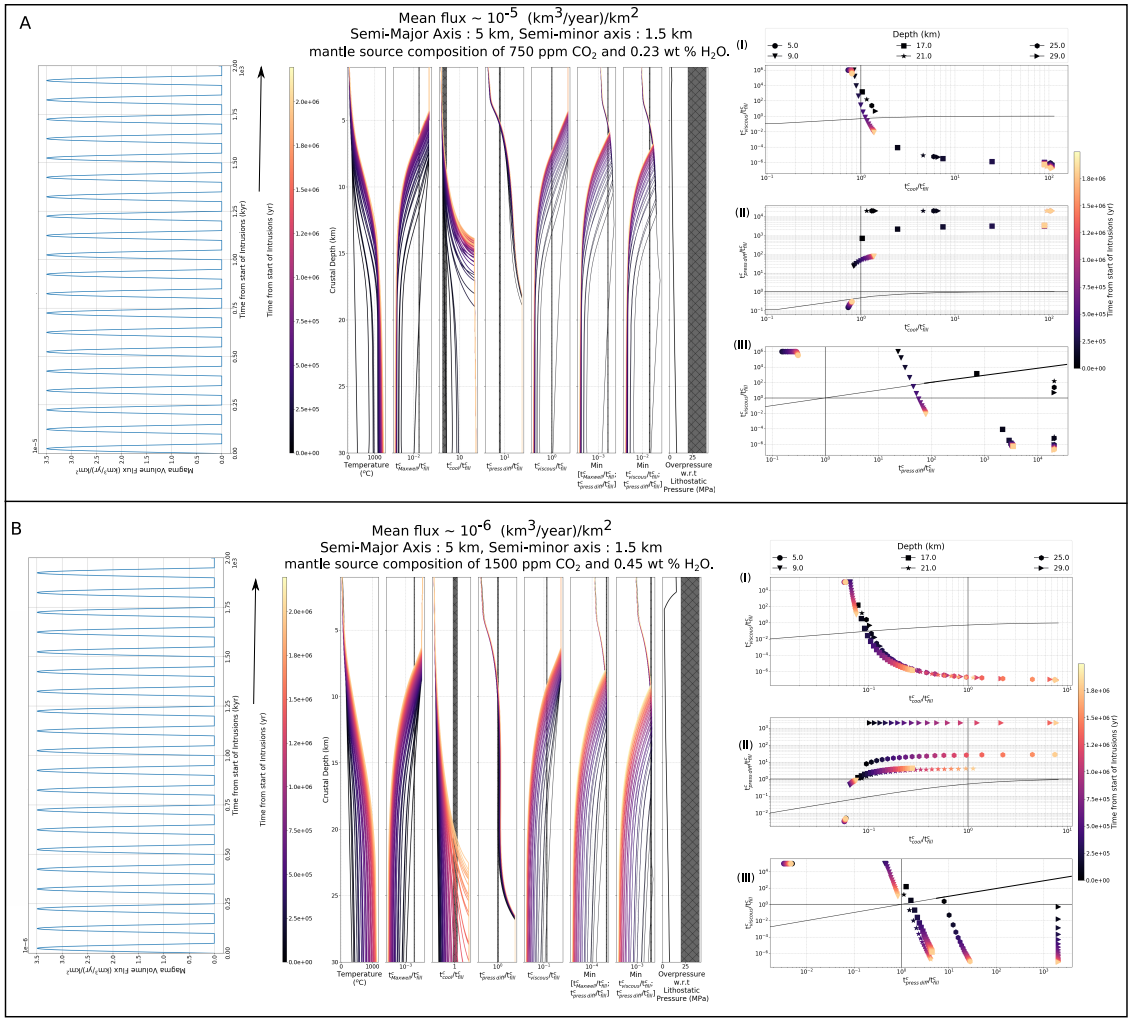

Figure 18: 1D thermal evolution model with constant melt input with a dike length-scale of 15 km (w.r.t the base of the crust). For each Panel, the Figure panel on the left shows the time-history of melt flux into the crustal column, the middle figure shows the thermal evolution of the crustal column as well as various non-dimensional timescales (Degruyter & Huber, 2014; Mittal & Richards, 2019) while the third figure shows the magmatic regime diagram for ascertaining the eruptibility of magma for reservoirs at different depths. The two sets of figure panels show the calculations for a same sized magma reservoir - 5 km semi-major axis, 1.5 km semi-minor axis, with different melt input fluxes and mantle volatile composition (Panel A, B, also see Figure 16). The initial concentrations of water and CO_2 in the melt is calculated for 10% degree of partial melting with a mantle source composition of 750 ppm CO_2 and 0.23 wt % H_2O (Panel A) and 1500 ppm and CO_2 and 0.46 wt % H_2O (Panel B)

al., 2016) to become volatile depleted and eruptible by other mechanisms. Additionally, the formation of a thermal aureole around the magma reservoir may also decrease the efficiency of pore pressure diffusion (See discussion in Mittal & Richards, 2019). Nevertheless, volatile loss by passive degassing is likely a significant stress relaxation process in the upper crust. For mid-crustal magma bodies, we find that the eruption mechanism and hence eruption frequency depend sensitively to the mass influx rate as well as melt volatile content. In particular, higher melt flux allows recharge-driven frequent eruptions for a 5 km x 1.5 km magma body at 9-15 km depths (Figure 18A). In contrast, the higher crustal temperature and corresponding lower viscosity make buoyancy overpressure the only viable mechanism for eruptions.

4.3 Plume-type melt flux

Since there are significant changes in both input melt flux and the degree of partial melting during a CFB event, we represent the crustal melt input as a Weibull distribution function with some additional noise following Black and Manga (2017) (Figure 19A). The degree of partial melting also follows the same functional form with a maximum of 10 % (e.g., Mahoney, 1988). To first order, this functional form approximates the observed pattern of alkali melts at the start and the end of the Deccan Traps main phase volcanism (Section 3.1, Section 3.2 Paper I). The peak melt crustal melt flux is about 10^{-5} (km^3/year)/km^2, equating to about 7.5 km^3/year over a 500 km radius plume head (or equivalently $\sim$ 1.5 km^3/year for a 200 km radius). In Figures 19, 20, and 21 we show the results of this model set up for a small, medium, and large magma reservoir size (a^c, b^c): 2km, 600m; 5 km, 1.5 km; and 20 km, 5 km respectively.

Compared to the results in Figure 18A, the main difference is that initially the degree of melting is very small ($\sim$ 1 %), leading to very volatile-rich initial melts. Consequently, significant CO_2 exsolution occurs in the lower crust, which in turn ensures a non-zero crustal permeability in the cold crust. With an increasing degree of melting, the volatile content decreases with a consequent increase of De_{pd} in the lower crust. Eventually, the degree of melting decreases and the melt's volatile content increases again. The strong effect of changing degrees of partial melting can be seen in the De_{pd} vs. De_{visc} phase space panels in Figures 19, 20, and 21. Since the crustal viscosity progressively decreases during a CFB event, the trajectories loop back but are not closed loops.

For the small sill shaped magma body (a^c, b^c - 2 km, 600 m), pore-pressure diffusion is the primary stress relaxation mechanism at upper crustal depths (5 km) throughout the calculations and the mid-crustal depths (9 & 17 km) for the initial part (Figure 19B, Right Panel III). Analyzing the corresponding phase space plot (Figure 19B, Right Panel II) for these magma bodies, we find that the shallow depth reservoir remains within the buoyancy overpressure regime. In contrast, the others are in the recharge-dominated regime permitting frequent eruptions. Given the small vertical extent of the magma body, the buoyancy overpressure is small even with high volatile content (Figure 19B). Consequently, the eruption of the shallowest magma reservoir seems potentially tricky. However, we posit that since these magma bodies are close to the region of recharge dominated eruptions, stochastic variations in the input melt flux (loops in the phase space, Figure 13C) may be sufficient to enable eruptions.

Furthermore, if we account for a potentially larger fraction of the plume melt flux feeding the magma reservoirs instead of being emplaced in the crust as dikes, we can further translate the trajectories towards the top right corner. Considering depths where viscous stress relaxation dominates, we find that mid-crustal magma bodies typically start in the recharge-dominated regime before transitioning at various times to the buoyancy regime with increasing temperature (Figure 19B, Right Panel I).

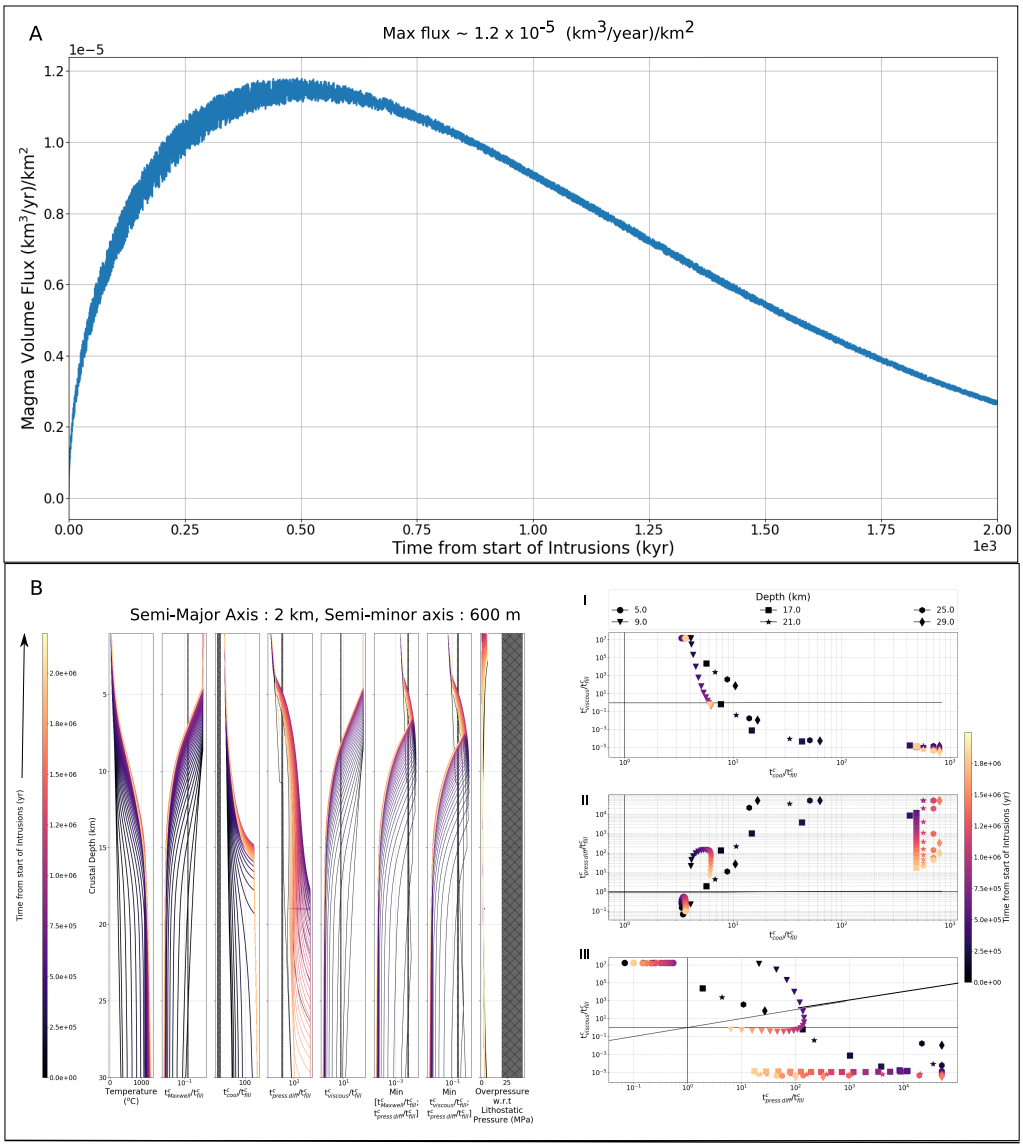

Figure 19: 1D thermal evolution model with time-varying melt input and a dike length-scale of 15 km (w.r.t the base of the crust) for a small magma reservoir. The input melt flux as well the degree of partial melting follow a weibull distribution (as shown the top figure panel A) to approximate the melting history from a flood basalt event. The initial concentrations of water and CO_2 in the melt is calculated for temporally varying degree of partial melting (maximum of 10 %) with a mantle source composition of 750 ppm CO_2 and 0.23 wt % H_2O.

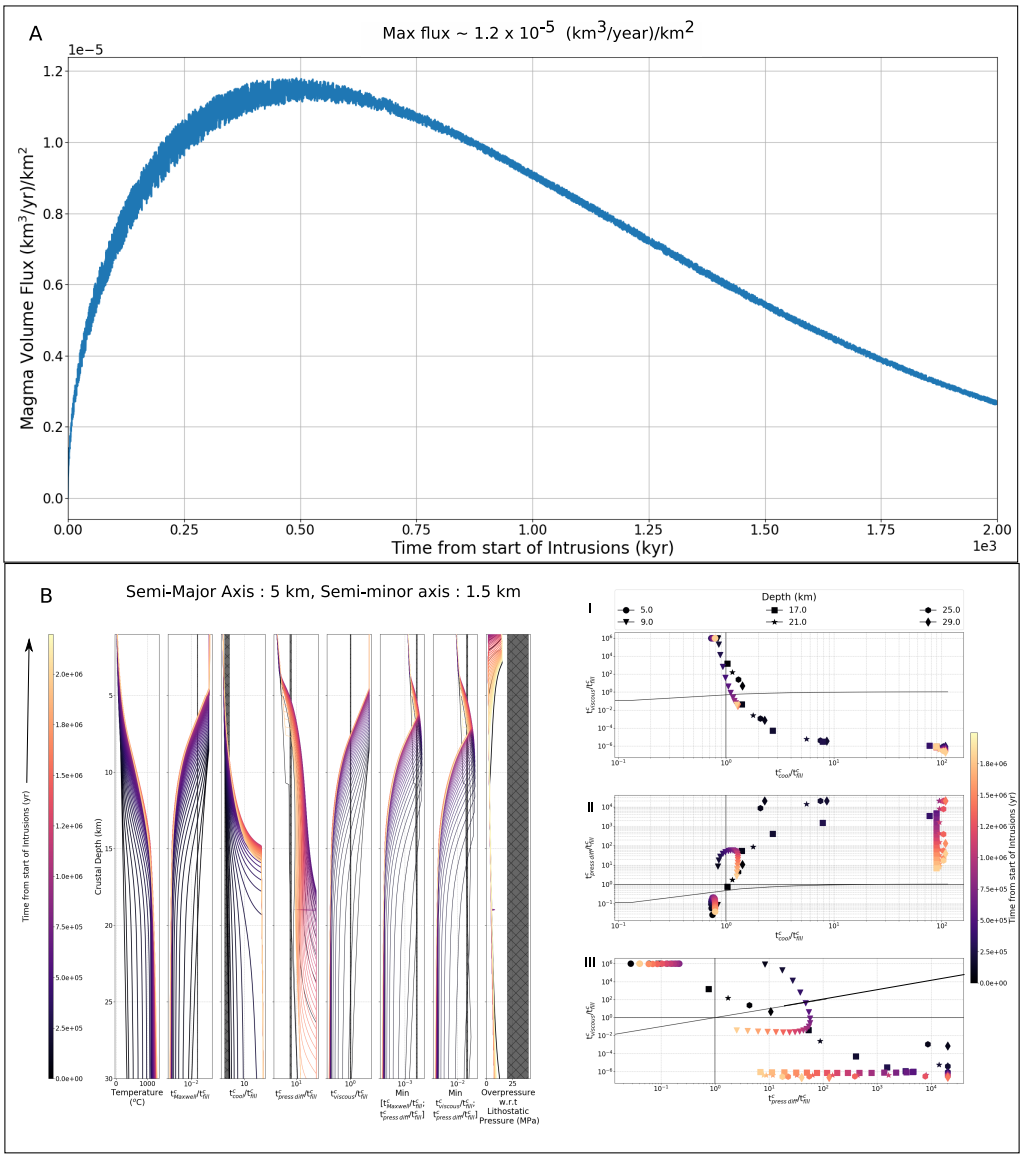

Figure 20: 1D thermal evolution model with time-varying melt input and a dike length-scale of 15 km (w.r.t the base of the crust) for a medium magma reservoir. The input melt flux as well the degree of partial melting follow a weibull distribution (as shown the top figure panel A) to approximate the melting history from a flood basalt event. The initial concentrations of water and CO_2 in the melt is calculated for temporally varying degree of partial melting (maximum of 10 %) with a mantle source composition of 750 ppm CO_2 and 0.23 wt % H_2O.

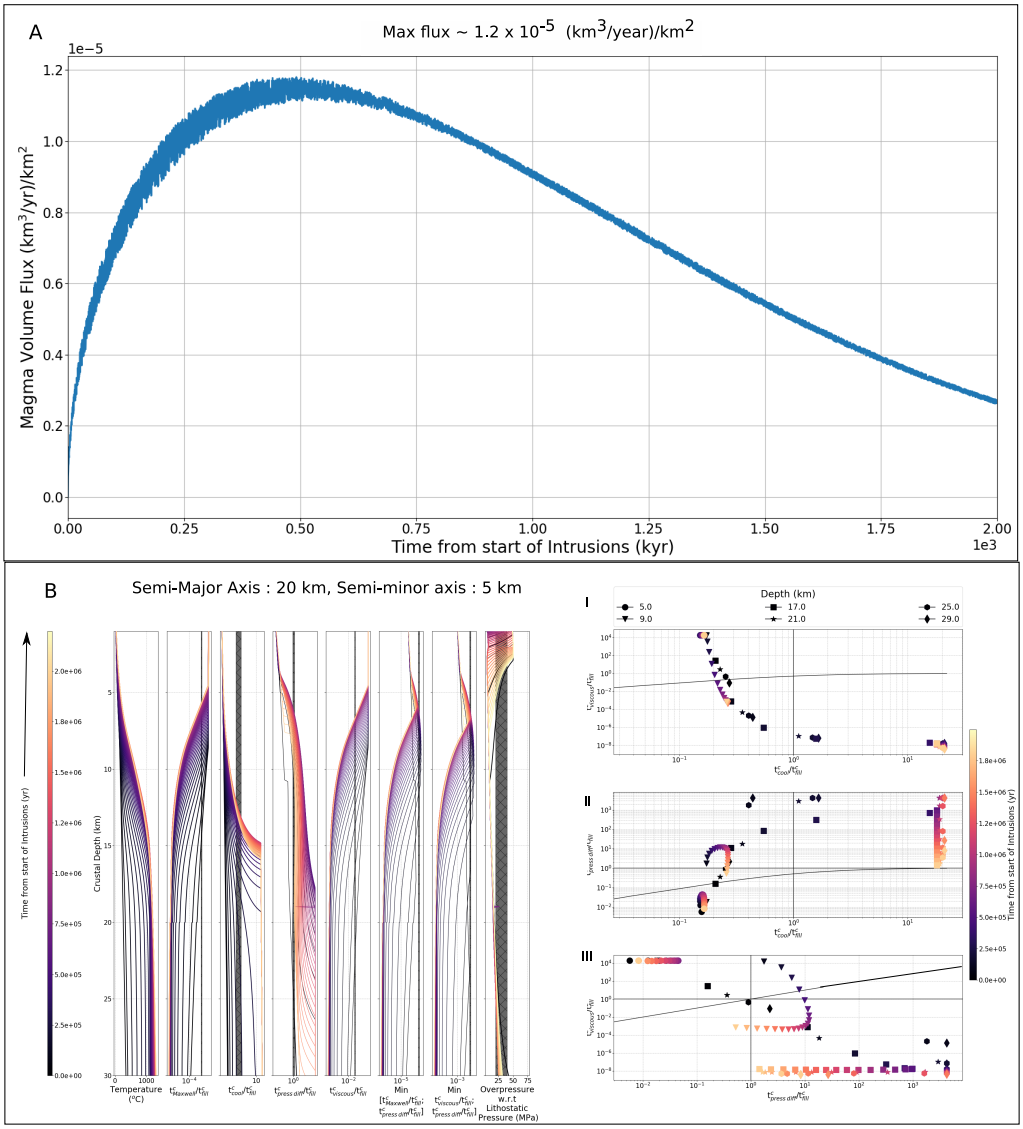

Figure 21: 1D thermal evolution model with time-varying melt input and a dike length-scale of 15 km (w.r.t the base of the crust) for a large magma reservoir. The input melt flux as well the degree of partial melting follow a weibull distribution (as shown the top figure panel A) to approximate the melting history from a flood basalt event. The initial concentrations of water and CO_2 in the melt is calculated for temporally varying degree of partial melting (maximum of 10 %) with a mantle source composition of 750 ppm CO_2 and 0.23 wt % H_2O.

Thus, while small sized mid-crustal bodies can frequently erupt with minimal growth rate, lower crustal bodies will typically erupt very infrequently and accumulate mass over time.

We find broadly similar results for the larger magma reservoir (a^c, b^c - 5 km, 1.5 km) with recharge associated eruptions likely for upper-crustal and mid-crustal magma bodies, especially after including some melt influx variability (Figure 20B, Left Panels I & II). The eruption likelihood is further enhanced by the larger buoyancy overpressure (due to the larger vertical extent of the magma body) for the upper crustal bodies. Thus, the additional elastic overpressure required for an eruption is lower. Consequently, all the trajectories will be translated upward further, making recharge or volatile-exsolution associated eruptions likely (Figure 13C, red arrow). In contrast, medium sized magma reservoirs are not expected to erupt frequently in the lower crust and will instead grow rapidly over time.

Finally, for the largest magma body (a^c, b^c - 20 km, 5 km), the right downward translation of phase space trajectories (Figure 21B, Left Panel I; Figure 13C) moves several magma bodies into either the no-eruption regime or the volatile exsolution regime. Thus, we expect infrequent eruptions if at all in this scenario. We note that the buoyancy overpressure is much higher, especially in the upper crust due to the coupled CO_2- H_2O exsolution as well as in the lower crust due to higher crustal density. Thus, some of the shallow, as well as lower crustal bodies, would likely be eruptible (Marsh, 1989).

4.4 Implications for CFB architecture

In conclusion, we find that at upper and mid-crustal depths, a medium-sized magma body ($a^c, b^c \sim$ 5 km, 1.5 km) is the optimal geometry given the requirement for frequent eruptions as well as being able to erupt sufficient volume in each eruptive episode (e.g., Figure 6, Section 3, Paper I). Additionally, we have some direct evidence of similarly sized intruded magma bodies in the DT geophysical datasets (Section 6, Paper I).

In the lower crust, however, viscous stress relaxation is too rapid to permit any other eruption mechanism (among the ones considered here) besides buoyancy overpressure. This result is, however, very challenging to reconcile with the requirement for frequent surface eruptions. The results from Black and Manga (2017) clearly illustrate that large magma reservoirs with failure due to buoyancy overpressure have a long hiatus between eruptions (also see Section 2.2.3, Figure 13B). Furthermore, there is clear geochemical evidence for significant lower crustal assimilation - fractional crystallization in the erupted lavas (e.g., Mahoney, 1988; Sen, 2001, and references therein, Section 3.1, Paper I). Thus, the erupted magmas spent some time in lower crustal magma reservoirs.

In order to address these challenges, we posit that we are missing a critical physical process in our model framework - the viscous flow of the surrounding country rock and formation of vertically extensive but spatially limited melt pathways (Cao et al., 2016; Rummel et al., 2018; Seropian et al., 2018; Colón et al., 2019). We envision that initially, the parental melt is stochastically emplaced in the lower crust with infrequent recharge into a single magma body (large Tr^c). As long is $T_{period}/t^c_{cool} \sim$ 0.1 - 1, individual magma bodies can cool sufficiently to produce buoyancy overpressure but still remain eruptible (Marsh, 1989, 2013). This buoyancy overpressure, in turn, leads to magma flow towards the top of the magma reservoir along (and associated crustal deformation) with the potential formation of non-elastic weak shear zones as well as brittle-ductile or ductile dikes (Scheibert et al., 2017; Bertelsen et al., 2018; Seropian et al., 2018; Haug et al., 2018; Kjøll et al., 2019). These deformation pathways can be used by the magma body to ascend to shallower depths. Typically, the critical

overpressure is lower for these mechanisms in comparison to tensile failure (Cao et al., 2016). Thus, over time, the magma body would become vertically extended with larger column-integrated buoyancy which further promotes deformation/tensile failure. Due to decreasing crustal temperature, as well as changes in the upper crustal rheology, the efficiency of this process will eventually decrease, and magma reservoir failure would become dominated by brittle tensile failure (Cao et al., 2016; Rummel et al., 2018) at mid-crustal depths. Additionally, the lower density of the middle crust reduces the magma-crustal density difference (e.g., Figure 21B). Since this cannot be compensated by increased volatile exsolution until shallower depths, the overall driving buoyancy pressure will also decrease (Figure 8).

We hypothesize that a combination of larger buoyancy overpressure, shorter absolute cooling timescales for a small reservoir, and periodic large melt influx (leading to more elongated Tr^c loops, Figure 13C) allow frequent eruptions from the lower crust. As the CFB magmatic system matures, we envision that the lower crustal magmatic system develops quasi-connected conduit style pathways analogous to the four ultramafic intrusions in the Seiland igneous province (Larsen et al., 2018). The area of each of these intrusions is only a few 100 km^2, but they have roots of up to 9 km. We note that a variety of physical mechanisms can form ductile shear zones. These include shear heating and thermal softening by small shear strains leading to spontaneous ductile shear zone generation (e.g., Kiss et al., 2019), reaction-weakening caused by infiltration of fluids (Mancktelow & Pennacchioni, 2005; Sørensen et al., 2019), or fabric development in rock with significant mechanical heterogeneities (Montési, 2013). Thus, the formation of weak zones can occur under a wide variety of thermomechanical conditions for the lower crust and is observed in some exhumed rift margins and magmatic bodies (Wenker & Beaumont, 2018; Tetreault & Buiter, 2018; Koptev et al., 2018; Francois et al., 2018; Korchinski et al., 2018; Kjøll et al., 2019; Sørensen et al., 2019; Lee et al., 2020).

5 New Conceptual Model for CFB magmatic system

Based on the observational constraints as well as the results from the magma reservoir model and thermal model, we propose a new conceptual model for CFB volcanism. *The key feature of this model is that individual CFB eruptive episodes are fed by a series of small interconnected trans-crustal magma reservoirs instead of a single large magma reservoir.* In Figure 22, we show a schematic representation of this model with three stages of CFB volcanism: Early phase, Main phase, and Late-stage continental flood basalt volcanism. Our proposed model structure builds upon various conceptual CFB magmatic architectures (Section 2.1, Paper I). In particular, our results closely resemble the proposed model for the Ethiopian Traps by Krans et al. (2018) as well as H. C. Sheth and Cañón-Tapia (2015) to explain composite Deccan Trap dikes. However, we can constrain the magmatic structure more quantitatively, especially with regards to the size of individual magma reservoirs and the physical processes driving eruptions. We acknowledge that a real continental flood basalt such as the Deccan Traps likely had multiple eruptive centers (e.g., Section 3.2,) as well as different sources of parental melt source compositions (Section 3.1). In the following, we do not attempt to explain this full geochemical complexity. Instead, our conceptual model is focused on explaining the overall eruptive tempo and some key geochemical features of CFBs.

5.1 Stage 1a : Early Phase Flood Basalt

Initially, low-degree melts from partial melting in the mantle plume head and the metasomatized mantle lithosphere ascend through some combination of brittle-ductile dikes (Havlin et al., 2013; Kjøll et al., 2019), diapiric melt bodies, and two-phase melt

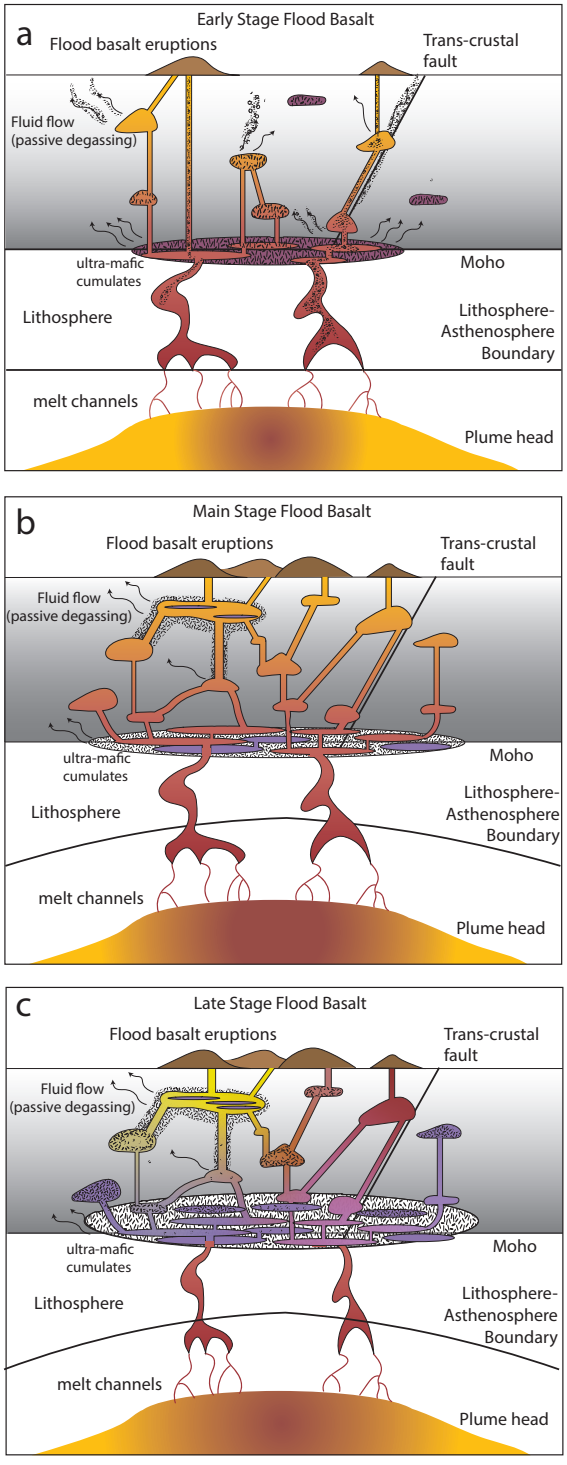
a
Early Stage Flood Basalt
Flood basalt eruptions
Trans-crustal fault
Fluid flow (passive degassing)
ultra-mafic cumulates
Moho
Lithosphere
Lithosphere-Asthenosphere Boundary
melt channels
Plume head
b
Main Stage Flood Basalt
Flood basalt eruptions
Trans-crustal fault
Fluid flow (passive degassing)
ultra-mafic cumulates
Moho
Lithosphere
Lithosphere-Asthenosphere Boundary
melt channels
Plume head
c
Late Stage Flood Basalt
Flood basalt eruptions
Trans-crustal fault
Fluid flow (passive degassing)
ultra-mafic cumulates
Moho
Lithosphere
Lithosphere-Asthenosphere Boundary
melt channels
Plume head

Figure 22

Figure 22 *(previous page)*: Conceptual model for the magmatic structure of a continental flood basalt sequence in three stages : Early Stage Flood Basalts (Panel A), Main Stage Flood Basalts (Panel B), and Late Stage Flood Basalts (Panel C). The most voluminous surface eruptions occur during the Main Stage Flood Basalts while the maximum passive degassing typically occurs towards the end of Early Stage CFBs. The darker colors in the plume head signify the degree of partial melting which increases from Early stage to Main stage and decreases again in the Late Stage. In the crustal magmatic system, the light yellow color (Late Stage Panel C) indicates the presence of a rhyolitic magma reservoir. In all the panels, the shaded crustal grayscale colors represent the background geotherm.

channelization (Aharonov et al., 1997; Katz et al., 2006; Solano et al., 2012; Weatherley & Katz, 2012; Keller et al., 2013; Weatherley & Katz, 2015; Schmeling et al., 2018, 2019). Since these melts are highly volatile enriched (Katz et al., 2003; Black & Gibson, 2019), they can exsolve significant CO_2 during decompression even at lower crustal depths (1st boiling, Edmonds & Wallace, 2017, Figure 19B). These melts are thus expected to be very buoyant, highly compressible, and have a lower solidus temperature (Black & Gibson, 2019; Yaxley et al., 2019). As a consequence, these melts can erupt to the surface from deep crustal reservoirs by buoyancy overpressure alone without much mid/upper crustal storage (Black & Manga, 2017). The typical magma reservoirs feeding these eruptions are expected to be either medium-sized ellipsoidal bodies or small but vertically elongated magma bodies. In some cases, the erupted melts ascend through the crust rapidly enough to carry mantle and lower crustal xenoliths (e.g., Ray et al. (2016); alkali basaltic lava flows and dikes in Kutchh subprovince). Additionally, the pre-existing crustal tectonic structure, such as old faults and shear zones, serve as important controls on the melt transport, volatile degassing, and the location of eruptions (e.g., Latyshev et al., 2018) Siberian Traps, Section 5 (Paper I) for Deccan Traps observations, Gettysburg Sill associated with CAMP (Mangan et al., 1993), and the Franklin sills (Bédard et al., 2012)).

5.2 Stage 1b : Early Phase Flood Basalt

Over time ($\sim 10^5$ - 10^6 years), the melt's volatile content will decrease due to increasing degrees of partial melting. Thus, individual Moho-depth magma reservoirs will not have enough buoyancy overpressure due to decompression alone. Also, the magmatism will progressively heat the lower crust. As a consequence of these two effects, parental melts will start accumulating at depth in several small-medium sized bodies rather than erupting. With progressive cooling and differentiation and associated volatile exsolution (Karlstrom & Richards, 2011), the buoyancy overpressure will increase. Coupled with non-tensile failure mechanisms, the higher buoyancy pressure will enable the development of small, stacked but vertically extensive magma bodies (or at least melt bodies which are temporarily connected vertically, See Section 4.4). We posit that eventually these processes will lead to an efficient conduit style lower crustal transport system even within an overall stacked sill style system. For lower melt flux CFBs (e.g. the Snake River Plains), the system may never transition to this fully connected regime leading to more sporadic surface eruptions with more geochemical variations between flows fed by individual sills/set of sills (Potter et al., 2018; Shervais et al., 2006).

In conclusion, we propose that during Stage 1 of a CFB, the initial eruption efficiency (and frequency) from the lower crust will be very high. It will subsequently decrease before increasing again towards the end of Stage 1. To have this initial increase (as well as match observations), it is critical that the lower crustal magmatic system

is not a single large magma reservoir but is instead comprised of a small-medium sized (few 100 km^3) magma body embedded in a mush zone.

We propose a similar time progression for the mid and upper crustal magma bodies. Initially, the shallower crust is both colder and has high permeability. Thus, there is initially a high likelihood for the magma reservoir to freeze in place and lose most of its volatiles to the surrounding crust leading to high cooling rate (Hepworth et al., 2020). Over time, both the mantle melt flux and the lower crustal melt transport efficiency will increase along with higher crustal temperatures. These changes will enable mid-upper crustal magma to remain eruptible for longer, reduce the effectiveness of pore pressure diffusion, and permit eruptions by recharge associated overpressure (See Section 4.3 and 4.4). Additionally, the presence of potentially more eruptible magma bodies will permit an individual eruption to include more secondary reservoirs with progressively decreasing conductivity timescales and higher conductivity (Sections 5.2.3, 5.3.1). Thus, we expect that both the eruption frequency as well as the volume of individual eruptive episodes would increase towards the end of Stage 1.

We emphasize that the same set of magma reservoirs do not need to feed each eruptive episode. Instead, each eruption represents a stochastic network of magma reservoirs that can connect depending on the crustal stress state, their internal overpressure, and eruptive history. Conceptually, this is similar to the idea of an open-system trans-crustal magamatic system that has been proposed for present-day arc volcanism (Marsh, 2013; Cashman et al., 2017; Bergantz et al., 2015). Typically, a given magma reservoir will only be part of an eruption episode every 0.5-5 kyr. Thus, there is sufficient time for shallow plagioclase fractionation despite relatively frequent eruptive episodes (Section 3.3, 3.4, 3.5, Paper I). The crustal residence time for some of the upper crustal magma bodies erupted towards the end of Stage 1b may be particularly long (e.g., 2-10 kyr) since the system is transitioning from a low to a high eruption probability. Thus, recharge driven individual eruptive episodes may entrain the magmatic mushes (both the melt and the large plagioclase crystals) from the primary or secondary reservoirs in some cases. Mush disaggregation and entrainment by a carrier melt has been geochemically shown to be an important process during the Laki 1783 eruption, a modern CFB analog (Passmore et al., 2012; Neave et al., 2017) as well as a number of modern ocean island basalts (Gleeson et al., 2020). In particular, the ocean island observations suggest that with increasing mantle melt fluxes, the primary mush zone feeding the eruption moves from mantle lithosphere depths to shallower crustal levels(Gleeson et al., 2020). For CFBs in particular, Capriolo et al. (2020) found that the CO_2 rich melt inclusions were geochemically distinct from their surrounding rock suggestive of recharge and transport of magmatic cargo from magmatic mushes. Finally, similar processes have also suggested explaining the occurrence of GPB flows with large concentrations and sizes of plagioclase phenocrysts in the Deccan Traps (Beane et al., 1986; Higgins & Chandrasekharam, 2007; Krishnamurthy, 2019) as well as the Iceland Neogene flood basalts (Óskarsson et al., 2017) and the Emeishan province (L. Cheng et al., 2014; L.-L. Cheng et al., 2014). Based on Sr isotope zoning in plagioclase crystals as well as crystal size distributions, Higgins and Chandrasekharam (2007); L. Cheng et al. (2014); Borges et al. (2014) inferred a GPB growth timescale of up to a few thousand years (See H. Sheth (2016) for more discussion and alternative models). Concerning the DT, we envision that the Kalsubai sub-group with several GPBs represents the end of Stage 1 of the CFB magmatic system.

Finally, with regards to passive degassing of magmatic volatiles, we expect an initial increase in degassing efficiency due to crustal melt storage and high permeability followed by a decline due to thermal maturation of the crust. The total volume of magmatic volatiles degassed depends on both the efficiency of degassing as well as the shallow melt volume. Thus, we anticipate that the peak passive degassing will be

shifted closer towards the end of stage 1 coincident with increasing surface eruptions. This physical mechanism (briefly suggested in Sprain et al. (2019)) thus provides a natural explanation for the observed pre-K-Pg global warming observed in a various marine and terrestrial paleo-proxy records (Hull et al., 2020) which is co-incident with the eruption of Kalsubai sub-group (Sprain et al., 2019; Schoene et al., 2019).

We readily acknowledge that this temporal pattern does not include any potential carbon release from heating and assimilation of country rocks. Multiple studies have suggested that this additional carbon source, primarily due to crustal heating by shallow sill complexes, is critical for CFBs such as Siberian Traps, Karoo, CAMP, and NAMP (Svensen et al., 2018, and references therein). Since the shallow sill network may be emplaced after the lava flows (Section 6.4, Paper I) due to the mechanical loading at the surface, the temporal rate of passive degassing for these systems can be significantly modified.

5.3 Stage 2: Main Stage Flood Basalt

With increasing mantle melt flux, shallowing lithosphere-asthenosphere boundary (N. Kumar et al., 2013; H. Wang et al., 2015; Maurya et al., 2016; Dessai et al., 2020), along with a higher degree of partial melting and the development of vertically integrated melt pathways in the lower crust, the CFB system transitions to Stage 2- Main stage flood basalt sequence. During this time period, the mid-upper crustal magmatic system is composed of a set of small-medium (5-15 km semi-major axis) magma bodies that progressively become more connected over time (higher conductivity and lower conductivity timescale). This, in turn, leads to both larger and potentially shorter eruptions since the conductivity timescales are faster (e.g., Wai subgroup flows, especially Poladpur, see Section 3.3 Paper I). Additionally, with increasing magma mixing and rapid eruptions, the magmatic system becomes geochemically homogenized through REAFC/RTF style processes (e.g., K. Cox, 1988, Section 2.2 Paper I). The geochemical variations are further reduced by less crustal interaction due to basaltic plating as well as a similar themo-chemical environment for the different crustal magma bodies (Mahoney, 1988; Chatterjee & Bhattacharji, 2008; Yu et al., 2015; Larsen et al., 2018; Heinonen et al., 2019; Potter et al., 2018). Due to the high rate of magma recharge as well as restricted reservoir size, eruptions are frequent and primarily recharge rate driven.

We hypothesize that during Stage 2, the magmatic stresses determine the crustal stress field instead of far-field tectonic stress. For the DT, this is potentially illustrated by changes in the orientation of dike swarms over time from being more oriented (and feeding the lower Formations, e.g., Narmada-Tapi Swarm) to less oriented (feeding Wai subgroup, e.g., Central Dike swarm Vanderkluysen et al. (2011); M. A. Richards et al. (2015) and Section 5.1). Towards the end of Stage 2, the decreasing crustal viscosity (due to higher temperatures) will potentially lead to longer and larger individual eruptive episodes but with slightly reduced eruption rates (e.g., Ambenali flows, see Section 3.3 and 5.2.2). We note that within our conceptual model, the rapid transitions between geochemical formations is challenging to explain. These abrupt changes may be indicative of either state transitions in the magmatic system due to "thermo-poro-chemo-elastic" interactions between magma reservoirs (Parks et al., 2017; Elshaafi & Gudmundsson, 2018; Albino et al., 2019; Mittal & Richards, 2019; Belardinelli et al., 2019) or spatial changes in eruptive centers with a separate plumbing system (e.g., Wolff & Ramos, 2013, for Columbia River Basalts). For the Deccan, the potential change in dike swarms feeding individual geochemical subgroups provides some support for this hypothesis.

5.4 Stage 3: Late Stage Flood Basalt

Eventually, the mantle melt flux into the system decreases along with a lower degree of melting of a depleted mantle plume head. Thus, although the volatile content of the magmas is potentially higher than "main-phase" CFBs, it is insufficient to allow frequent eruptions (akin to Stage 1a) through a hot crust. Additionally, over time, the deep crustal rheology also evolves due to metamorphic reactions as well as the continued influx of CO_2 rich fluids and magma (e.g., Larsen et al., 2018). Typically, these processes would lead to a weaker lower crust (Black & Gibson, 2019; Bürgmann & Dresen, 2008; Karlstrom & Richards, 2011). The lower crustal viscosity is further reduced due to the lower viscosity of the large cumulate ultramafic region (composed primarily of clinopyroxene and olivine, M. Richards et al., 2013) vis-a-vis a typical continental crust (some anorthite and clinopyroxene, Karlstrom & Richards, 2011). Thus consequent faster viscous relaxation leads to both faster lower crustal flow (disrupting melt transport pathways) as well as reduced efficiency of recharge to trigger eruptions. In aggregate, the eruption efficiency in the system progressively decreases. Some of the larger lower and upper crustal magma bodies can persist for a long time, slowly building up buoyancy but never being sufficient to erupt to the surface. Furthermore, continued crystallization and solidification front instabilities (Marsh, 2002) can generate rhyolitic magmas that erupt towards the end of the DT eruptive sequence (Section 3.2, Paper I). If there is some continental rifting in this time-period, the eruption of both shallow and deep melts become easier (e.g., the Mumbai sequence, Hooper et al., 2010). It is noteworthy that for Deccan in particular, we have limited information of the eruptive tempo and composition of the massive offshore volcanism and the rift formation (Fainstein et al., 2019). Thus, it is very likely that the part of our Phase 3 was interrupted by continental rifting initiating a new oceanic spreading center (Yatheesh, 2020).

Within our conceptual model framework, the typical one million year duration of "main phase" CFB volcanism is a consequence of two related processes. Firstly, the thermal maturity of the crust decreases due to reduced melt flux with plate motion over the mantle plume. Thus, it is difficult for smaller magma bodies to remain eruptible. Secondly, with an increase in the size of the connected magma reservoirs (Biggs & Annen, 2019), especially in the lower crust, the eruption efficiency by any mechanism other than buoyancy becomes harder. As illustrated by Black and Manga (2017), there is a long hiatus time before large magma bodies can build up buoyancy overpressure and erupt. We posit that towards the end of the CFB sequence, this overpressure condition may never be achieved due to decreasing melt input.

6 Discussion

6.1 What makes CFB eruptive episodes unique ?

Individual eruptive episodes in continental flood basalts are unique compared to any modern basaltic volcanic system (e.g., Hawaii and Iceland), with much larger erupted volumes and eruption durations, but not necessarily larger flux rates. Nevertheless, we propose that a CFB magmatic system can still be considered as a scaled-up version of these modern analogs with one key difference. As we show with our model results, the larger magma flux from a mantle plume head (and the consequent thermal input) allows multiple magma bodies to remain thermally viable with a high likelihood of inter-reservoir connectivity due to thermo-poro-mechanical processes (e.g., Belardinelli et al., 2019; Mittal & Richards, 2019; Mindaleva et al., 2020). This larger flux enables larger, longer CFB eruptions over a large distributed region rather than the formation of a single surface volcano and associated upper crustal conduit system.

Although our primary argument for a multiply-connected magma reservoir model is observational (to match eruptive tempo constraints), there are also physical reasons why we may expect this magmatic architecture to dominate over single large well-mixed magma reservoir structure. Firstly, it is physically challenging (from a thermodynamics standpoint) to sustain large well mixed magma bodies and studies on modern magmatic systems are increasingly illustrating that magma bodies typically have a large mush zone (Marsh, 2013; Cooper, 2015). Even for a high, spatially localized, mantle flux region such as Hawaii, the presence of magmatic mushes and multple distinct magma bodies is clear from a combination of geophysical and geochemical datasets (Marsh, 2013; Wright & Marsh, 2016; Wieser et al., 2020; A. N. Anderson et al., 2020; C. A. Neal et al., 2019). Thus, it is difficult to have a large thermally viable well mixed single magma reservoir. Secondly, CFBs are associated with a high (potentially comparable to Hawaii, Iceland) melt flux over a large distributed region rather than a very small localized region. Thus, from a vertical melt transport perspective, it is natural to establish a large set of individual magma bodies. The establishment of a single magma reservoir is thus a potentially subsequent step in the system's evolution rather than a starting setup. Our analysis suggests that the conditions for this merger are typically not established for Phanerozoic CFBs. This challenge is further exacerbated by that fact that it is easier to erupt smaller magma bodies with magma recharge compared to large magma bodies that require sufficient buoyancy overpressure. Finally, as discussed in Paper I and clearly illustrated by the Deccan dike dataset, pre-existing tectonic structures play a signficant role in facilitating initial magma ascent to the surface. We thus posit, that it is very unlikely to establish regional scale magma bodies across these tectonic structures since the buoyant magma would typically like to erupt rather than spread laterally. The one exception to this argument is when a combination of far-field extensional stress, overburden stress, and hot low viscosity crust promotes melt accumulation during Stage 3 (e.g, sills in the McMurdo Dry Valleys,(Marsh, 2004)).

We note that we do not expect that the magmatic architecture of each CFB will be the same. Variations in plume composition, crustal and lithospheric structure and composition, and background tectonics all play a critical role in determining the magmatic plumbing structure of a given CFB. For instance, the eruption styles, as well as the volume of silicic components, vary significantly between CFBs. The Parana-Etendeka, Columbia River Basalts, and the Ethiopian Trap flood basalts have a significant silicic component, unlike Deccan Traps and Siberian Traps (Bryan et al., 2010). As described in Section 4.6 (Paper I), many CFBs are associated with large sill complexes that may have fed the overlying lava flows (Muirhead et al., 2012, 2014; Elliot & Fleming, 2018; Coetzee et al., 2019; Magee, Ernst, et al., 2019) and facilitated both long-distance lateral magma transport (Leat, 2008; Magee, Muirhead, et al., 2016) as well as magma transport vertically through the sill complex (Angkasa et al., 2017; Svensen et al., 2018; Galland et al., 2019; Magee, Ernst, et al., 2019).

Nevertheless, our results suggest that all these systems still need some form of a multiply-connected magmatic system to match constraints on the eruptive tempo and volume of individual eruptive episodes. In this work, we have exclusively focused on Continental Flood Basalts and not discussed their oceanic counterparts, such as the Ontong Java Plateau. Due to the different crustal structure (e.g., <7 km initial thickness) and crustal rheology, we anticipate that the magmatic architecture of the oceanic Large Igneous Provinces are very different (Karlstrom & Richards, 2011). Without additional geochronological, geophysical, and volcanological constraints for these systems, it is difficult to ascertain how similar eruptive episodes for oceanic LIPs are to CFBs (e.g., Kerr et al., 1997; Geldmacher et al., 2014; Pietsch & Uenzelmann-Neben, 2015; Hochmuth et al., 2015; Sager et al., 2019; Zhang et al., 2019; C. R. Neal et al., 2019, and references therein). Thus, we can not rule out the possibility that oceanic LIPs are erupted from large magma reservoirs with long hiatus. Nevertheless,

the prevalence of magma transport, storage, and differentiation over a range of crustal depths in multiple Oceanic Plateaus suggests a potentially transcrustal magmatic system (Tejada et al., 2002; Fitton & Godard, 2004; Reekie et al., 2019; van Gerve et al., 2020).

6.2 Testing the proposed CFB model

Our proposed CFB magmatic architecture model is principally based on observations from the Deccan Traps, particularly the Western Ghats region (Section 3, Paper I). Thus, additional high-precision geochronology and paleomagnetic datasets from other parts of the Deccan Traps, especially the Central Deccan region, would be very useful to better constrain the volume, number, and hiatus intervals between individual eruptive episodes. Additionally, improved constraints on the eruptive tempo - duration, flux rate, and frequency of eruptive episodes for other CFBs would help assess if our conceptual model is generally applicable or not.

Another useful test for our proposed model would be a combined analysis of lava flow geochemistry (major, minor, trace element & isotopic compositions, petrology, diffusion timescales), paleo-secular variation, and flow morphology in a single stratigraphic section with high precision Ar-Ar flow dates. Such an analysis would help temporally constrain the timescale for intra-flow variations as well as the eruptive rates and eruption frequency. In particular, differences in isotopic and geochemical compositions can be used to directly constrain the timescale of magma mixing, fractionation, and the input of more deep-seated melt flux/fluids between eruptive events. A similar analysis for a spatially extensive single physically traced flow unit (Vye-Brown, Gannoun, et al., 2013) will help test how homogeneous individual eruptive units are and if that is consistent with a multiply connected magmatic architecture.

Finally, we expect that the pattern of deformation due to recharge and eruption of an interconnected magma reservoir network will be different compared to a single large upper crustal magma reservoir. This topographic difference may impact the pattern of lava flow distribution and the spatial coverage of individual lava flows. Also, on a more local scale, the pattern of deformation may manifest itself in 5-50 km scale changes in relative elevation of a single flow as well as changes in flow morphology due to changes in slope (Bondre & Hart, 2008; Richardson & Karlstrom, 2019). At present, these variations are challenging to discern given the limited datasets and complexities associated with inflated sheet lobe formation (Vye-Brown, Self, & Barry, 2013; Rader et al., 2017). However, systematic studies can potentially help distinguish between single vs. multiple magma chamber models. Additionally, recent studies (O'Hara et al., 2019; Karlstrom et al., 2018) have illustrated that magmatic systems may imprint a strong signature on the overlying landscape with regards to the surface topography and erosion rates. We thus posit that a careful topographic analysis of CFBs may help constrain the structure of the shallow magmatic system.

6.3 Quantitative model of CFB magmatism

In this study, we use a set of idealized models (Section 2) to constrain the conditions required for CFB eruptive episodes. However, to self-consistently calculate how the eruptive tempo varies throughout a CFB event, a full thermo-chemo-physical model is required both for the crust and the plume associated lithospheric evolution (Black & Gibson, 2019; Dessai et al., 2020). Our results illustrate that such a model needs to have a few key features. Firstly, the magmatic system should be comprised of a multi-level network of small-medium sized magma bodies which interact through crustal thermo-poro-visco-elastic processes (e.g., Taron et al., 2009; Liao et al., 2018; Mittal & Richards, 2019; Beinlich et al., 2020) as well as direct recharge of melt and volatiles and their associated evolution (Snyder & Tait, 1995; Montagna et al.,

2015; Papale et al., 2017; Calogero et al., 2020). It is also essential to account for pre-existing tectonic structures and specific crustal properties since these strongly influence the location of magma bodies and their ability to ascend (e.g., presence or absence of a sedimentary basin). One should also include non-magmatic stresses due to uplift from the mantle plume head, continental rifting, and surface loading by lava flows (Hieronymus & Bercovici, 2001; Saunders et al., 2007; Karlstrom et al., 2009; Rooney et al., 2014; McGovern et al., 2015; Tibaldi, 2015; Blanchard et al., 2017; Ernst et al., 2019).

Secondly, the importance of magmatic volatiles for the eruptibility of a magma reservoir suggests that processes associated with magmatic fluid transport in the magmatic mush and the crust are critical (Mittal & Richards, 2019; Lamy-Chappuis et al., 2020). Additionally, influx or outflux of just the magmatic vapor phase can significantly affect the thermochemical properties of the magma reservoir (e.g., Marsh & Coleman, 2009; Caricchi et al., 2018). Since magma reservoirs likely have spatially variable amounts of melt, crystals and exsolved volatiles along with various layered and banded structures (e.g., Jerram et al., 2018, and references therein), it is challenging to model the volatile transport and mechanical response adequately with a volume averaged approximation and a single rheology (Marsh, 1996; Hildreth & Wilson, 2007; Bachmann & Bergantz, 2008; Marsh, 2013; Sparks et al., 2019; Carrara et al., 2019; Burgisser et al., 2020; Carrara et al., 2020). To accurately model the visco-elastic rheological response of a magma reservoir, it also important to consider changes in crustal assimilant due to thermal and fluid-driven metamorphic reactions (Aarnes et al., 2012). Lavecchia, Clark, et al. (2016) showed that depending on the P-T conditions, crustal strength in the proximity of the magmatic bodies could both increase and decrease along with changes in crustal density. Since a CFB event is associated with a large crustal-scale thermo-chemical perturbation, these processes are important to model the temporal evolution of the magmatic system (Lavecchia, Beekman, et al., 2016).

Finally, our results and observations suggest that a quantitative CFB model should include some mechanisms for visco-elastoplastic crustal deformation and the formation of shear zones/ductile fracture/two-phase flow channelization instabilities (Colón et al., 2019; Schmeling et al., 2018, 2019; Mindaleva et al., 2020; Beinlich et al., 2020). This introduces significant model complexity and high numerical resolution (Calogero et al., 2020). However without such processes, it is challenging to transport melt from lower crustal magma reservoirs into the upper crust without a long time hiatus. Since, we do not find evidence for such hiatuses in the Deccan Traps and other CFBs (Section 3.2 - 3.5, Paper I), we contend that a realistic flood basalt model should include, either directly or in a parametrized form, some non-tensile failure mechanisms (Kjøll et al., 2019).

7 Conclusions

Continental flood basalt provinces (CFB) are some of the largest magmatic events in Earth's history and are typically associated with global-scale environmental perturbations (Clapham & Renne, 2019). Individual eruptive episodes for CFBs have lava volumes much larger than any modern-day counterpart. The commonly accepted model to explain this observation is that individual eruptive episodes are fed by correspondingly large magma reservoirs that erupt due to buoyancy overpressure (Black & Manga, 2017, see Section 2, Paper I). However, it is difficult to validate this model due to the lack of surface exposure of these hypothesized magma bodies. In this set of two papers, we use constraints, both direct (geochronology; paleo-secular variation) and indirect (Hg chemostratigraphy; lava flow morphology), on the eruptive tempo of the Deccan Traps flood basalt province to show that the observations do not match the large magma reservoir model predictions (Section 3, Paper I). This conclusion is

1754 further supported by the pattern of inter- and intra-flow geochemical variations, as
1755 well as the absence of a large upper crustal magma reservoir in geophysical datasets
1756 (Section 4, 5, and 6; Paper I).

1757 Using a set of simplified magma reservoir mechanical models and 1D thermal
1758 calculations (Section 3 & 4), we find that the most plausible crustal plumbing system of
1759 CFBs is a multiply connected magmatic architecture with small-medium sized magma
1760 reservoirs (3-10 km semi-major axis, each a few hundred km^3 in volume). Individual
1761 eruptions are fed from a stochastic network of connected magma reservoirs, and this
1762 setup can help explain the eruptive flux, duration, and frequency of individual eruptive
1763 episodes. We propose that these small magma reservoirs are distributed throughout the
1764 crust and erupt due to recharge associated overpressure (for upper and middle crust).
1765 In contrast, buoyancy, along with non-tensile failure mechanisms, are responsible for
1766 the development of a vertically extended, but spatially limited, melt transport network
1767 in the lower crust. Based on these results, we propose an updated conceptual model
1768 for continental flood basalt volcanism.

1769 We find observational constraints from other CFBs, especially the Columbia
1770 River Basalts and Siberian Traps, to support our proposed model. In particular, that
1771 most of the CFBs show similar geochemical variations as the Deccan Traps strongly
1772 suggests a multiple magma reservoir magmatic architecture. Our study provides a
1773 framework to combine various disparate observations with theoretical calculations and
1774 can be used with future measurements for the Deccan Traps and other CFBs to both
1775 test and refine our model. A better understanding of the CFB magmatic architecture
1776 is critical for making quantitative predictions for the rate of volatile release (CO_2 and
1777 SO_2) during eruptions as well as the volume that is passively degassed. These inputs,
1778 along with magma volume flux and duration of individual eruptive episodes, are criti-
1779 cal for quantitatively assessing the environmental consequences of flood basalt events
1780 and comparing with paleo-climate proxy observations (Self et al., 2006; Schmidt et al.,
1781 2016; Glaze et al., 2017; Suarez et al., 2019; Hull et al., 2020).

1782 8 Tables

1783 Table 1: Summary of characteristic timescale for the magma reservoir model and
1784 the thermo-chemical box model.

Timescale	Expression
$t_{Maxwell}$	$\frac{\eta_{cr}\tilde{\beta}_s}{K_{cr}}$
t_{flux}	$\frac{4d_{res}a_c^2 b_c}{ab^3}\frac{\eta_{res}\tilde{\beta}_s}{K_{cr}}$
t_{repres}	$\frac{\pi a_c^2 b_c \tilde{\beta}_s \rho_{res}}{\Omega K_{cr}}$
$t_{R,spherical\ shell}$	$\left[\frac{3\eta_{cr,1}(1-\nu)}{K_{cr}(1+\nu)}\right]\left(\frac{R_2}{R_1}\right)^3$
$t_{R,relax\ compress}$	$t_{R,spherical\ shell}/(1+\beta\alpha)$
$t^c_{viscous}$	$\eta_{crust}/(\Delta P)$
t^c_{fill}	V/Q_0
t^c_{cool}	$\epsilon_0 V\left(\frac{\oint_{res} q(\Delta T)dA}{\rho_{res}L_f} - \frac{Q_0 c_p \Delta T}{L_f}\right)^{-1}$
$t^c_{press\ diff}$	$\frac{b_c^2}{4\kappa_{pd}}$

Table 1: Summary of characteristic timescale for the magma reservoir model and the thermo-chemical box model.

Acknowledgments

T. Mittal acknowledges graduate funding support from the NSF grant EAR #1615203 and the Crosby Postdoc Fellowship at MIT. We thank Paul Renne, Steve Self, Isabel Fendley, Courtney Sprain, Benjamin Black, Michael Manga, Leif Karlstrom, and Loyc Vanderkluysen for useful discussions and suggestions for the manuscript text. We thank (reviewers and editors) for their valuable comments and suggestions. The authors declare that the research was conducted in the absence of any commercial or financial relationships that could be construed as a potential conflict of interest. There is no experimental or observational data associated to this study. Codes for realizing the analytical and semi-analytical solutions can be downloaded from `https://figshare.com/s/aad2f0311d1c596b0d8e`.

References

Aarnes, I., Podladchikov, Y., & Svensen, H. (2012). Devolatilization-induced pressure build-up: Implications for reaction front movement and breccia pipe formation. *Geofluids*, *12*(4), 265–279.

Aharonov, E., Spiegelman, M., & Kelemen, P. (1997). Three-dimensional flow and reaction in porous media: Implications for the earth's mantle and sedimentary basins. *Journal of Geophysical Research: Solid Earth*, *102*(B7), 14821–14833.

Aki, K., & Ferrazzini, V. (2001). Comparison of mount etna, kilauea, and piton de la fournaise by a quantitative modeling of their eruption histories. *Journal of Geophysical Research: Solid Earth*, *106*(B3), 4091–4102.

Albino, F., Biggs, J., & Syahbana, D. K. (2019). Dyke intrusion between neighbouring arc volcanoes responsible for 2017 pre-eruptive seismic swarm at agung. *Nature communications*, *10*(1), 1–11.

Amoruso, A., & Crescentini, L. (2009). Shape and volume change of pressurized ellipsoidal cavities from deformation and seismic data. *Journal of Geophysical Research: Solid Earth*, *114*(B2).

Anderson, A. N., Foster, J. H., & Frazer, N. (2020). Implications of deflation-inflation event models on kilauea volcano, hawai'i. *Journal of Volcanology and Geothermal Research*, 106832.

Anderson, K., & Segall, P. (2011). Physics-based models of ground deformation and extrusion rate at effusively erupting volcanoes. *Journal of Geophysical Research: Solid Earth*, *116*(B7).

Anderson, K. R., & Poland, M. P. (2017). Abundant carbon in the mantle beneath hawai 'i. *Nature Geoscience*, *10*(9), 704–708.

Angkasa, S. S., Jerram, D. A., Millett, J. M., Svensen, H. H., Planke, S., Taylor, R. A., ... Howell, J. (2017). Mafic intrusions, hydrothermal venting, and the basalt-sediment transition: Linking onshore and offshore examples from the north atlantic igneous province. *Interpretation*, *5*(3), SK83–SK101.

Aravena, A., Cioni, R., de' Michieli Vitturi, M., Pistolesi, M., Ripepe, M., & Neri, A. (2018, aug). Evolution of conduit geometry and eruptive parameters during effusive events. *Geophysical Research Letters*, *45*(15), 7471–7480. doi: 10.1029/2018gl077806

Aravena, A., Cioni, R., de' Michieli Vitturi, M., Pistolesi, M., Ripepe, M., & Neri, A. (2018). Evolution of conduit geometry and eruptive parameters during effusive events. *Geophysical Research Letters*, *45*(15), 7471–7480.

Aravena, Á., Cioni, R., Vitturi, M. d., & Neri, A. (2018). Conduit stability effects on intensity and steadiness of explosive eruptions. *Scientific reports*, *8*(1), 1–9.

Bachmann, O., & Bergantz, G. (2008). The magma reservoirs that feed supereruptions. *Elements*, *4*(1), 17–21.

Beane, J., Turner, C., Hooper, P., Subbarao, K., & Walsh, J. (1986). Stratigraphy, composition and form of the deccan basalts, western ghats, india. *Bulletin of Volcanology*, *48*(1), 61–83.

Bédard, J. H., Naslund, H. R., Nabelek, P., Winpenny, A., Hryciuk, M., Macdonald, W., ... others (2012). Fault-mediated melt ascent in a neoproterozoic continental flood basalt province, the franklin sills, victoria island, canada. *Bulletin*, *124*(5-6), 723–736.

Beinlich, A., John, T., Vrijmoed, J. C., Tominaga, M., Magna, T., & Podladchikov, Y. Y. (2020). Instantaneous rock transformations in the deep crust driven by reactive fluid flow. *Nature Geoscience*, *13*(4), 307–311.

Belardinelli, M., Bonafede, M., & Nespoli, M. (2019). Stress heterogeneities and failure mechanisms induced by temperature and pore-pressure increase in volcanic regions. *Earth and Planetary Science Letters*, *525*, 115765.

Bergantz, G., Schleicher, J., & Burgisser, A. (2015). Open-system dynamics and mixing in magma mushes. *Nature Geoscience*, *8*(10), 793–796.

Bertelsen, H. S., Rogers, B. D., Galland, O., Dumazer, G., & Abbana Benanni, A. (2018). Laboratory modeling of coeval brittle and ductile deformation during magma emplacement into viscoelastic rocks. *Frontiers in Earth Science*, *6*, 199.

Biggs, J., & Annen, C. (2019, jan). The lateral growth and coalesence of magma systems. *Philosophical Transactions of the Royal Society A: Mathematical, Physical and Engineering Sciences*, *377*(2139), 20180005. doi: 10.1098/rsta.2018.0005

Black, B. A., & Gibson, S. A. (2019). Deep carbon and the life cycle of large igneous provinces. *Elements: An International Magazine of Mineralogy, Geochemistry, and Petrology*, *15*(5), 319–324.

Black, B. A., & Manga, M. (2017). Volatiles and the tempo of flood basalt magmatism. *Earth and Planetary Science Letters*, *458*, 130–140.

Blanchard, J. A., Ernst, R. E., & Samson, C. (2017). Gravity and magnetic modelling of layered mafic–ultramafic intrusions in large igneous province plume centre regions: case studies from the 1.27 ga mackenzie, 1.38 ga kunene–kibaran, 0.06 ga deccan, and 0.13–0.08 ga high arctic events. *Canadian Journal of Earth Sciences*, *54*(3), 290–310.

Bondre, N. R., & Hart, W. K. (2008). Morphological and textural diversity of the steens basalt lava flows, southeastern oregon, usa: implications for emplacement style and nature of eruptive episodes. *Bulletin of Volcanology*, *70*(8), 999–1019.

Borges, M. R., Sen, G., Hart, G. L., Wolff, J. A., & Chandrasekharam, D. (2014). Plagioclase as recorder of magma chamber processes in the deccan traps: Sr-isotope zoning and implications for deccan eruptive event. *Journal of Asian Earth Sciences*, *84*, 95–101.

Boudoire, G., Rizzo, A. L., Di Muro, A., Grassa, F., & Liuzzo, M. (2018). Extensive co2 degassing in the upper mantle beneath oceanic basaltic volcanoes: First insights from piton de la fournaise volcano (la réunion island). *Geochimica et Cosmochimica Acta*, *235*, 376–401.

Brown, R., Kavanagh, J., Sparks, R., Tait, M., & Field, M. (2007). Mechanically disrupted and chemically weakened zones in segmented dike systems cause vent localization: Evidence from kimberlite volcanic systems. *Geology*, *35*(9), 815–818.

Bruce, P. M., & Huppert, H. E. (1990). Solidification and melting along dykes by the laminar flow of basaltic magma. *Magma transport and storage*, 87–101.

Bryan, S. E., & Ferrari, L. (2013). Large igneous provinces and silicic large igneous provinces: Progress in our understanding over the last 25 years. *GSA Bulletin*, *125*(7-8), 1053–1078.

Bryan, S. E., Peate, I. U., Peate, D. W., Self, S., Jerram, D. A., Mawby, M. R., ... Miller, J. A. (2010). The largest volcanic eruptions on earth. *Earth-Science Reviews*, *102*(3-4), 207–229.

Burgisser, A., Carrara, A., & Annen, C. (2020). Numerical simulations of mag-

matic enclave deformation. *Journal of Volcanology and Geothermal Research*, *392*, 106790.

Bürgmann, R., & Dresen, G. (2008). Rheology of the lower crust and upper mantle: Evidence from rock mechanics, geodesy, and field observations. *Annu. Rev. Earth Planet. Sci.*, *36*, 531–567.

Calogero, M., Hetland, E., & Lange, R. (2020). High-resolution numerical modeling of heat and volatile transfer from basalt to wall rock: Application to the crustal column beneath long valley caldera, ca. *Journal of Geophysical Research: Solid Earth*, *n/a*(n/a), e54059. Retrieved from `https://agupubs.onlinelibrary.wiley.com/doi/abs/10.1029/2018JB016773` (e54059 2018JB016773) doi: 10.1029/2018JB016773

Calvari, S. (2019). Understanding basaltic lava flow morphologies and structures for hazard assessment. *Annals of Geophysics*.

Campbell, I. H., & Griffiths, R. W. (1990). Implications of mantle plume structure for the evolution of flood basalts. *Earth and Planetary Science Letters*, *99*(1-2), 79–93.

Cao, W., Kaus, B. J., & Paterson, S. (2016). Intrusion of granitic magma into the continental crust facilitated by magma pulsing and dike-diapir interactions: Numerical simulations. *Tectonics*, *35*(6), 1575–1594.

Cao, W., Lee, C.-T. A., Yang, J., & Zuza, A. V. (2019, jun). Hydrothermal circulation cools continental crust under exhumation. *Earth and Planetary Science Letters*, *515*, 248–259. doi: 10.1016/j.epsl.2019.03.029

Capriolo, M., Marzoli, A., Aradi, L. E., Callegaro, S., Dal Corso, J., Newton, R. J., ... others (2020). Deep co 2 in the end-triassic central atlantic magmatic province. *Nature communications*, *11*(1), 1–11.

Caricchi, L., Annen, C., Blundy, J., Simpson, G., & Pinel, V. (2014). Frequency and magnitude of volcanic eruptions controlled by magma injection and buoyancy. *Nature Geoscience*, *7*(2), 126.

Caricchi, L., Sheldrake, T. E., & Blundy, J. (2018). Modulation of magmatic processes by co2 flushing. *Earth and Planetary Science Letters*, *491*, 160–171.

Carrara, A., Burgisser, A., & Bergantz, G. W. (2019). Lubrication effects on magmatic mush dynamics. *Journal of Volcanology and Geothermal Research*, *380*, 19–30.

Carrara, A., Burgisser, A., & Bergantz, G. W. (2020). The architecture of an intrusion in magmatic mush.

Cashman, K. V., Sparks, R. S. J., & Blundy, J. D. (2017). Vertically extensive and unstable magmatic systems: a unified view of igneous processes. *Science*, *355*(6331), eaag3055.

Cassidy, M., Manga, M., Cashman, K., & Bachmann, O. (2018). Controls on explosive-effusive volcanic eruption styles. *Nature communications*, *9*(1), 1–16.

Chatterjee, N., & Bhattacharji, S. (2008). Trace element variations in deccan basalts: roles of mantle melting, fractional crystallization and crustal assimilation. *Journal of the Geological Society of India*, *71*(2), 171.

Chatterjee, N., & Sheth, H. (2015). Origin of the powai ankaramite, and the composition, p–t conditions of equilibration and evolution of the primary magmas of the deccan tholeiites. *Contributions to Mineralogy and Petrology*, *169*(3), 32.

Cheng, L., Zeng, L., Ren, Z., Wang, Y., & Luo, Z. (2014). Timescale of emplacement of the panzhihua gabbroic layered intrusion recorded in giant plagioclase at sichuan province, sw china. *Lithos*, *204*, 203–219.

Cheng, L.-L., Yang, Z.-F., Zeng, L., Wang, Y., & Luo, Z.-H. (2014). Giant plagioclase growth during storage of basaltic magma in emeishan large igneous province, sw china. *Contributions to Mineralogy and Petrology*, *167*(2), 971.

Chevrel, M. O., Pinkerton, H., & Harris, A. J. (2019). Measuring the viscosity of lava in the field: A review. *Earth-Science Reviews*.

Choudhary, B. R., Santosh, M., De Vivo, B., Jadhav, G., & Babu, E. (2019). Melt inclusion evidence for mantle heterogeneity and magma degassing in the deccan large igneous province, india. *Lithos*, *346*, 105135.

Clapham, M. E., & Renne, P. R. (2019). Flood basalts and mass extinctions. *Annual Review of Earth and Planetary Sciences*, *47*, 275–303.

Coetzee, A., Kisters, A., & Chevallier, L. (2019). Sill complexes in the karoo lip: Emplacement controls and regional implications. *Journal of African Earth Sciences*, *158*, 103517.

Coetzee, A., & Kisters, A. F. (2018). The elusive feeders of the karoo large igneous province and their structural controls. *Tectonophysics*, *747*, 146–162.

Colón, D. P., Bindeman, I. N., & Gerya, T. V. (2019). Understanding the isotopic and chemical evolution of yellowstone hot spot magmatism using magmatic-thermomechanical modeling. *Journal of Volcanology and Geothermal Research*, *370*, 13–30.

Cooper, K. M. (2015). Timescales of crustal magma reservoir processes : insights from U-series crystal ages. *Chemica, Physical and Temporal Evolution of Magmatic System*. doi: 10.1016/j.gca.2006.06.135

Costa, A., Melnik, O., & Sparks, R. (2007). Controls of conduit geometry and wall-rock elasticity on lava dome eruptions. *Earth and Planetary Science Letters*, *260*(1-2), 137–151.

Courtillot, V., & Fluteau, F. (2014). A review of the embedded time scales of flood basalt volcanism with special emphasis on dramatically short magmatic pulses. *Geological Society of America Special Papers*, *505*, SPE505–15.

Courtillot, V. E., & Renne, P. R. (2003). On the ages of flood basalt events. *Comptes Rendus Geoscience*, *335*(1), 113–140.

Cox, K. (1988). Numerical modelling of a randomized rtf magma chamber: a comparison with continental flood basalt sequences. *Journal of Petrology*, *29*(3), 681–697.

Cox, K. G. (1980). A model for flood basalt volcanism. *Journal of Petrology*, *21*(4), 629–650. doi: 10.1093/petrology/21.4.629

Cruden, A. R., & Weinberg, R. F. (2018). Mechanisms of magma transport and storage in the lower and middle crust—magma segregation, ascent and emplacement. In *Volcanic and igneous plumbing systems* (pp. 13–53). Elsevier.

DeBari, S. M., & Greene, A. R. (2011). Vertical stratification of composition, density, and inferred magmatic processes in exposed arc crustal sections. In *Arc-continent collision* (pp. 121–144). Springer.

Degruyter, W., & Huber, C. (2014). A model for eruption frequency of upper crustal silicic magma chambers. *Earth and Planetary Science Letters*, *403*, 117–130.

de Silva, S. L., & Gregg, P. M. (2014). Thermomechanical feedbacks in magmatic systems: Implications for growth, longevity, and evolution of large caldera-forming magma reservoirs and their supereruptions. *Journal of Volcanology and Geothermal Research*, *282*, 77–91.

Dessai, A., Viegas, A., & Griffin, W. (2020). Thermal architecture of cratonic india and implications for decratonization of the western dharwar craton: Evidence from mantle xenoliths in the deccan traps. *Lithos*, 105927.

Dongre, A., Viljoen, K., & Rathod, A. (2018). Mineralogy and geochemistry of picro-dolerite dykes from the central deccan traps flood basaltic province, india, and their geodynamic significance. *Mineralogy and Petrology*, *112*(2), 267–277.

Dragoni, M., & Magnanensi, C. (1989). Displacement and stress produced by a pressurized, spherical magma chamber, surrounded by a viscoelastic shell. *Physics of the Earth and Planetary Interiors*, *56*(3-4), 316–328.

Dragoni, M., & Santini, S. (2007). Lava flow in tubes with elliptical cross sections. *Journal of volcanology and geothermal research*, *160*(3-4), 239–248.

Dragoni, M., & Tallarico, A. (2018). Changes in lava effusion rate from a volcanic

fissure due to pressure changes in the conduit. *Geophysical Journal International*, *216*(1), 692–702.

Edmonds, M., Cashman, K. V., Holness, M., & Jackson, M. (2019, jan). Architecture and dynamics of magma reservoirs. *Philosophical Transactions of the Royal Society A: Mathematical, Physical and Engineering Sciences*, *377*(2139), 20180298. doi: 10.1098/rsta.2018.0298

Edmonds, M., & Wallace, P. J. (2017). Volatiles and exsolved vapor in volcanic systems. *Elements*, *13*(1), 29–34.

Elliot, D. H., & Fleming, T. H. (2018). The ferrar large igneous province: field and geochemical constraints on supra-crustal (high-level) emplacement of the magmatic system. *Geological Society, London, Special Publications*, *463*(1), 41–58.

Elshaafi, A., & Gudmundsson, A. (2018). Mechanical interaction between volcanic systems in libya. *Tectonophysics*, *722*, 549–565.

Ernst, R. E. (2014). *Large igneous provinces*. Cambridge University Press.

Ernst, R. E., Liikane, D. A., Jowitt, S. M., Buchan, K., & Blanchard, J. (2019). A new plumbing system framework for mantle plume-related continental large igneous provinces and their mafic-ultramafic intrusions. *Journal of Volcanology and Geothermal Research*, *384*, 75–84.

Ernst, R. E., & Youbi, N. (2017). How large igneous provinces affect global climate, sometimes cause mass extinctions, and represent natural markers in the geological record. *Palaeogeography, Palaeoclimatology, Palaeoecology*, *478*, 30–52.

Fainstein, R., Richards, M., & Kalra, R. (2019). Seismic imaging of deccan-related lava flows at the kt boundary, deepwater west india. *The Leading Edge*, *38*(4), 286–290.

Farnetani, C. G., Hofmann, A. W., Duvernay, T., & Limare, A. (2018). Dynamics of rheological heterogeneities in mantle plumes. *Earth and Planetary Science Letters*, *499*, 74–82.

Farnetani, C. G., & Richards, M. A. (1994). Numerical investigations of the mantle plume initiation model for flood basalt events. *Journal of Geophysical Research: Solid Earth*, *99*(B7), 13813–13833.

Fendley, I. M., Mittal, T., Sprain, C. J., Marvin-DiPasquale, M., Tobin, T. S., & Renne, P. R. (2019). Constraints on the volume and rate of deccan traps flood basalt eruptions using a combination of high-resolution terrestrial mercury records and geochemical box models. *Earth and Planetary Science Letters*, *524*, 115721.

Fendley, I. M., Sprain, C. J., Renne, P. R., Arenillas, I., Arz, J. A., Gilabert, V., ... others (2020). No cretaceous-paleogene boundary in exposed rajahmundry traps: A refined chronology of the longest deccan lava flows from 40ar/39ar dates, magnetostratigraphy, and biostratigraphy. *Geochemistry, Geophysics, Geosystems*, *21*(9), e2020GC009149.

Fialko, Y. A., & Rubin, A. M. (1999). Thermal and mechanical aspects of magma emplacement in giant dike swarms. *Journal of Geophysical Research: Solid Earth*, *104*(B10), 23033–23049. doi: 10.1029/1999JB900213

Fitton, J. G., & Godard, M. (2004). Origin and evolution of magmas on the ontong java plateau. *Geological Society, London, Special Publications*, *229*(1), 151–178.

Francois, T., Koptev, A., Cloetingh, S., Burov, E., & Gerya, T. (2018). Plume-lithosphere interactions in rifted margin tectonic settings: Inferences from thermo-mechanical modelling. *Tectonophysics*, *746*, 138–154.

Galland, O., Spacapan, J. B., Rabbel, O., Mair, K., Soto, F. G., Eiken, T., ... Leanza, H. A. (2019). Structure, emplacement mechanism and magma-flow significance of igneous fingers–implications for sill emplacement in sedimentary basins. *Journal of Structural Geology*, *124*, 120–135.

Geldmacher, J., van den Bogaard, P., Heydolph, K., & Hoernle, K. (2014, nov). The age of Earth's largest volcano: Tamu Massif on Shatsky Rise (northwest Pacific Ocean). *International Journal of Earth Sciences*, *103*(8), 2351–2357. doi: 10.1007/s00531-014-1078-6

Gibson, S. A., Rooks, E. E., Day, J. A., Petrone, C. M., & Leat, P. T. (2020). The role of sub-continental mantle as both "sink" and "source" in deep earth volatile cycles. *Geochimica et Cosmochimica Acta*. doi: https://doi.org/10.1016/j.gca.2020.02.018

Glaze, L. S., Self, S., Schmidt, A., & Hunter, S. J. (2017). Assessing eruption column height in ancient flood basalt eruptions. *Earth and Planetary Science Letters*, *457*, 263–270.

Gleeson, M., Gibson, S. A., & Stock, M. J. (2020). Upper mantle mush zones beneath low melt flux ocean island volcanoes: insights from isla floreana, galápagos.

Gonnermann, H., & Manga, M. (2012). *Dynamics of magma ascent in the volcanic conduit, modeling volcanic processes: The physics and mathematics of volcanism, eds. sarah a. fagents, tracy kp gregg, and rosaly mc lopes.* Cambridge University Press.

Gonnermann, H. M. (2015). Magma fragmentation. *Annual Review of Earth and Planetary Sciences*, *43*, 431–458.

Gu, X.-Y., Wang, P.-Y., Kuritani, T., Hanski, E., Xia, Q.-K., & Wang, Q.-Y. (2019). Low water content in the mantle source of the hainan plume as a factor inhibiting the formation of a large igneous province. *Earth and Planetary Science Letters*, *515*, 221–230.

Gudmundsson, A. (2002). Emplacement and arrest of sheets and dykes in central volcanoes. *Journal of Volcanology and Geothermal Research*, *116*(3-4), 279–298.

Gudmundsson, A. (2016). The mechanics of large volcanic eruptions. *Earth-science reviews*, *163*, 72–93.

Halbach, H., & Chatterjee, N. D. (1982). An empirical redlich-kwong-type equation of state for water to 1,000 c and 200 kbar. *Contributions to Mineralogy and Petrology*, *79*(3), 337–345.

Harris, A. J., Dehn, J., & Calvari, S. (2007). Lava effusion rate definition and measurement: a review. *Bulletin of Volcanology*, *70*(1), 1.

Haug, Ø., Galland, O., Souloumiac, P., Souche, A., Guldstrand, F., Schmiedel, T., & Maillot, B. (2018). Shear versus tensile failure mechanisms induced by sill intrusions: Implications for emplacement of conical and saucer-shaped intrusions. *Journal of Geophysical Research: Solid Earth*, *123*(5), 3430–3449.

Hauri, E. H., Gaetani, G. A., & Green, T. H. (2006). Partitioning of water during melting of the earth's upper mantle at h2o-undersaturated conditions. *Earth and Planetary Science Letters*, *248*(3-4), 715–734.

Havlin, C., Parmentier, E., & Hirth, G. (2013, aug). Dike propagation driven by melt accumulation at the lithosphere–asthenosphere boundary. *Earth and Planetary Science Letters*, *376*, 20–28. doi: 10.1016/j.epsl.2013.06.010

Heinonen, J. S., Luttinen, A. V., Spera, F. J., & Bohrson, W. A. (2019). Deep open storage and shallow closed transport system for a continental flood basalt sequence revealed with magma chamber simulator. *Contributions to Mineralogy and Petrology*, *174*(11), 87.

Hepworth, L. N., Daly, J. S., Gertisser, R., Johnson, C. G., Emeleus, C. H., & O'Driscoll, B. (2020). Rapid crystallization of precious-metal-mineralized layers in mafic magmatic systems. *Nature Geoscience*, *13*(5), 375–381.

Hieronymus, C. F., & Bercovici, D. (2001). A theoretical model of hotspot volcanism: Control on volcanic spacing and patterns via magma dynamics and lithospheric stresses. *Journal of Geophysical Research-Solid Earth*, *106*, 683–702. doi: 10.1029/2000JB900355

Higgins, M. D., & Chandrasekharam, D. (2007). Nature of sub-volcanic magma chambers, deccan province, india: evidence from quantitative textural analysis of plagioclase megacrysts in the giant plagioclase basalts. *Journal of Petrology*, *48*(5), 885–900.

Hildreth, W., & Wilson, C. J. (2007). Compositional zoning of the bishop tuff. *Journal of Petrology*, *48*(5), 951–999.

Hochmuth, K., Gohl, K., & Uenzelmann-Neben, G. (2015). *Playing jigsaw with Large Igneous Provinces-A plate tectonic reconstruction of Ontong Java Nui, West Pacific.* doi: 10.1002/2015GC006036

Hon, K., Kauahikaua, J., Denlinger, R., & Mackay, K. (1994). Emplacement and inflation of pahoehoe sheet flows: Observations and measurements of active lava flows on kilauea volcano, hawaii. *Geological Society of America Bulletin*, *106*(3), 351–370.

Hooper, P., Widdowson, M., & Kelley, S. (2010). Tectonic setting and timing of the final deccan flood basalt eruptions. *Geology*, *38*(9), 839–842.

Hull, P. M., Bornemann, A., Penman, D. E., Henehan, M. J., Norris, R. D., Wilson, P. A., ... others (2020). On impact and volcanism across the cretaceous-paleogene boundary. *Science*, *367*(6475), 266–272.

Huppert, H. E., & Woods, A. W. (2002). The role of volatiles in magma chamber dynamics. *Nature*, *420*(6915), 493–495.

Iacono-Marziano, G., Morizet, Y., Le Trong, E., & Gaillard, F. (2012). New experimental data and semi-empirical parameterization of h2o–co2 solubility in mafic melts. *Geochimica et Cosmochimica Acta*, *97*, 1–23.

Ingebritsen, S., & Gleeson, T. (2017). Crustal permeability. *Hydrogeology Journal*, *25*(8), 2221–2224.

Ingebritsen, S., & Manning, C. E. (2010). Permeability of the continental crust: dynamic variations inferred from seismicity and metamorphism. *Geofluids*, *10*(1-2), 193–205.

Ivanov, A. V., Mukasa, S. B., Kamenetsky, V. S., Ackerson, M., Demonterova, E. I., Pokrovsky, B. G., ... Zedgenizov, D. A. (2018). Volatile concentrations in olivine-hosted melt inclusions from meimechite and melanephelinite lavas of the siberian traps large igneous province: Evidence for flux-related high-ti, high-mg magmatism. *Chemical Geology*, *483*, 442–462.

Jay, A. E., Mac Niocaill, C., Widdowson, M., Self, S., & Turner, W. (2009). New palaeomagnetic data from the mahabaleshwar plateau, deccan flood basalt province, india: implications for the volcanostratigraphic architecture of continental flood basalt provinces. *Journal of the Geological Society*, *166*(1), 13–24.

Jennings, S., Hasterok, D., & Payne, J. (2019). A new compositionally based thermal conductivity model for plutonic rocks. *Geophysical Journal International*, *219*(2), 1377–1394.

Jerram, D. A., Dobson, K. J., Morgan, D. J., & Pankhurst, M. J. (2018). The petrogenesis of magmatic systems: Using igneous textures to understand magmatic processes. In *Volcanic and igneous plumbing systems* (pp. 191–229). Elsevier.

Jerram, D. A., & Widdowson, M. (2005). The anatomy of continental flood basalt provinces: geological constraints on the processes and products of flood volcanism. *Lithos*, *79*(3-4), 385–405.

Jones, M. T., Jerram, D. A., Svensen, H. H., & Grove, C. (2016). The effects of large igneous provinces on the global carbon and sulphur cycles. *Palaeogeography, Palaeoclimatology, Palaeoecology*, *441*, 4–21.

Karakas, O., Degruyter, W., Bachmann, O., & Dufek, J. (2017). Lifetime and size of shallow magma bodies controlled by crustal-scale magmatism. *Nature Geoscience*, *10*(6), 446–450.

Karakas, O., & Dufek, J. (2015). Melt evolution and residence in extending crust: Thermal modeling of the crust and crustal magmas. *Earth and Planetary Sci-*

ence Letters, *425*, 131–144. doi: 10.1016/j.epsl.2015.06.001

Karlstrom, L., Dufek, J., & Manga, M. (2009). Organization of volcanic plumbing through magmatic lensing by magma chambers and volcanic loads. *Journal of Geophysical Research: Solid Earth*, *114*(B10).

Karlstrom, L., & Manga, M. (2009, 12). Magma siphoning and the mechanics of large igneous province eruptions. *AGU Fall Meeting Abstracts*.

Karlstrom, L., Paterson, S. R., & Jellinek, A. M. (2017). A reverse energy cascade for crustal magma transport. *Nature Geoscience*, *10*(8), 604.

Karlstrom, L., & Richards, M. (2011). On the evolution of large ultramafic magma chambers and timescales for flood basalt eruptions. *Journal of Geophysical Research: Solid Earth*, *116*(B8).

Karlstrom, L., Richardson, P. W., O'Hara, D., & Ebmeier, S. K. (2018). Magmatic landscape construction. *Journal of Geophysical Research: Earth Surface*, *123*(8), 1710–1730.

Karlstrom, L., Rudolph, M. L., & Manga, M. (2012). Caldera size modulated by the yield stress within a crystal-rich magma reservoir. *Nature Geoscience*, *5*(6), 402–405.

Karlstrom, L., Wright, H. M., & Bacon, C. R. (2015). The effect of pressurized magma chamber growth on melt migration and pre-caldera vent locations through time at Mount Mazama, Crater Lake, Oregon. *Earth and Planetary Science Letters*, *412*, 209–219. doi: 10.1016/j.epsl.2014.12.001

Katz, R. F., Spiegelman, M., & Holtzman, B. (2006). The dynamics of melt and shear localization in partially molten aggregates. *Nature*, *442*(7103), 676–9. doi: 10.1038/nature05039

Katz, R. F., Spiegelman, M., & Langmuir, C. H. (2003). A new parameterization of hydrous mantle melting. *Geochemistry, Geophysics, Geosystems*, *4*(9).

Keller, T., May, D. A., & Kaus, B. J. P. (2013). Numerical modelling of magma dynamics coupled to tectonic deformation of lithosphere and crust. *Geophysical Journal International*, *195*(3), 1406–1442. doi: 10.1093/gji/ggt306

Kerr, A. C., Tarney, J., Marriner, G. F., Nivia, A., & Saunders, A. D. (1997). The Caribbean-Colombian Cretaceous Igneous Province: The internal anatomy of an oceanic plateau. *Geophysical Monograph*, *100*, 123–144. doi: 10.1029/GM100p0123

Kiss, D., Podladchikov, Y., Duretz, T., & Schmalholz, S. M. (2019, aug). Spontaneous generation of ductile shear zones by thermal softening: Localization criterion, 1d to 3d modelling and application to the lithosphere. *Earth and Planetary Science Letters*, *519*, 284–296. doi: 10.1016/j.epsl.2019.05.026

Kjøll, H. J., Galland, O., Labrousse, L., & Andersen, T. B. (2019, jul). Emplacement mechanisms of a dyke swarm across the brittle-ductile transition and the geodynamic implications for magma-rich margins. *Earth and Planetary Science Letters*, *518*, 223–235. doi: 10.1016/j.epsl.2019.04.016

Koptev, A., Burov, E., Gerya, T., Le Pourhiet, L., Leroy, S., Calais, E., & Jolivet, L. (2018). Plume-induced continental rifting and break-up in ultra-slow extension context: Insights from 3d numerical modeling. *Tectonophysics*, *746*, 121–137.

Korchinski, M., Rey, P. F., Mondy, L., Teyssier, C., & Whitney, D. L. (2018). Numerical investigation of deep-crust behavior under lithospheric extension. *Tectonophysics*, *726*, 137–146.

Krans, S. R., Rooney, T. O., Kappelman, J., Yirgu, G., & Ayalew, D. (2018, apr). From initiation to termination: a petrostratigraphic tour of the ethiopian low-ti flood basalt province. *Contributions to Mineralogy and Petrology*, *173*(5). doi: 10.1007/s00410-018-1460-7

Krishnamurthy, P. (2019). Giant plagioclase basalts (gpbs) from the deccan volcanic province (dvp) and the deccan volcanic cycle (dvc), india. *Journal of the Geological Society of India*, *94*(3), 223–226.

Kumar, K. V., Laxman, M. B., & Nagaraju, K. (2018). Mantle source heterogeneity

in continental mafic large igneous provinces: insights from the panjal, rajmahal and deccan basalts, india. *Geological Society, London, Special Publications*, *463*(1), 87–116.

Kumar, N., Zeyen, H., Singh, A., & Singh, B. (2013). Lithospheric structure of southern indian shield and adjoining oceans: integrated modelling of topography, gravity, geoid and heat flow data. *Geophysical Journal International*, *194*(1), 30–44.

Lamy-Chappuis, B., Heinrich, C. A., Driesner, T., & Weis, P. (2020). Mechanisms and patterns of magmatic fluid transport in cooling hydrous intrusions. *Earth and Planetary Science Letters*, *535*, 116111.

Lange, R. A. (2002). Constraints on the preeruptive volatile concentrations in the columbia river flood basalts. *Geology*, *30*(2), 179–182.

Langtangen, H., & Linge, S. (2017). *Finite difference computing with pdes, texts in computational science and engineering.* Springer International Publishing, Cham. https://doi. org/10.1007/978-3-319 ....

Larsen, R. B., Grant, T., Sørensen, B. E., Tegner, C., McEnroe, S., Pastore, Z., ... others (2018). Portrait of a giant deep-seated magmatic conduit system: The seiland igneous province. *Lithos*, *296*, 600–622.

Latyshev, A., Veselovskiy, R., & Ivanov, A. (2018, jan). Paleomagnetism of the permian-triassic intrusions from the tunguska syncline and the angara-taseeva depression, siberian traps large igneous province: Evidence of contrasting styles of magmatism. *Tectonophysics*, *723*, 41–55. doi: 10.1016/j.tecto.2017.11.035

Lavecchia, A., Beekman, F., Clark, S. R., & Cloetingh, S. A. (2016). Thermo-rheological aspects of crustal evolution during continental breakup and melt intrusion: The main ethiopian rift, east africa. *Tectonophysics*, *686*, 51–62.

Lavecchia, A., Clark, S. R., Beekman, F., Cloetingh, S. A., & Burov, E. (2016). Thermal perturbation, mineral assemblages, and rheology variations induced by dyke emplacement in the crust. *Tectonics*, *35*(5), 1137–1152.

Leat, P. T. (2008). On the long-distance transport of ferrar magmas. *Geological Society, London, Special Publications*, *302*(1), 45–61.

Lee, A. L., Lloyd, G. E., Torvela, T., & Walker, A. M. (2020). Evolution of a shear zone before, during and after melting. *Journal of the Geological Society*.

Liao, Y., Soule, S. A., & Jones, M. (2018). On the mechanical effects of poroelastic crystal mush in classical magma chamber models. *Journal of Geophysical Research: Solid Earth*, *123*(11), 9376–9406.

Liu, J., Xia, Q.-K., Kuritani, T., Hanski, E., & Yu, H.-R. (2017). Mantle hydration and the role of water in the generation of large igneous provinces. *Nature communications*, *8*(1), 1–8.

Magee, C., Ernst, R. E., Muirhead, J., Phillips, T., & Jackson, C. A.-L. (2019). Magma transport pathways in large igneous provinces: Lessons from combining field observations and seismic reflection data. In *Dyke swarms of the world: A modern perspective* (pp. 45–85). Springer.

Magee, C., Muirhead, J., Schofield, N., Walker, R. J., Galland, O., Holford, S., ... McCarthy, W. (2019). Structural signatures of igneous sheet intrusion propagation. *Journal of Structural Geology*, *125*, 148–154.

Magee, C., Muirhead, J. D., Karvelas, A., Holford, S. P., Jackson, C. A., Bastow, I. D., ... others (2016). Lateral magma flow in mafic sill complexes. *Geosphere*, *12*(3), 809–841.

Magee, C., O'Driscoll, B., Petronis, M., & Stevenson, C. (2016, apr). Three-dimensional magma flow dynamics within subvolcanic sheet intrusions. *Geosphere*, *12*(3), 842–866. doi: 10.1130/ges01270.1

Magee, C., Stevenson, C. T., Ebmeier, S. K., Keir, D., Hammond, J. O., Gottsmann, J. H., ... others (2018). Magma plumbing systems: a geophysical perspective. *Journal of Petrology*, *59*(6), 1217–1251.

Mahoney, J. J. (1988). Deccan traps. In *Continental flood basalts* (pp. 151–194). Springer.

Mahoney, J. J., & Coffin, M. F. (1997). *Large igneous provinces: continental, oceanic, and planetary flood volcanism* (Vol. 100). American Geophysical Union.

Mancktelow, N. S., & Pennacchioni, G. (2005). The control of precursor brittle fracture and fluid–rock interaction on the development of single and paired ductile shear zones. *Journal of Structural Geology*, *27*(4), 645–661.

Mangan, M., Marsh, B., Froelich, A., & Gottfried, D. (1993). Emplacement and differentiation of the york haven diabase sheet, pennsylvania. *Journal of Petrology*, *34*, 1271–1302.

Marsh, B. D. (1989). Magma chambers. *Annual Review of Earth and Planetary Sciences*, *17*(1), 439–472.

Marsh, B. D. (1996). Solidification fronts and magmatic evolution. *Mineralogical Magazine*, *60*(398), 5–40.

Marsh, B. D. (2002). On bimodal differentiation by solidification front instability in basaltic magmas, part 1: basic mechanics. *Geochimica et Cosmochimica Acta*, *66*(12), 2211–2229.

Marsh, B. D. (2004). A magmatic mush column rosetta stone: the mcmurdo dry valleys of antarctica. *Eos, Transactions American Geophysical Union*, *85*(47), 497–502.

Marsh, B. D. (2013, aug). On some fundamentals of igneous petrology. *Contributions to Mineralogy and Petrology*, *166*(3), 665–690. doi: 10.1007/s00410-013-0892-3

Marsh, B. D., & Coleman, N. M. (2009). Magma flow and interaction with waste packages in a geologic repository at yucca mountain, nevada. *Journal of volcanology and geothermal research*, *182*(1-2), 76–96.

Matthews, S., Shorttle, O., Maclennan, J., & Rudge, J. F. (2020). The global melt inclusion c/ba array: mantle variability, melting process, or degassing? *Geochimica Et Cosmochimica Acta*.

Maurya, S., Montagner, J.-P., Kumar, M. R., Stutzmann, E., Kiselev, S., Burgos, G., ... Srinagesh, D. (2016, oct). Imaging the lithospheric structure beneath the indian continent. *Journal of Geophysical Research: Solid Earth*, *121*(10), 7450–7468. doi: 10.1002/2016jb012948

McGovern, P. J., Grosfils, E. B., Galgana, G. A., Morgan, J. K., Rumpf, M. E., Smith, J. R., & Zimbelman, J. R. (2015, jan). Lithospheric flexure and volcano basal boundary conditions: keys to the structural evolution of large volcanic edifices on the terrestrial planets. *Geological Society, London, Special Publications*, *401*(1), 219–237. doi: 10.1144/SP401.7

Mindaleva, D., Uno, M., Higashino, F., Nagaya, T., Okamoto, A., & Tsuchiya, N. (2020). Rapid fluid infiltration and permeability enhancement during middle–lower crustal fracturing: Evidence from amphibolite–granulite-facies fluid–rock reaction zones, sør rondane mountains, east antarctica. *Lithos*, 105521.

Mittal, T., & Richards, M. A. (2019). Volatile degassing from magma chambers as a control on volcanic eruptions. *Journal of Geophysical Research: Solid Earth*.

Montagna, C., Papale, P., & Longo, A. (2015). Timescales of mingling in shallow magmatic reservoirs. *Geological Society, London, Special Publications*, *422*(1), 131–140.

Montési, L. G. (2013). Fabric development as the key for forming ductile shear zones and enabling plate tectonics. *Journal of Structural Geology*, *50*, 254–266.

Moons, P., & Spencer, D. (1988). Field theory handbook: including coordinate systems, differential equations, and their solutions. *Eleven Coordinate Systems*, 1–48.

Muirhead, J. D., Airoldi, G., Rowland, J. V., & White, J. D. (2012). Interconnected sills and inclined sheet intrusions control shallow magma transport in

the ferrar large igneous province, antarctica. *Bulletin*, *124*(1-2), 162–180.

Muirhead, J. D., Airoldi, G., White, J. D., & Rowland, J. V. (2014). Cracking the lid: Sill-fed dikes are the likely feeders of flood basalt eruptions. *Earth and Planetary Science Letters*, *406*, 187–197.

Neal, C. A., Brantley, S., Antolik, L., Babb, J., Burgess, M., Calles, K., ... others (2019). The 2018 rift eruption and summit collapse of kilauea volcano. *Science*, *363*(6425), 367–374.

Neal, C. R., Coffin, M. F., & Sager, W. W. (2019). Contributions of scientific ocean drilling to understanding the emplacement of submarine large igneous provinces and their effects on the environment. *Oceanography*, *32*(1), 176–192.

Neave, D. A., Buisman, I., & Maclennan, J. (2017). Continuous mush disaggregation during the long-lasting laki fissure eruption, iceland. *American Mineralogist: Journal of Earth and Planetary Materials*, *102*(10), 2007–2021.

O'Hara, D., Karlstrom, L., & Roering, J. J. (2019). Distributed landscape response to localized uplift and the fragility of steady states. *Earth and Planetary Science Letters*, *506*, 243–254.

Óskarsson, B. V., Andersen, C. B., Riishuus, M. S., Sørensen, E. V., & Tegner, C. (2017). The mode of emplacement of neogene flood basalts in eastern iceland: The plagioclase ultraphyric basalts in the grænavatn group. *Journal of Volcanology and Geothermal Research*, *332*, 26–50.

Papale, P., Montagna, C. P., & Longo, A. (2017). Pressure evolution in shallow magma chambers upon buoyancy-driven replenishment. *Geochemistry, Geophysics, Geosystems*, *18*(3), 1214–1224.

Parcheta, C., Fagents, S., Swanson, D. A., Houghton, B. F., & Ericksen, T. (2015). Hawaiian fissure fountains: quantifying vent and shallow conduit geometry, episode 1 of the 1969–1974 mauna ulu eruption. *Hawaiian Volcanoes: From Source to Surface: American Geophysical Union Geophysical Monograph*, *208*, 369–391.

Parks, M. M., Heimisson, E. R., Sigmundsson, F., Hooper, A., Vogfjörd, K. S., Árnadóttir, T., ... others (2017). Evolution of deformation and stress changes during the caldera collapse and dyking at bárdarbunga, 2014–2015: Implication for triggering of seismicity at nearby tungnafellsjökull volcano. *Earth and Planetary Science Letters*, *462*, 212–223.

Parmigiani, A., Faroughi, S., Huber, C., Bachmann, O., & Su, Y. (2016). Bubble accumulation and its role in the evolution of magma reservoirs in the upper crust. *Nature*, *532*(7600), 492.

Passmore, E., Maclennan, J., Fitton, G., & Thordarson, T. (2012, sep). Mush disaggregation in basaltic magma chambers: Evidence from the ad 1783 laki eruption. *Journal of Petrology*, *53*(12), 2593–2623. doi: 10.1093/petrology/egs061

Patrick, M., Dietterich, H., Lyons, J., Diefenbach, A., Parcheta, C., Anderson, K., ... Kauahikaua, J. (2019). Cyclic lava effusion during the 2018 eruption of kīlauea volcano. *Science*, *366*(6470).

Pedersen, G., Höskuldsson, A., Dürig, T., Thordarson, T., Jonsdottir, I., Riishuus, M. S., ... others (2017). Lava field evolution and emplacement dynamics of the 2014–2015 basaltic fissure eruption at holuhraun, iceland. *Journal of Volcanology and Geothermal Research*, *340*, 155–169.

Pietsch, R., & Uenzelmann-Neben, G. (2015). The manihiki plateau—a multistage volcanic emplacement history. *Geochemistry, Geophysics, Geosystems*, *16*(8), 2480–2498.

Piombo, A., Tallarico, A., & Dragoni, M. (2016). Role of mechanical erosion in controlling the effusion rate of basaltic eruptions. *Geophysical Research Letters*, *43*(17), 8970–8977.

Pollard, D. D., Muller, O. H., & Dockstader, D. R. (1975). The form and growth of fingered sheet intrusions. *Bulletin of the Geological Society of America*, *86*(3), 351–363.

Pollard, D. D., & Segall, P. (1987). Theoretical displacements and stresses near fractures in rock: with applications to faults, joints, veins, dikes, and solution surfaces. In *Fracture mechanics of rock* (pp. 277–347).

Potter, K. E., Shervais, J. W., Christiansen, E. H., & Vetter, S. K. (2018). Evidence for cyclical fractional crystallization, recharge, and assimilation in basalts of the kimama drill core, central snake river plain, idaho: 5.5-million-years of petrogenesis in a mid-crustal sill complex. *Frontiers in Earth Science*, *6*, 10.

Rader, E., Vanderkluysen, L., & Clarke, A. (2017). The role of unsteady effusion rates on inflation in long-lived lava flow fields. *Earth and Planetary Science Letters*, *477*, 73–83.

Ray, A., Hatui, K., Paul, D. K., Sen, G., Biswas, S., & Das, B. (2016, feb). Mantle xenolith-xenocryst-bearing monogenetic alkali basaltic lava field from kutch basin, gujarat, western india: Estimation of magma ascent rate. *Journal of Volcanology and Geothermal Research*, *312*, 40–52. doi: 10.1016/j.jvolgeores.2016.01.015

Reekie, C., Jenner, F. E., Smythe, D., Hauri, E., Bullock, E., & Williams, H. (2019). Sulfide resorption during crustal ascent and degassing of oceanic plateau basalts. *Nature communications*, *10*(1), 1–11.

Richards, M., Contreras-Reyes, E., Lithgow-Bertelloni, C., Ghiorso, M., & Stixrude, L. (2013). Petrological interpretation of deep crustal intrusive bodies beneath oceanic hotspot provinces. *Geochemistry, Geophysics, Geosystems*, *14*(3), 604–619. doi: 10.1029/2012GC004448

Richards, M. A., Alvarez, W., Self, S., Karlstrom, L., Renne, P. R., Manga, M., ... Gibson, S. A. (2015). Triggering of the largest Deccan eruptions by the Chicxulub impact. *Bulletin of the Geological Society of America*, *127*(11-12), 1507–1520. doi: 10.1130/B31167.1

Richards, M. A., Duncan, R. A., & Courtillot, V. E. (1989). Flood basalts and hot-spot tracks: plume heads and tails. *Science*, *246*(4926), 103–107.

Richardson, P., & Karlstrom, L. (2019). The multi-scale influence of topography on lava flow morphology. *Bulletin of Volcanology*, *81*(4), 21.

Rivalta, E. (2010). Evidence that coupling to magma chambers controls the volume history and velocity of laterally propagating intrusions. *Journal of Geophysical Research: Solid Earth*, *115*(B7).

Rivalta, E., & Segall, P. (2008). Magma compressibility and the missing source for some dike intrusions. *Geophysical Research Letters*, *35*(4).

Rohrbach, A., & Schmidt, M. W. (2011). Redox freezing and melting in the earth's deep mantle resulting from carbon–iron redox coupling. *Nature*, *472*(7342), 209–212.

Roland, E., Behn, M. D., & Hirth, G. (2010). Thermal-mechanical behavior of oceanic transform faults: Implications for the spatial distribution of seismicity. *Geochemistry, Geophysics, Geosystems*, *11*(7). doi: 10.1029/2010GC003034

Rooney, T. O., Bastow, I. D., Keir, D., Mazzarini, F., Movsesian, E., Grosfils, E. B., ... Yirgu, G. (2014, jun). The protracted development of focused magmatic intrusion during continental rifting. *Tectonics*, *33*(6), 875–897. doi: 10.1002/2013TC003514

Rubin, A. M. (1995). Propagation of magma-filled cracks. *Annual Review of Earth and Planetary Sciences*, *23*(1), 287–336.

Rummel, L., Kaus, B. J., White, R. W., Mertz, D. F., Yang, J., & Baumann, T. S. (2018). Coupled petrological-geodynamical modeling of a compositionally heterogeneous mantle plume. *Tectonophysics*, *723*, 242–260.

Sager, W. W., Huang, Y., Tominaga, M., Greene, J. A., Nakanishi, M., & Zhang, J. (2019). Oceanic plateau formation by seafloor spreading implied by tamu massif magnetic anomalies. *Nature Geoscience*, *12*(8), 661–666.

Saunders, A., Jones, S., Morgan, L., Pierce, K., Widdowson, M., & Xu, Y. (2007). Regional uplift associated with continental large igneous provinces: the roles of

mantle plumes and the lithosphere. *Chemical Geology*, *241*(3-4), 282–318.
Scheibert, J., Galland, O., & Hafver, A. (2017). Inelastic deformation during sill and laccolith emplacement: Insights from an analytic elastoplastic model. *Journal of Geophysical Research: Solid Earth*, *122*(2), 923–945.
Schmeling, H., Marquart, G., & Grebe, M. (2018). A porous flow approach to model thermal non-equilibrium applicable to melt migration. *Geophysical Journal International*, *212*(1), 119–138.
Schmeling, H., Marquart, G., Weinberg, R., & Wallner, H. (2019, jan). Modelling melting and melt segregation by two-phase flow: new insights into the dynamics of magmatic systems in the continental crust. *Geophysical Journal International*, *217*(1), 422–450. doi: 10.1093/gji/ggz029
Schmidt, A., Skeffington, R. A., Thordarson, T., Self, S., Forster, P. M., Rap, A., ... others (2016). Selective environmental stress from sulphur emitted by continental flood basalt eruptions. *Nature Geoscience*, *9*(1), 77–82.
Schoene, B., Eddy, M. P., Samperton, K. M., Keller, C. B., Keller, G., Adatte, T., & Khadri, S. F. (2019). U-pb constraints on pulsed eruption of the deccan traps across the end-cretaceous mass extinction. *Science*, *363*(6429), 862–866.
Schofield, N., Brown, D. J., Magee, C., & Stevenson, C. T. (2012). Sill morphology and comparison of brittle and non-brittle emplacement mechanisms. *Journal of Structural Geology*, *169*(Baer 1995), 127–141. doi: 10.1144/0016-76492011-078 .Sill
Schofield, N., Holford, S., Millett, J., Brown, D., Jolley, D., Passey, S. R., ... others (2017). Regional magma plumbing and emplacement mechanisms of the faroe-shetland sill complex: implications for magma transport and petroleum systems within sedimentary basins. *Basin Research*, *29*(1), 41–63.
Segall, P. (2016). Repressurization following eruption from a magma chamber with a viscoelastic aureole. *Journal of Geophysical Research: Solid Earth*, *121*(12), 8501–8522.
Segall, P. (2019). Magma chambers: what we can, and cannot, learn from volcano geodesy. *Philosophical Transactions of the Royal Society A*, *377*(2139), 20180158.
Self, S., Jay, A. E., Widdowson, M., & Keszthelyi, L. P. (2008). Correlation of the deccan and rajahmundry trap lavas: Are these the longest and largest lava flows on earth? *Journal of Volcanology and Geothermal Research*, *172*(1-2), 3–19.
Self, S., Keszthelyi, L., & Thordarson, T. (1998). The importance of pāhoehoe. *Annual Review of Earth and Planetary Sciences*, *26*(1), 81–110.
Self, S., Schmidt, A., & Mather, T. (2014). Emplacement characteristics, time scales, and volcanic gas release rates of continental flood basalt eruptions on earth. *Geological Society of America Special Papers*, *505*.
Self, S., Widdowson, M., Thordarson, T., & Jay, A. E. (2006). Volatile fluxes during flood basalt eruptions and potential effects on the global environment: A Deccan perspective. *Earth and Planetary Science Letters*, *248*(1-2), 517–531. doi: 10.1016/j.epsl.2006.05.041
Sen, G. (2001). Generation of deccan trap magmas. *Journal of Earth System Science*, *110*(4), 409–431.
Sen, G., & Chandrasekharam, D. (2011). Deccan traps flood basalt province: An evaluation of the thermochemical plume model. In *Topics in igneous petrology* (pp. 29–53). Springer.
Seropian, G., Rust, A., & Sparks, R. (2018). The gravitational stability of lenses in magma mushes: Confined rayleigh-taylor instabilities. *Journal of Geophysical Research: Solid Earth*, *123*(5), 3593–3607.
Shervais, J. W., Vetter, S. K., & Hanan, B. B. (2006). Layered mafic sill complex beneath the eastern snake river plain: Evidence from cyclic geochemical variations in basalt. *Geology*, *34*(5), 365–368.

Sheth, H. (2016). Giant plagioclase basalts: Continental flood basalt–induced remobilization of anorthositic mushes in a deep crustal sill complex. *Bulletin*, *128*(5-6), 916–925.

Sheth, H. C., & Cañón-Tapia, E. (2015). Are flood basalt eruptions monogenetic or polygenetic? *International Journal of Earth Sciences*, *104*(8), 2147–2162.

Snyder, D., & Tait, S. (1995). Replenishment of magma chambers: comparison of fluid-mechanic experiments with field relations. *Contributions to Mineralogy and Petrology*, *122*(3), 230–240. doi: 10.1007/s004100050123

Solano, J. M. S., Jackson, M. D., Sparks, R. S. J., Blundy, J. D., & Annen, C. (2012). Melt segregation in deep crustal hot zones: A mechanism for chemical differentiation, crustal assimilation and the formation of evolved magmas. *Journal of Petrology*, *53*(10), 1999–2026. doi: 10.1093/petrology/egs041

Sørensen, B. E., Grant, T., Ryan, E. J., & Larsen, R. B. (2019). In situ evidence of earthquakes near the crust mantle boundary initiated by mantle co2 fluxing and reaction-driven strain softening. *Earth and Planetary Science Letters*, *524*, 115713.

Sparks, R., Annen, C., Blundy, J., Cashman, K., Rust, A., & Jackson, M. (2019). Formation and dynamics of magma reservoirs. *Philosophical Transactions of the Royal society A*, *377*(2139), 20180019.

Sprain, C. J., Renne, P. R., Vanderkluysen, L., Pande, K., Self, S., & Mittal, T. (2019). The eruptive tempo of deccan volcanism in relation to the cretaceous-paleogene boundary. *Science*, *363*(6429), 866–870.

Stagno, V., Ojwang, D. O., McCammon, C. A., & Frost, D. J. (2013). The oxidation state of the mantle and the extraction of carbon from earth's interior. *Nature*, *493*(7430), 84–88.

Stober, I., & Bucher, K. (2015). Hydraulic conductivity of fractured upper crust: insights from hydraulic tests in boreholes and fluid-rock interaction in crystalline basement rocks. *Geofluids*, *15*(1-2), 161–178.

Suarez, C. A., Edmonds, M., & Jones, A. P. (2019, oct). Earth catastrophes and their impact on the carbon cycle. *Elements*, *15*(5), 301–306. doi: 10.2138/gselements.15.5.301

Svensen, H., Torsvik, T., Callegaro, S., Augland, L., Heimdal, T., Jerram, D., ... Pereira, E. (2018). Gondwana large igneous provinces: plate reconstructions, volcanic basins and sill volumes. *Geological Society, London, Special Publications*, *463*(1), 17–40.

Taisne, B., & Tait, S. (2011). Effect of solidification on a propagating dike. *Journal of Geophysical Research: Solid Earth*, *116*(1), 1–14. doi: 10.1029/2009JB007058

Tarasewicz, J., White, R. S., Woods, A. W., Brandsdóttir, B., & Gudmundsson, M. T. (2012). Magma mobilization by downward-propagating decompression of the eyjafjallajökull volcanic plumbing system. *Geophysical Research Letters*, *39*(19).

Taron, J., Elsworth, D., & Min, K.-B. (2009). Numerical simulation of thermal-hydrologic-mechanical-chemical processes in deformable, fractured porous media. *International Journal of Rock Mechanics and Mining Sciences*, *46*(5), 842–854.

Tejada, M., Mahoney, J., Neal, C., Duncan, R., & Petterson, M. (2002). Basement geochemistry and geochronology of central malaita, solomon islands, with implications for the origin and evolution of the ontong java plateau. *Journal of Petrology*, *43*(3), 449–484.

Tetreault, J., & Buiter, S. (2018). The influence of extension rate and crustal rheology on the evolution of passive margins from rifting to break-up. *Tectonophysics*, *746*, 155–172.

Thordarson, T., & Self, S. (1993). The laki (skaftár fires) and grímsvötn eruptions in 1783–1785. *Bulletin of Volcanology*, *55*(4), 233–263.

Thordarson, T., & Self, S. (1998). The roza member, columbia river basalt group: A gigantic pahoehoe lava flow field formed by endogenous processes? *Journal of Geophysical Research: Solid Earth*, *103*(B11), 27411–27445.

Tibaldi, A. (2015). Structure of volcano plumbing systems: A review of multi-parametric effects. *Journal of Volcanology and Geothermal Research*, *298*, 85–135. doi: 10.1016/j.jvolgeores.2015.03.023

Torsvik, T. H. (2020). Connecting the deep earth and the atmosphere.

Townsend, M., & Huber, C. (2020a). A critical magma chamber size for volcanic eruptions. *Geology*.

Townsend, M., & Huber, C. (2020b, feb). A critical magma chamber size for volcanic eruptions. *Geology*. doi: 10.1130/g47045.1

Townsend, M., Huber, C., Degruyter, W., & Bachmann, O. (2019). Magma chamber growth during inter-caldera periods: insights from thermo-mechanical modeling with applications to laguna del maule, campi flegrei, santorini, and aso. *Geochemistry, Geophysics, Geosystems*.

Vanderkluysen, L., Mahoney, J. J., Hooper, P. R., Sheth, H. C., & Ray, R. (2011). The feeder system of the Deccan Traps (India): Insights from dike geochemistry. *Journal of Petrology*, *52*(2), 315–343. doi: 10.1093/petrology/egq082

van Gerve, T., Neave, D., Almeev, R., Holtz, F., & Namur, O. (2020). Zoned crystal records of transcrustal magma transport, storage and differentiation: insights from the shatsky rise oceanic plateau. *Journal of Petrology*.

Vye-Brown, C., Gannoun, A., Barry, T., Self, S., & Burton, K. (2013). Osmium isotope variations accompanying the eruption of a single lava flow field in the columbia river flood basalt province. *Earth and Planetary Science Letters*, *368*, 183–194.

Vye-Brown, C., Self, S., & Barry, T. (2013). Architecture and emplacement of flood basalt flow fields: case studies from the columbia river basalt group, nw usa. *Bulletin of Volcanology*, *75*(3), 697.

Wadge, G. (1981). The variation of magma discharge during basaltic eruptions. *Journal of Volcanology and Geothermal Research*, *11*(2-4), 139–168.

Wang, H., van Hunen, J., & Pearson, D. G. (2015). The thinning of subcontinental lithosphere: The roles of plume impact and metasomatic weakening. *Geochemistry, Geophysics, Geosystems*. doi: 10.1002/2015GC005784

Wang, X.-C., Wilde, S. A., Xu, B., & Pang, C.-J. (2016). Origin of arc-like continental basalts: implications for deep-earth fluid cycling and tectonic discrimination. *Lithos*, *261*, 5–45.

Weatherley, S. M., & Katz, R. F. (2012). Melting and channelized magmatic flow in chemically heterogeneous, upwelling mantle. *Geochemistry, Geophysics, Geosystems*, *13*(1), 1–23. doi: 10.1029/2011GC003989

Weatherley, S. M., & Katz, R. F. (2015). Melt transport rates in heterogeneous mantle beneath mid-ocean ridges. *Geochimica et Cosmochimica Acta*. doi: 10.1016/j.gca.2015.09.029

Weisstein, E. W. (2003). Oblate spheroid.

Wenker, S., & Beaumont, C. (2018). Effects of lateral strength contrasts and inherited heterogeneities on necking and rifting of continents. *Tectonophysics*, *746*, 46–63.

White, R. S., Edmonds, M., Maclennan, J., Greenfield, T., & Agustsdottir, T. (2019). Melt movement through the icelandic crust. *Philosophical Transactions of the Royal Society A*, *377*(2139), 20180010.

Wieser, P. E., Edmonds, M., Maclennan, J., & Wheeler, J. (2020). Microstructural constraints on magmatic mushes under kīlauea volcano, hawai'i. *Nature communications*, *11*(1), 1–14.

Wignall, P. B. (2001). Large igneous provinces and mass extinctions. *Earth-science reviews*, *53*(1-2), 1–33.

Wolff, J., & Ramos, F. (2013). Source materials for the main phase of the Columbia

River Basalt Group: Geochemical evidence and implications for magma storage and transport. *Geological Society of America Special Papers*, *497*(11), 273–291. doi: 10.1130/2013.2497(11)

Woods, A. W., & Huppert, H. E. (2003). On magma chamber evolution during slow effusive eruptions. *Journal of Geophysical Research*, *108*(B8), 2403. doi: 10.1029/2002JB002019

Wright, T. L., & Marsh, B. (2016). Quantification of the intrusion process at kilauea volcano, hawai'i. *Journal of Volcanology and Geothermal Research*, *328*, 34–44.

Wylie, J. J., Helfrich, K. R., Dade, B., Lister, J. R., & Salzig, J. F. (1999). Flow localization in fissure eruptions. *Bulletin of Volcanology*, *60*(6), 432–440.

Yatheesh, V. (2020). Structure and tectonics of the continental margins of india and the adjacent deep ocean basins: Current status of knowledge and some unresolved problems. *Episodes*, *43*(1), 586–608.

Yaxley, G. M., Ghosh, S., Kiseeva, E. S., Mallik, A., Spandler, C., Thomson, A. R., & Walter, M. J. (2019). Co2-rich melts in earth. In *Deep carbon: Past to present.* Cambridge University Press.

Yu, X., Lee, C.-T. A., Chen, L.-H., & Zeng, G. (2015). Magmatic recharge in continental flood basalts: Insights from the chifeng igneous province in inner mongolia. *Geochemistry, Geophysics, Geosystems*, *16*(7), 2082–2096.

Zhang, J., Chen, J., & Huang, Y. (2019). Secondary cones of the shatsky rise and implications for late-stage volcanism atop oceanic plateaus. *Journal of Ocean University of China*, *18*(5), 1115–1122.